THE EVRYSCOPE FAST TRANSIENT ENGINE: REAL-TIME DISCOVERY OF RAPIDLY EVOLVING TRANSIENTS WITH EVRYSCOPE AND THE ARGUS OPTICAL ARRAY

Henry T. Corbett, I.V.

A dissertation submitted to the faculty of the University of North Carolina at Chapel Hill in partial fulfillment of the requirements for the degree of Doctor of Philosophy in the Department of Physics and Astronomy.

Chapel Hill
2023

Approved by:

Nicholas M. Law

Rosa T. Branca

Andrew W. Mann

Robert M. Quimby

Daniel E. Reichart

ABSTRACT

Henry T. Corbett: The Evryscope Fast Transient Engine: Real-Time Discovery of
Rapidly-Evolving Transients with Evryscope and the Argus Optical Array
(Under the direction of Nicholas M. Law)

Modern synoptic sky surveys are typically designed to detect supernovae-like transients, using a tiling strategy to identify objects that evolve on day-to-month timescales. Astrophysical phenomena with sub-hour durations, ranging from galactic stellar flares to optical flashes accompanying gamma-ray bursts, have largely escaped scrutiny. Due to their low intrinsic rates and short durations, surveys for fast transients must simultaneously cover significant fractions of the sky at sub-hour cadences, often by combining multiple telescopes. The Evryscopes represent an extreme of this approach, combining 43 small telescopes to image 38% of the entire sky every two minutes. To investigate bright and fast transients with the Evryscopes, I developed the Evryscope Fast Transient Engine (EFTE), a real-time transient detection and photometric analysis pipeline. EFTE uses a unique direct image subtraction routine suited to continuously monitoring the transient sky at minute cadence. Candidates are produced within two minutes for 98.5% of images, and are internally filtered using VetNet, a machine learning algorithm trained to sort real astrophysical events from false positives, both instrumental and astronomical, including millisecond-timescale reflections, or “glints” from satellites and debris in Earth orbit. Glints are a dominating foreground for astronomical surveys in the extreme time domain. I present the first measurements of the glint rate, noting that it exceeds the combined rate of public alerts from all active all-sky, fast-timescale transient searches, including neutrino, gravitational-wave, gamma-ray, and radio observatories. I further report spectroscopic followup of two stellar flares identified in real-time from the EFTE alert stream using glint-mitigation and science-driven selection metrics. These are the closest spectra relative to peak ever observed for flare stars outside of dedicated starting campaigns on known active stars, and provide unique constraints on the evolution of the flare continuum and temperature. Finally, EFTE is the software test bed for the pipelines of the Argus Optical Array, an upcoming all-sky survey based on the Evryscope concept scaled to the depths of the deepest operating sky surveys and a terabit per second data rate. This work concludes with a description of the Argus prototype series and pipelines, and an overview of fast transient science with the Array.

For Verlee Underwood, who would have liked a copy,

and Zack Jones, who would have not.

ACKNOWLEDGEMENTS

This work could not have been possible without the support, mentorship, and generosity of more people than I can list; nonetheless, I would be remiss to not enumerate some here. First, I would like to thank the members of the Evryscope, now Argus Array, lab here at UNC: Octavi Fors, Jeff Ratzloff, Carl Ziegler, Ward Howard, Amy Glazier, Ramses Gonzalez, Nathan Galliher, Alan Vasquez, Lawrence Machia, and Jon Carney. I am grateful to have been able to learn, work, and wash windows in exotic locales with all of you. Your contributions run through the work presented here much like we have run through lab space these last few years, and I sincerely appreciate all of them. Special thanks are of course due to my dissertation advisor, Nicholas M. Law. Thank you for your mentorship and support over the years, starting with inviting me to work on the Evryscope project back when I took your 519 course as a continuing education student. You have opened many doors for me, most of which I would have scarcely even been aware of in your absence.

Josh Reding, Christopher Moakler, Jake Brooks; thank you for our brief foray into developing a genuine technical capacity for theoretical physics; modest and short-lived as it was.

I am deeply grateful for the support and early guidance provided by the members of the community of astronomers, both amateur and professional, in the central North Carolina region, whom I have been lucky to know both through the Cline Observatories at Guilford Technical Community College and at my alma mater, Guilford College. Don Smith, Steve Shapiro, Thom Espinola, and Thom English, thank you for your time and for all of the work you have put into making these departments and communities such thriving places for astronomy.

It is due to Rex Adelberger's generosity of time and spirit that I initially developed a love for research and the process of solving problems of the "advanced basic" variety (for instance, how to remove ants from a radio telescope correlator). While Rex is longer with us, I find myself constantly re-discovering his shrewd and experimental thinking with regards to problems of all varieties and scales, and appreciating it more with each passing year.

I would like to thank my family and friends outside of Phillips Hall, who have been so fundamental in helping me maintain perspective and sustained my efforts over these last few years. Most of all, thank you to my mother, Patty, for her unwavering support and belief in me, to my partner, Emily Albert, for her support both graphical, practical, and emotional, and to Ollie, for many formative discussions of a technical nature; this work would not have been possible without any of you.

TABLE OF CONTENTS

LIST OF TABLES

LIST OF FIGURES

LIST OF ABBREVIATIONS AND SYMBOLS

2MASS	2-Micron All-Sky Survey
A2TD	Argus Array Technology Demonstrator
AAVSO	American Association of Variable Star Observers
ANTARES	Arizona-NOIRLab Temporal Analysis and Response to Events System
APASS	AAVSO Photometric All-Sky Survey
ATLAS	Asteroid-Terrestrial Last Alert System
ASAS-SN	All-Sky Automated Survey for SuperNovae
CHIME	Canadian Hydrogen Intensity Mapping Experimen
CMD	Color-Magnitude Diagram
CTIO	Cerro Tololo Inter-American Observatory
CPU	Central Processing Unit
CCD	Charge-Coupled Device
CMOS	Completmentary Metal-Oxide Semiconductor
Dec	Declination
DECam	Dark Energy Camera
dM	M-type Dwarf
DR	Data Release
DSLR	Digital Single-Lens Reflex
DWF	Deeper, Wider, Faster (Andreoni et al. 2020a)
eFOT	Extragalactic Fast Optical Transient
EFTE	Evryscope Fast Transient Engine
EVRT	Evryscope Transient candidate prefix
FOV	Field of view
FRB	Fast Radio Burst
FWHM	Full Width at Half Maximum
GACAM	Goodman Acquisition Camera

GBM	Gamma-ray Burst Monitor
Gbps	Gigabit per second
GRB	Gamma-ray Burst
GiB	Gibibyte (2^{30} bytes)
GIS	Geographic Information Systems
GHTS	Goodman High-Throughput Spectrograph (on SOAR)
GLADE	Galaxy List for the Advanced Detector Era
GPU	Graphics Processing Unit
HARPS	High Accuracy Radial Velocity Planet Searcher
HDPS	[Argus] Hierarchical Data Processing System
HEALPix	Hierarchical Equal Areal isoLatitude Pixelization
HFD	Half Flux Diameter
HOTPANTS	High Order Transform of Psf ANd Template Subtraction
ID	Identification
IP	Internet Protocol
iPTF	Intermediate Palomar Transient Factory
JSON	JavaScript Object Notation
LIGO	Laser Interferometer Gravitational-wave Observatory
LSST	Legacy Survey of Space and Time
LEO	Low Earth Orbit
MC	Monte Carlo
MEO	Medium Earth Orbit
ML	Machine Learning
MLO	Mount Laguna Observatory
NUV	Near Ultra Violet
OASES	Organized Autotelescopes for Serendipitous Events Survey
PiB	Pebibyte (2^{50} bytes)

PSF	Point Spread function
PTF	Palomar Transient Factory
Pan-STARRS	Panoramic Survey Telescope & Rapid Response System
RA	Right Ascension
RASA	Rowe-Ackermann Schmidt Astrograph
RAM	Random Access Memory
ROSAT	ROentgen SATellite
SOAR	SOuthern Astrophysical Research Telescope
SSD	Solid State Drive
SQL	Structured Query Language
Tbps	Terabit per second
TESS	Transiting Exoplanet Survey Satellite
TiB	Tebibyte (2^{40} bytes)
TPV	Tangent Polynomial Value *(uncertain)*
VSX	international Variable Star indeX
WCSLIB	World Coordinate Systems Library (Calabretta et al. 2004)
ZOGY	Zackey-Ofek-Gal Yam (see Zackay et al. (2016))
ZTF	Zwicky Transient Facility

CHAPTER 1: INTRODUCTION AND MOTIVATION

Section 1.1: The Rapidly Varying Sky

Astrophysical phenomena with ultra-short (sub-minute) durations have largely escaped the scrutiny of modern synoptic sky surveys, which are typically optimized for supernovae-like transients evolving on day-to-month timescales. Sensitivity to minute- and hour-timescale events can be achieved through sub-surveys over fractional sky areas; however, these searches typically use many-second exposures, confining the shortest events to single images.

For the fastest events, including prompt optical flashes from long gamma-ray bursts (GRBs) (Fox et al. 2003; Cucchiara et al. 2011; Vestrand et al. 2014; Martin-Carrillo et al. 2014; Troja et al. 2017), shock breakout in young supernovae (Garnavich et al. 2016; Bersten et al. 2018), and stellar flares (Howard & MacGregor 2022; Pietras et al. 2022; Aizawa et al. 2022), the duration of the event can be ≤ 1 hour, shorter than the base observing cadence of conventional tiling surveys, such as the Zwicky Transient Facility (ZTF; Bellm et al. 2019), Pan-STARRS (Kaiser et al. 2010), the Catalina Sky Survey (CSS; Larson et al. 2003) and Catalina Real-Time Transient Survey (CRTS; Drake et al. 2009), SkyMapper (Keller et al. 2007), the Asteroid Terrestrial-impact Last Alert System (ATLAS; Tonry et al. 2018), the All-Sky Automated Survey for Supernovae (ASAS-SN; Shappee et al. 2014), the Dark Energy Survey (DES; Dark Energy Survey Collaboration et al. 2016), the Gravitational Wave Optical Transient Observatory (GOTO; Dyer et al. 2018), and the Mobile Astronomical System of Telescope-Robots (MASTER; Lipunov et al. 2004). Each of these surveys tile the sky on timescales of days to maximize their likelihood of detecting supernova-like transients, which evolve over the course of days and months. Figure 1.1 compares the instantaneous depth and survey speed of all active and planned sky surveys with rapid-transient detection capabilities and all-sky footprints.

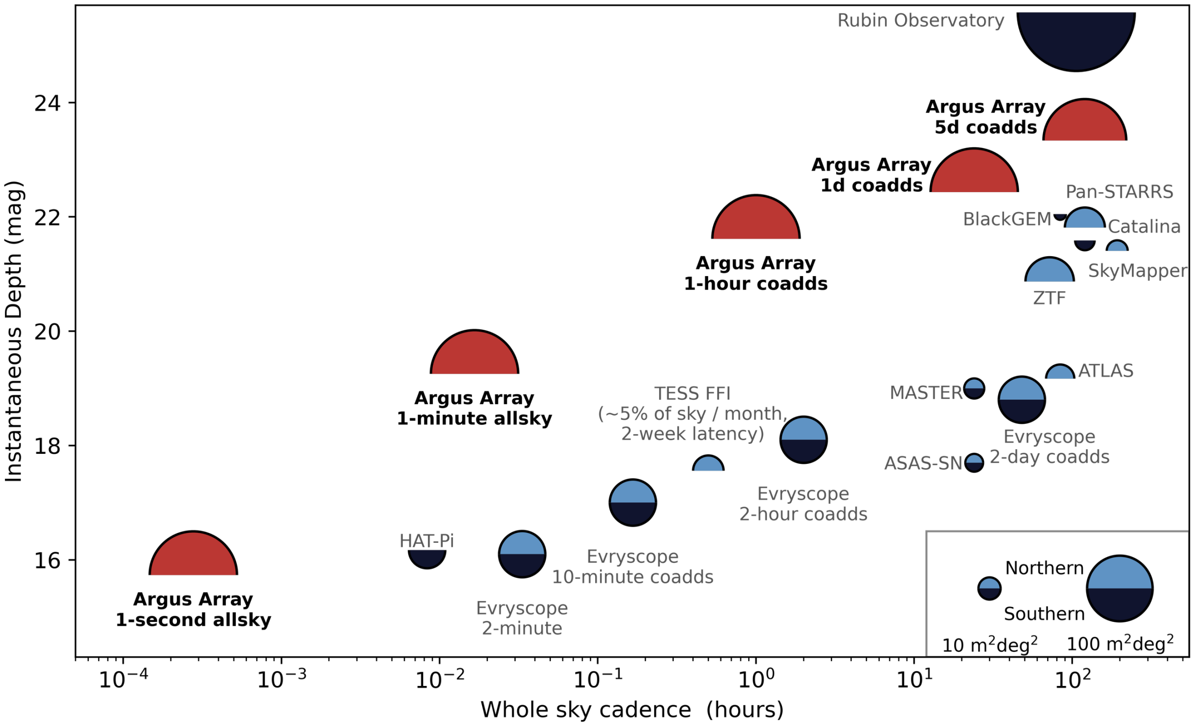

Figure 1.1 Operating and planned all-sky surveys with rapid transient detection capabilities. The position of each survey is a function of mirror, étendue, cadence and survey design. The shape and size of the points shows site location and étendue respectively. Where telescopes operate multiple surveys, the plot shows the survey with the fastest rate of all-sky coverage, and (where available in the literature) depths refer to dark-sky, 5σ-detection limiting magnitudes. Adapted from Law et al. (2022c).

Faster events, occurring on minute-to-hour timescales, are detected in tiling surveys, but with frequently under-sampled light curves. Tiling surveys are also not typically optimized for minute-scale latency between detection and reporting, precluding spectroscopic follow-up on timescales comparable to the lifetime of the transient. As a result, searches for short-lived events typically require simultaneous coordinated observations of small sky regions for spectroscopic confirmation and classification, as in the Deeper-Wider-Faster program (DWF; Andreoni et al. 2020a). However, previous searches for fast transients in this regime, by the DWF team (Andreoni et al. 2020a), as well as from PanSTARRS (Berger et al. 2013), iPTF

(Ho et al. 2018), PTF (van Roestel et al. 2019), Tomo-e-Gozen (Richmond et al. 2020), and the Organized Autotelescopes for Serendipitous Events Survey (OASES; Arimatsu et al. 2021) have only produced upper-limits on the extragalactic event rate of fast transients, suggesting that increased areal survey rates are necessary to observe any new populations of high-speed transients.

While no extragalactic fast transients with sub-hour durations have been identified in these un-targeted searches, many classes of exotic fast transients have been predicted, and many examples of known galactic transients have been observed. Additionally, fast transients are observed at other wavelengths, most notably in the radio, and the possibility to identify optical counterparts to these signals commonly motivates continued efforts to explore this section of the time domain.

1.1.1 Stellar Flares

Over the last few decades, the promise of M-dwarfs as hosts of habitable exoplanets has been debated. M-dwarfs are extremely common, making up the majority of nearby stars (Henry et al. 2006; Covey et al. 2008). Detection of Earth- and super-Earth-sized planets around M-dwarfs is comparably easier than around higher-mass stars, due to their relative sizes and transit depths. These facts, coupled with the estimate that over 10% of M-dwarfs host rocky, habitable-zone planets (Dressing & Charbonneau 2013; 2015), appear to make these stars ideal candidates in the search for exoplanetary life.

However, M-dwarfs are known to be extremely active and prone to frequent flares, which make up the majority of galactic transients at minute-to-hour timescales (Kulkarni & Rau 2006). Flares are caused by reconnections in the stellar magnetic field, producing radiation across the electromagnetic spectrum on timescales ranging from seconds to hours (Kowalski et al. 2013; Allred et al. 2015). Radiation from the largest events, so-called *superflares*, reach energies $\geq 10^{33}$ erg – orders of magnitude greater than the largest solar flares (Schaefer et al. 2000). Flares are responsible for much of the UV environment of rocky planets orbiting cool stars (Walkowicz et al. 2008), potentially eroding Earth-like atmospheres entirely (Loyd et al. 2018; Howard et al. 2018a) or perhaps more commonly, high-energy particle fluence accompanying large flares can deplete an Earth-like atmosphere's ozone column depth by up to 94% over time (Segura et al. 2010).

In either case, the depletion of an Earth-like atmosphere's ozone layer leaves the planet's surface vulnerable to possible sterilization by UV radiation from more common, smaller flares until the ozone column recovers (Loyd et al. 2018; Howard et al. 2018a; Tilley et al. 2019). Nevertheless, it is possible that the excess UV flux provided by some periodic flaring could balance out the otherwise tiny quiescent UV emission from the star, providing the necessary UV radiation to support prebiotic chemistry (Ranjan et al. 2017; Rimmer et al. 2018).

Spectroscopic observations taken during the initial stages of a flare can reveal temperature and emission-line evolution during their most impulsive phases, which is valuable for constraining both the fundamental flare physics and the potential impacts of flare activity on exoplanet atmospheres. Although photometric observations can provide the initial detection of a flare event and constrain flare rates, photometric observations alone have significant limitations. Andreoni et al. (2020a) noted that the single-band light curves of flare stars are indistinguishable from optical flashes associated with some gamma-ray bursts, such as those in Cucchiara et al. (2011), emphasizing the need for spectroscopic confirmation of flare candidates. All flares also exhibit spectral evolution over the lifetime of the flare, both in temperature profile and relative contributions of line emission versus the stellar continuum (Kowalski et al. 2013). Collectively, these effects can cause estimates of habitability–impacting UV flux to vary by an order of magnitude or more, due solely to differences in the flare's assumed temperature or elapsed time between flare detection and spectroscopic follow-up. Rapid spectroscopic observation immediately after flare detection is thus critical both for confirming the event as a flare and for quantifying its effect on the local space weather environment.

1.1.2 Fast Radio Bursts and their Potential Optical Counterparts

Fast Radio Bursts (FRBs) are highly luminous (10^{42} erg/s), millisecond-timescale radio transients observed primarily at extragalactic distances (Lorimer 2007, Thornton 2013). FRBs are common across the sky, occurring at rates of $O(10^3)$ per sky per day (Chawla et al. 2017; Bhandari et al. 2018), with 635 unique sources recorded to-date. The majority of known FRBs have been discovered in wide-field radio surveys, which generally have insufficient localization precision to establish a host galaxy without followup using Very Long Baseline Interferometry (VLBI). This is only possible for the 1-in-30 FRBs that appear to produce repeated bursts. For the 23 known repeaters, precise VLBI localizations of their emitters within their host galaxies has revealed a diversity of environments. While some FRBs are clearly coincident with star-forming regions (Marcote et al. 2020; Fong et al. 2021; Piro et al. 2021; Ravi et al. 2022; Nimmo et al. 2022), others are significantly offset (Bassa et al. 2017; Tendulkar et al. 2021; Xu et al. 2022), or even in host galaxies with a minimal SFR (Heintz et al. 2020; Mannings et al. 2021; Bhandari et al. 2022), or globular clusters (Kirsten et al. 2022).

The characteristic timescales and luminosities of FRBs require a high-energy, but physically small, light emitting region, suggesting a compact-object origin, though the specific progenitors and mechanisms remain an open question (see Platts et al. (2019) for an overview). The recent detection (CHIME/FRB Collaboration et al. 2020; Bochenek et al. 2020) of a bright, FRB-like burst (FRB 20200428A) from the galactic magnetar SGR 1935+2154 suggests that magnetars are likely among the progenitors of fast radio bursts, and models involving a neutron star or magnetar are currently favored. However, even with a settled progenitor, the diversity of host environments and the statistical differentiation between the repeating and non-repeating populations, Zhang et al. (2022) suggest that multiple mechanisms can exist, potentially corresponding to each magnetar's formation channel; CC SNe for regions with a high SFR, binary merger or accretion-drive collapse for other sources.

Magnetars may produce FRB-like coherent emission via reconnection directly in the magnetosphere (Lyutikov 2021), analogous to flaring events on main sequence stars, or through synchrotron maser emission from the forward shock between a flare and the surrounding medium at large radii (Metzger et al. 2019). The latter scenario would additionally predict an associated rapidly-fading optical afterglow powered by incoherent synchrotron radiation, with detectability depending on the electron-positron pair density in the plasma wind (Metzger et al. 2019; Beloborodov 2020). Multiple searches for optical emission have been conducted, all focused on known repeating bursts (Petroff et al. 2015; Hardy et al. 2017; Tominaga et al. 2018; Niino et al. 2018; MAGIC Collaboration et al. 2018; Tingay 2020; Andreoni et al. 2020b; Kilpatrick et al. 2021; Núñez et al. 2021; Niino et al. 2022; Tingay 2022), except for Xin et al. (2021), which reports optical upper limits for the singular burst FRB 20181130B. One plausible late-time counterpart has been recently discovered (AT 2022hur; Li et al. 2022), an otherwise-unclassified optical transient spatially coincident with FRB 20180916B. However, no prompt transient multi-wavelength counterpart to a fast radio burst has been discovered to date.

1.1.3 Exotic Extragalactic Fast Transients

Other classes of short-duration transients have been predicted, including accretion of planetary remnants onto the surfaces of white dwarfs (Di Stefano et al. 2015), and from exotic scenarios originally linked to FRBs, like starquakes (Wang et al. 2018), the formation of strange quark stars from magnetar collapse (Gupta & Saini 2018), or the explosion of a primordial black hole (Barrau et al. 2014). Despite many years of searches (Sokołowski et al. 2010; Griffin 2012; Berger et al. 2013; Karpov et al. 2018; Andreoni et al. 2020a; Richmond et al. 2020; Tingay 2020; Tingay & Joubert 2021; Arimatsu et al. 2021), no discoveries of extragalactic fast optical transients (eFOTs) on sub-minute timescales have been claimed. Two broad reasons for this lack of discoveries are likely: 1) areal event rates for eFOTs are intrinsically low, requiring survey grasp in excess of current instrument capability, and

2) near-field event rates from artificial Earth satellites (Maley 1987; 1991; Corbett et al. 2020; Nir et al. 2021; Karpov & Peloton 2022) and galactic M-Dwarf flares (Kulkarni & Rau 2006) are high, requiring a significant follow-up effort to separate any eFOTs from a dense foreground of nearby sources. Figure 1.2 shows the upper limits determined by these surveys, as well as the potential limits that could be established by the upcoming Argus Pathfinder and Argus Optical Array surveys (described below and in Chapters 6 and 7) in the absence of any eFOT detections.

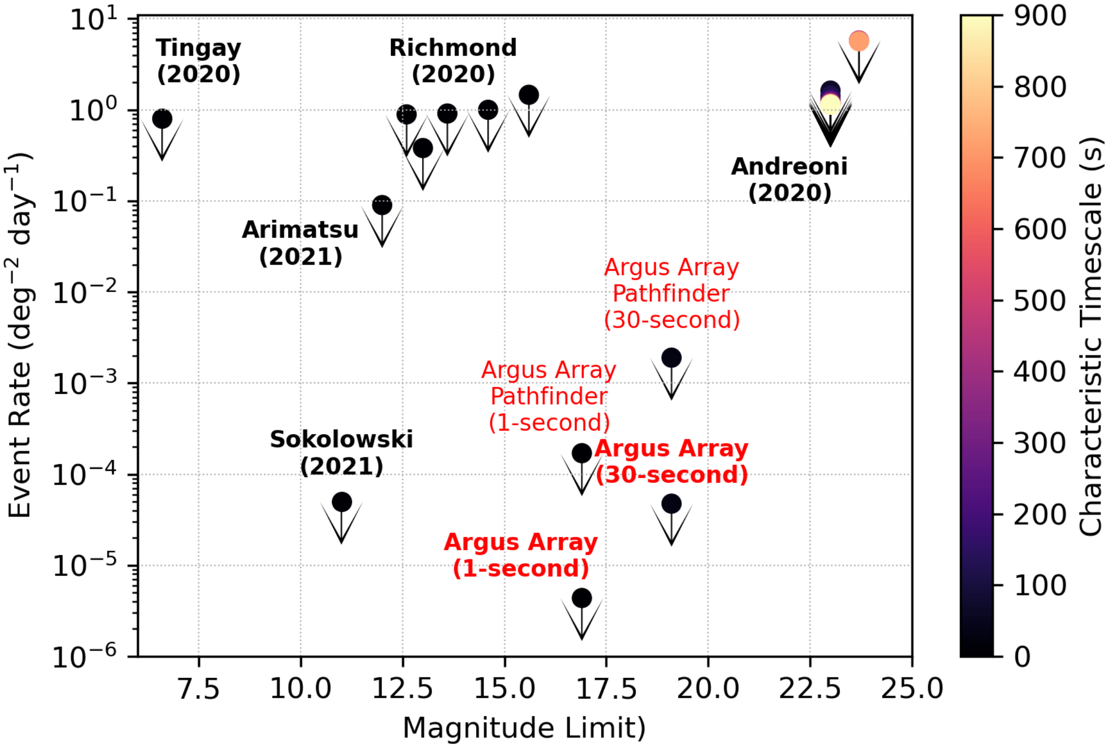

Figure 1.2 Upper limits for the occurrence rate of fast optical transients as a function of magnitude and characteristic timescale, including potential limits that could be established by Argus Pathfinder and the Argus Optical Array.

1.1.4 Orbital Debris and Reflections from Earth Satellites

The most common of rapid time domain signals detected from Earth are astronomical in nature, but with the exception of a handful of space telescopes, completely unrelated to astrophysics. Flashes of reflected sunlight from satellites in Earth orbit outnumber astrophysical transients by orders of magnitude. Image contamination by Earth satellites takes two forms: streaks, with uniform illumination over extended trajectories, and glints, which appear as short-duration flashes (Corbett et al. 2020). These two morphologies are frequently degenerate, and depend on the structure and orbit of the reflector. Streaks are associated with fast-moving or slowly-rotating satellites, such as the Starlink constellation discussed in McDowell (2020). Glints are associated with short rotation periods or high altitudes, and are produced by chance alignments between an observer, the sun, and a reflective rotating surface. The duration of a glint is the crossing time of the reflective surface's normal vector across the disk of the sun, less than a second for satellites with minutes-long rotation periods (Schaefer et al. 1987). Short durations relative to their motion on the sky and sharp contrast with their associated streaks have led to glints being mistaken for astrophysical events (Schaefer et al. 1987; Maley 1987; 1991; Rast 1991; Shamir & Nemiroff 2006).

Karpov et al. (2016) presents time-resolved observations of satellite glints that reveal a peak in the duration distribution at 0.4 seconds. Approximately half of the glints reported in Karpov et al. (2016) were not coincident with the position of a satellite in the NORAD database. Similarly, Tingay (2020) and Karpov & Peloton (2022) both note multiple candidates with no or poorly-constrained association with tracked satellites based on their latest two-line element parameters. Based on these observations, it is unlikely that glints will be universally separable from a population of astrophysical transients based on ephemerides for tracked satellites.

Section 1.2: Time-domain Survey Optimization and the Evryscopes

One common parametrization of the sensitivity of a telescope or survey to time domain information is its grasp, defined as the volume of the universe which the telescope can observe per unit time. Ofek & Ben-Ami (2020)[1] define the grasp of an instrument as:

$$\mathcal{G} \propto \Omega A_{\mathrm{eff}}^{3/4} \frac{\sigma^{-3/2} t_{\mathrm{E}}^{3/4}}{t_{\mathrm{E}} + t_{D}}, \tag{1.1}$$

where Ω is the field of view (FOV), A_{eff} is the light-sensitive collecting area, σ is the size of the point spread function (PSF), t_{E} is the exposure time, and t_{D} is the dead time between exposures. An alternate approach to parametrize survey performance is étendue (G), a simple geometric quantity relating the collecting area and field of view of a telescope:

$$G = A_{\mathrm{eff}} \times \Omega. \tag{1.2}$$

In both cases, the metric is most directly sensitive to two fundamental parameters of the system: the telescope size, described by A_{eff}, and the fraction of the sky that can be observed at once, Ω. While tiling surveys typically prioritize increasing A_{eff} to reap the non-linear benefits of increasing volume, there is an alternate approach to survey design based on building on Ω using arrays of smaller telescopes with modest depth but huge fields of view. Designing a survey in this way limits the sensitivity to distant events like supernovae, but maximizes the sensitivity of the system to rare and short-lived events like flares, prompt counterparts to distant explosions, and, unfortunately, satellite reflections.

1.2.1 Overview of the Evryscope Survey

The Evryscopes are a pair of multiplexed wide-field survey telescopes, designed to maximize the FOV (Ω). The Evryscopes are located at Cerro Tololo Inter-American Observatory

---

[1] A similar metric, the volumetric survey speed, is defined in Bellm (2016).

(CTIO) in Chile and Mount Laguna Observatory (MLO) in California. Figure 1.3 shows the two instruments installed at their respective observatories. Each site consists of up to twenty-seven 6.1 cm aperture camera units, arranged to observe the majority of the sky above an airmass of ∼2 simultaneously. Collectively, the Evryscopes have a instantaneous field of view of 16,512 sq. degrees (15,929 sq. degrees accounting for overlaps between adjacent cameras) with a resolution of 13.2arcsec pixel^{-1} across a 1.24 gigapixel combined image plane. The telescopes observe at a constant two-minute cadence with a 97% duty cycle, and collect an average of 600 GiB of data per night. While the primary Evryscope survey has been conducted in the Sloan g-band, Evryscope-North is also equipped with a Sloan r filter for use in future surveys. All of the telescopes at each site are attached on a single mount, which tracks the sky in two-hour increments.

Figure 1.3 Evryscope-North, installed at Mount Laguna Observatory, outside San Diego, California, and Evryscope-South at Cerro Tololo Inter-American Observatory, Chile.

The instruments are fully robotic, operating autonomously based on a local weather station. Evryscope-South has been in operation since May 2015, and Evryscope-North began science operations in January 2019. For a full description of the instrument and Evryscope science programs, see Ratzloff et al. (2019a) and Law et al. (2015). The instrument parameters are summarized in Table 1.1.

Table 1.1 System properties for the Evryscopes. For further information, see Ratzloff et al. (2019a)

Property	Evryscope-South	Evryscope-North
Field of View (Deduplicated)	8520 sq. deg	7409 sq. deg
Field of View (Total)	8832 sq. deg	7680 sq. deg
Detector Size	662.4 MPix	576 MPix
Cadence	2 minutes	
Aperture	6.1 cm	
Pixel Scale	13.2 arcsec/pixel	
Data Rate	165 Mbps (1.2 GiB/minute)	

1.2.2 Observation Strategy

The Evryscopes utilize two distinct strategies for determining the two-hour-observing fields that are observed over the course of the night:

1. Semi-random, with the eastern-most edge of the field placed 30 degrees above the horizon to the east at the start of each 2-hour observation.
2. Fixed pointings, chosen from 48 overlapping regions, separated by 7.5 degrees in right ascension.

In both scenarios, the duration of a single pointing is limited by the time it takes the westward edge of the field to pass beneath an airmass of $\sim$2. This timescale (a “ratchet”) is typically on the order of two hours. Each Evryscope tracks continuously at the sidereal rate. Minimal (few arcminute) drift due to polar alignment is present over the course of a ratchet, but the visible field between consecutive two-minute exposures is consistent, point-like, and unstreaked.

Semi-random pointings (currently used for Evryscope-South) are preferred for long-term photometric performance, as diverse field positions allow sensor-plane effects to average out over the duration of the survey. Because of the commercial-off-the-shelf optics used, individual cameras exhibit up to 50% vignetting at the edge of the sensor field of view. Randomized pointings also minimize the effects of camera-to-camera periodic noise, provide some resilience against CCD sensor defects, and limit the prevalence of pathological coordinates that are always located at the edge of a sensor and thus unduly affected by optical vignetting. The trade-off is that individual fields repeat only on timescales of months (cross camera) or years (single camera), and only to few-degree precision.

Fixed-fields, by contrast, are used for Evryscope-North, and result in fields that repeat with arc-minute precision on 1-3 day timescales. This repeatability is convenient for transient searches, as it allows us to build up an archive of reference frames to use for image subtraction. For fields above an airmass of 2, 76% are observed within two days of the previous visit, and 97% are observed within a week. Because adjacent fields overlap by $\sim$ 95%, a given sky region will appear in many different pointings, meaning that the field recurrence time is independent of the observing cadence.

Section 1.3: The Argus Optical Array[2]

The Argus Optical Array is a new instrument, which expands the Evryscope design concept and observing strategy to a larger collecting area while maintaining an equivalent FOV. This concept is enabled by a revolution of capabilities in the amateur astronomy community. In 2017, Celestron introduced the Rowe-Ackermann Schmidt Astrograph (RASA) line of telescopes (Berry & the Celestron Engineering Team 2020), which match good image quality across a wide field with low-cost mass production. List prices are only around \$60,000 m^2 of glass, including all secondary optics and ancillary mounting components. Especially when coupled with wide-field sensors, such as the new tens-of-MPix ultra-low-noise complementary metal-oxide semiconductor (CMOS) detectors from Sony, arrays of these telescopes offer an affordable route to building large-scale instruments. Multiplexed CMOS-based arrays are capable of both high-speed operation with negligible (O(μs)) dead time (t_D in Equation 1.1) and a significant survey volume, leveraging minimal readout noise (1.7 e^-) and high quantum efficiency ($> 94\%$) to increase depth by combining multiple images. The survey speed and

---

[2] Parts of this section are adapted from Law et al. (2022c). My contributions to this paper are described in Section 1.6.

depth of Argus relative to all other current and planned synoptic sky surveys, both in single images and deep stacks of many images, is shown in Figure 1.1.

While Evryscope is optimized to maximize simultaneous field of view, with an étendue of 48 m^2 deg^2, larger than almost all active and planned sky surveys, actual on-sky performance and volumetric grasp of the Evryscope cannot match that of conventional surveys with comparable étendue due to the coarse pixel scale (13arcsec $pixel^{-1}$) and 6.1 cm aperture. To optimize Argus for grasp, rather than étendue alone, a pixel scale comparable to the typical atmospheric seeing limit (~1arcsec) is required. Using currently-available sensors and mass-produced optics, the most efficient approach requires O(1000) telescopes with apertures accessible to the consumer market (typically 200-350 mm). This is two orders of magnitude beyond the Evryscope scale, and reliable operation requires some modifications to the Evryscope design concept to ensure stability and minimize maintenance. Rather than an open fiberglass substrate within an otherwise conventional clam-shell observatory dome, the Argus design is sealed to the outside. Each telescope is arranged in an inverted hemisphere and observes the sky through a centrally-located window placed at a "pseudo-focal" point where all of the individual telescope FOVs intersect. The enclosure is maintained at a constant temperature with lab-like conditions with filtered climate-control at all times, minimizing both the wear-and-tear of thermal cycling and the need to periodically clean optical surfaces. A render of the design concept is show in Figure 1.4.

Despite the new pseudofocal design, the survey strategy follows the same approach used by the Evryscopes: an all-sky ($\sim$ 8000 square degree) FOV is multiplexed from the individual telescopes, which are statically mounted to a structure which tracks the sky in fixed intervals, or "ratchets." For Argus, the length is correspondingly shorter (9 or 15 minutes, depending on sensor orientation), due to the smaller crossing times for the individual camera fields of view. At the end of the ratchet, the mount simply returns to the home position and begins again; the only free parameters for the survey design are thus the imaging cadence and the filter bandpass. Argus will perform two surveys, a 1-second cadence program for fast transients

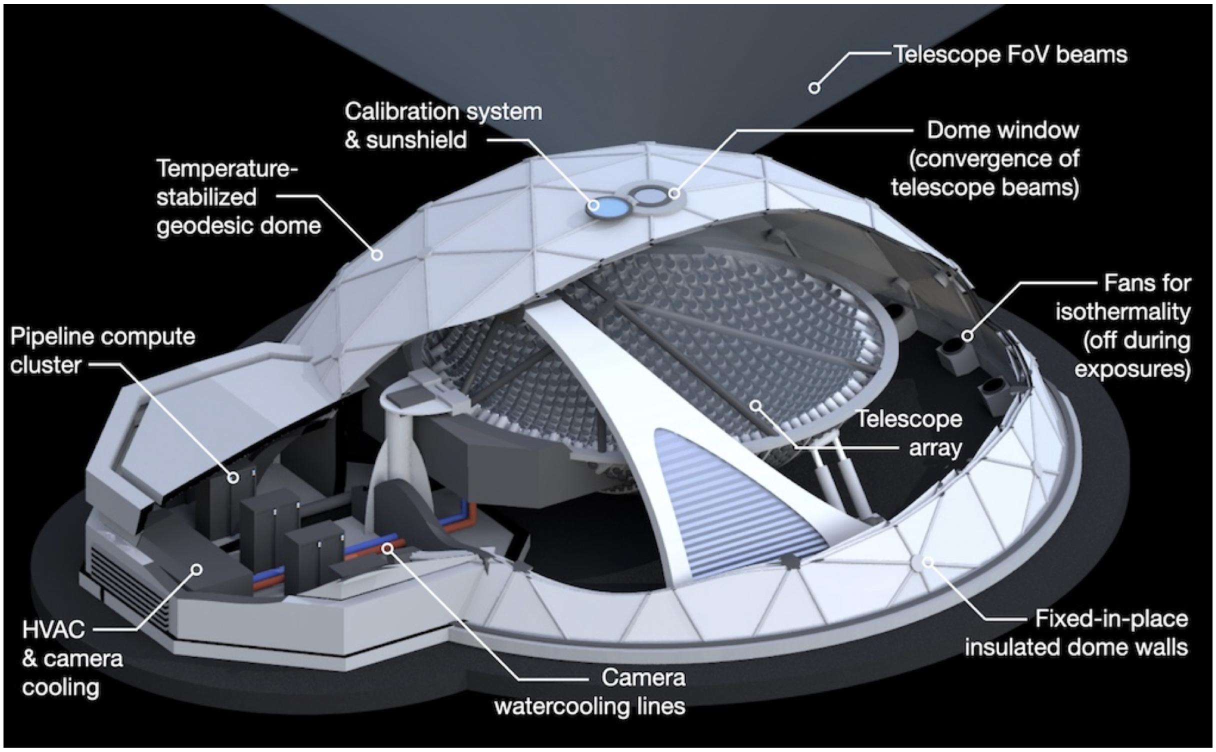

Figure 1.4 Conceptual overview of the Argus Array and its pseudofocal telescope arrangement. The fixed enclosure is heavily-insulated, with an extension housing the near-line computing and climate control systems. Heat generation within the enclosure is minimized by water cooling all electronic components. Figure is reproduced from Law et al. (2022b).

down to $g = 16.1$, and a 30-second base cadence survey with a limiting magnitude of $g = 19.3$. Due to the low readout noise of CMOS sensors, the Array can build up competitive depth by combining hundreds or thousands of images, up to $g = 24.0$ per week. During both surveys, Argus will use alternating filters so that each field will be observed in alternating bandpasses over successive ratchets.

Argus is currently in development through a series of prototypes, including the nine-telescope Argus Array Technology Demonstrator (A2TD; Chapter 6) and the 38-telescope Argus Pathfinder, which was recently (2022 December) installed at the Pisgah Astronomical Research Institute, a dark sky site in western North Carolina. Figure 1.5 shows Pathfinder installed at the observatory. Table 1.2 lists the basic parameters of the Argus Optical Array and the Argus prototype series.

Table 1.2 System properties for the Argus Optical Array and Argus prototype series. Table is reproduced from Law et al. (2022b).

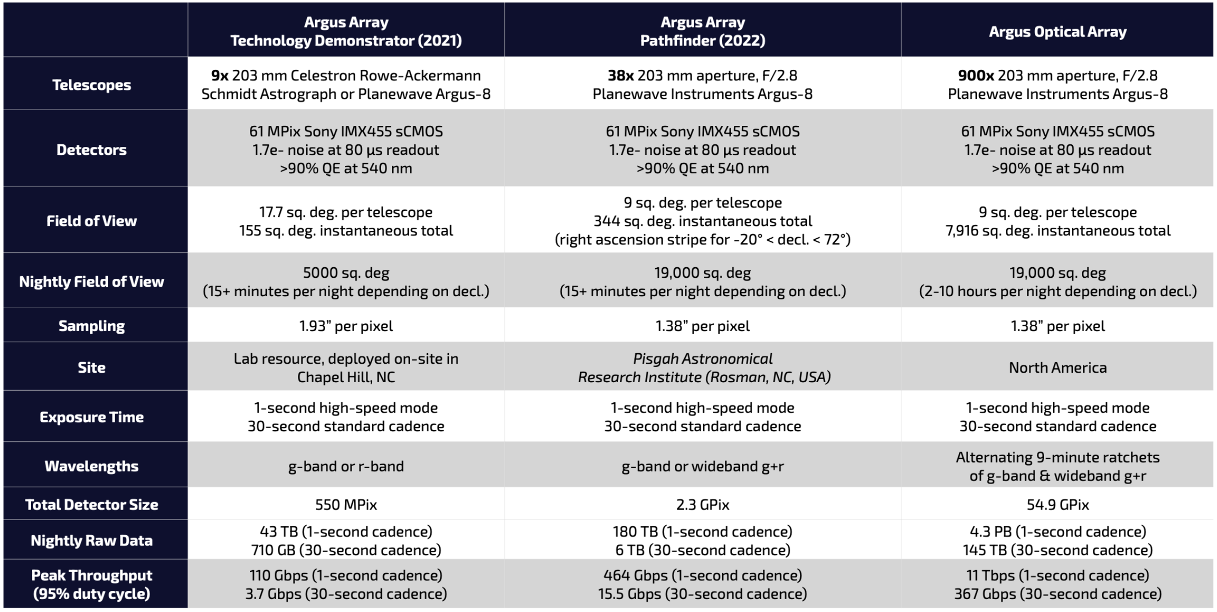

	Argus Array Technology Demonstrator (2021)	Argus Array Pathfinder (2022)	Argus Optical Array
Telescopes	**9x** 203 mm Celestron Rowe-Ackermann Schmidt Astrograph or Planewave Argus-8	**38x** 203 mm aperture, F/2.8 Planewave Instruments Argus-8	**900x** 203 mm aperture, F/2.8 Planewave Instruments Argus-8
Detectors	61 MPix Sony IMX455 sCMOS 1.7e- noise at 80 µs readout >90% QE at 540 nm	61 MPix Sony IMX455 sCMOS 1.7e- noise at 80 µs readout >90% QE at 540 nm	61 MPix Sony IMX455 sCMOS 1.7e- noise at 80 µs readout >90% QE at 540 nm
Field of View	17.7 sq. deg. per telescope 155 sq. deg. instantaneous total	9 sq. deg. per telescope 344 sq. deg. instantaneous total (right ascension stripe for -20° < decl. < 72°)	9 sq. deg. per telescope 7,916 sq. deg. instantaneous total
Nightly Field of View	5000 sq. deg (15+ minutes per night depending on decl.)	19,000 sq. deg (15+ minutes per night depending on decl.)	19,000 sq. deg (2-10 hours per night depending on decl.)
Sampling	1.93" per pixel	1.38" per pixel	1.38" per pixel
Site	Lab resource, deployed on-site in Chapel Hill, NC	*Pisgah Astronomical Research Institute (Rosman, NC, USA)*	North America
Exposure Time	1-second high-speed mode 30-second standard cadence	1-second high-speed mode 30-second standard cadence	1-second high-speed mode 30-second standard cadence
Wavelengths	g-band or r-band	g-band or wideband g+r	Alternating 9-minute ratchets of g-band & wideband g+r
Total Detector Size	550 MPix	2.3 GPix	54.9 GPix
Nightly Raw Data	43 TB (1-second cadence) 710 GB (30-second cadence)	180 TB (1-second cadence) 6 TB (30-second cadence)	4.3 PB (1-second cadence) 145 TB (30-second cadence)
Peak Throughput (95% duty cycle)	110 Gbps (1-second cadence) 3.7 Gbps (30-second cadence)	464 Gbps (1-second cadence) 15.5 Gbps (30-second cadence)	11 Tbps (1-second cadence) 367 Gbps (30-second cadence)

Section 1.4: Pipelines for Transient Discovery in Data-Intensive Surveys

Multiplexed survey instruments like the Evryscopes and Argus Optical Array provide a cost-effective way to explore unique sections of the transient sky; however, rapid cadence and all-sky imaging with high-resolution sensors produce a significant data rate. The Evryscopes' combined 1.24-gigapixel mosaic camera produces a 2.48 GiB image every two minutes and a 5.4 Gbps peak throughput to maintain a 97% duty cycle. The increased resolution (2.3 gigapixel) and higher cadence (up to 1-second) of the Argus Array Pathfinder produces correspondingly higher data rates, up to 464 Gbps and 180 TB of raw data per night. Scaling to the full Argus Array, data rates are equivalent to $\sim 1\%$ of all public IP traffic in 2021 (Cisco 2021). Performant software tools are required for economical science analysis using these datasets. Even for science cases with less stringent latency requirements, analysis needing more compute time per image than the effective observing cadence would fall unrecoverably behind.

Figure 1.5 Argus Pathfinder installed at the Pisgah Astronomical Research Institute in Rosman, NC (front container). The second shipping container houses ArgusSpec (Galliher et al. 2022b), a dedicated spectroscopic followup system, and a "service module" with computing and climate control equipment.

In addition to these logistical concerns, data pipelines for transients searches often have science requirements for minimal latency, so that candidate sources can be rapidly identified for spectroscopic followup and classification. Examples of bespoke pipelines optimized for minimal latency are presented in Perrett et al. (2010), Kumar et al. (2015), Cao et al. (2016), Förster et al. (2016), and Andreoni et al. (2017). Such pipelines are often built around difference image analysis, a method for isolating sources with variable flux by subtracting an earlier reference image of the field, complicated by the need to match the seeing-limited point spread functions (PSFs) of images from multiple epochs. Methods for subtracting images in the presence of variable PSFs have historically included deconvolution with a matching kernel

(Alard & Lupton 1998; Bramich 2008; Becker 2015), which can be computationally expensive and numerically unstable. Recent developments in image subtraction include the statistically optimal ZOGY method (Zackay et al. 2016), which requires a robust and static model of the image PSF, and the Saccadic Fast Fourier Transform SFFT method (Hu et al. 2022), a GPU-based technique that fits a spatially-varying PSF in a per-pixel δ-function basis.

Section 1.5: Outline of this Work

In the following chapters of this text, I will describe my efforts to detect, characterize, and ultimately make discoveries in the rapid time domain sky using the Evryscopes and the prototypes of the Argus Optical Array. The chapters are organized as follows.

In Chapter 2, I describe the Evryscope Fast Transient Engine (EFTE), a pipeline for identifying candidate transient events in image data using a simplified image-differencing algorithm. This algorithm was developed for the unique instrument parameter space of the Evryscopes. While this algorithm produces competitive results with other source detection algorithms, the significant advantage it provides is minimal execution time, enabling real-time searches within the two-minute Evryscope cadence using only a single computer, located on-site at each observatory.

Chapter 3, I present VetNet, a secondary pipeline which analyzes the candidates produced by EFTE, using a combination of machine learning, technical metrics, and science-driven filters to remove false positives from the stream of candidates and identify the “needle in a needle stack” representing the astrophysical phenomena of interest.

Exploration of a previously unexplored parameter space of bright and fast transient events also revealed a new parameter space of bright and fast contaminants to our data. In Chapter 4, I present the first-ever quantitative measurements of the impact of millisecond-scale reflections from satellites and debris in Earth orbit, and find that they are extremely common, outnumbering astrophysical sources in the same brightness regime by orders of magnitude.

In Chapter 5, I describe a program to observe stellar flares detected by EFTE in real time with time-series spectroscopy from the Southern Astrophysical Research (SOAR) telescope. This program has produced the highest time- and spectral-resolution survey of flare spectra from typical M-dwarfs (*i.e.*, stars that are not notably active relative to the M-dwarf population) ever assembled. In this chapter, I present initial results from this program, characterizing the evolution of the spectral components of the flare and modelling the characteristic temperature of their white-light continuum evolution.

In Chapter 6, I introduce the Argus Optical Array, a new, much larger system based on the design concept of the Evryscopes (now with a parity inversion). I led the early effort to prototype the physical hardware of the system, resulting in the construction of a nine-telescope Argus Array Technology Demonstrator (A2TD), which was used for design iteration of core systems and components for the instrument and collection of representative data.

In Chapter 7, I present the Argus Hierarchical Data Processing System (HDPS), a successor to the EFTE pipeline built with scalability to the cluster-scale compute necessary for the 12 Tbps data production rate of Argus. HDPS was developed in parallel with the hardware for Argus, and includes both real-time transient detection capabilities and the control and operating system for the observatory itself.

Finally, in Chapter 8, I conclude with an overview of the capabilities of the Argus Pathfinder and Argus Optical Array to search for rapid transients, as well as an overview of other projects to which I have made significant contributions, but which lie outside of the scope presented here.

Section 1.6: Additional Work and Contributions

Beyond the work enumerated in the following chapters, I have made significant contributions to the following publications as a coauthor. The bibliographic information, along with my specific contributions to each, are listed below.

1. Howard, W. S., Tilley, M. A., Corbett, H., et al. 2018a, Astrophysical Journal Letters, 860, L30, “10.3847/2041-8213/aacaf3” – I assisted with the initial data validation, photometry of the flare peak in Evryscope data, and analysis of the serendipitous, simultaneous, and spectroscopic HARPS data.

2. Ratzloff, J. K., Law, N. M., Fors, O., et al. 2019a, Publications of the Astronomical Society of the Pacific, 131, 075001, “10.1088/1538-3873/ab19d0” – I contributed to the description of the Evryscope data analysis pipeline, and to characterization of on-sky performance from coaddition.

3. Ratzloff, J. K., Law, N. M., Corbett, H. T., Fors, O., & del Ser, D. 2020a, Journal of Astronomical Telescopes, Instruments, and Systems, 6, 018002, “10.1117/1.JATIS.6.1.018002” – I contributed modelling of the Evryscope PSF as a function of position to illustrate the effect of the robotic alignment system.

4. Glazier, A. L., Howard, W. S., Corbett, H., et al. 2020, The Astrophysical Journal, 900, 27, “10.3847/1538-4357/aba4a6” – I assisted with statistical analysis and developed a tool to produce astrometric image cutouts from Evryscope images.

5. Wee, J., Blagorodnova, N., Penprase, B. E., et al. 2020, The Astrophysical Journal, 899, 162, “10.3847/1538-4357/aba3cc” – I contributed an analysis of the Evryscope lightcurve of the nova and context for the Evryscope detections [previously reported in Corbett et al. (2018)].

6. Law, N. M., Corbett, H., Galliher, N. W., et al. 2022c, Publications of the Astronomical Society of the Pacific, 134, 035003, “10.1088/1538-3873/ac4811” – I contributed an overview of the Argus Array pipeline and data products, and a description of the multi-messenger and FRB science cases for Argus. I also wrote the appendix justifying the choices of telescopes and cameras for the Array.

Finally, data products from the Evryscope Fast Transient Engine (EFTE; Chapter 2) and Evrypipe, an earlier iteration of the Evryscope pipeline which I developed in collaboration with Octavi Fors, have proven useful for a variety of science cases. Papers resulting from the products of the Evryscope pipelines which are unrelated to the fast transients science case, or to which I have made only minor contributions, are listed below.

1. Tokovinin, A., Corbett, H., Fors, O., et al. 2018, The Astronomical Journal, 156, 120, "10.3847/1538-3881/aad694"
2. Kosiarek, M. R., Crossfield, I. J. M., Hardegree-Ullman, K. K., et al. 2019, The Astronomical Journal, 157, 97, "10.3847/1538-3881/aaf79c"
3. Howard, W. S., Corbett, H., Law, N. M., et al. 2019, The Astrophysical Journal, 881, 9, "10.3847/1538-4357/ab2767"
4. Howard, W. S., Corbett, H., Law, N. M., et al. 2020, The Astrophysical Journal, 895, 140, "10.3847/1538-4357/ab9081"
5. Howard, W. S., Teske, J., Corbett, H., et al. 2021, The Astronomical Journal, 162, 147, "10.3847/1538-3881/ac0fe3"
6. Ratzloff, J. K., Corbett, H., Law, N. M., et al. 2019b, Publications of the Astronomical Society of the Pacific, 131, 084201, "10.1088/1538-3873/ab1d77"
7. Ratzloff, J. K., Barlow, B. N., Kupfer, T., et al. 2019c, The Astrophysical Journal, 883, 51, "10.3847/1538-4357/ab3727"
8. Ratzloff, J. K., Barlow, B. N., Németh, P., et al. 2020b, The Astrophysical Journal, 890, 126, "10.3847/1538-4357/ab64f3"
9. Quimby, R. M., Shafter, A. W., & Corbett, H. 2021, Research Notes of the American Astronomical Society, 5, 160, "10.3847/2515-5172/ac14c0"

10. Powell, B. P., Kostov, V. B., Rappaport, S. A., et al. 2021, The Astronomical Journal, 162, 299, "10.3847/1538-3881/ac2c81"
11. Sokolovsky, K. V., Johnson, T. J., Buson, S., et al. 2023, arXiv e-prints, arXiv:2302.03043, "10.48550/arXiv.2302.03043" *accepted, MNRAS*

CHAPTER 2: THE EVRYSCOPE FAST TRANSIENT ENGINE[1]

In this Chapter, I present the Evryscope Fast Transient Engine (EFTE), a real-time discovery pipeline for the Evryscopes. The primary goal of EFTE is to provide a reliable event stream with sufficiently minimal latency to enable multi-wavelength followup of events with sub-hour durations. EFTE also provides useful general-purpose utilities for interacting with and analyzing Evryscope data, including a quick-look photometry pipeline independent of the general-purpose precision-photometry pipeline, a custom astrometric solver, and CCD calibration functions. EFTE is mostly written in Python, with some compute-intensive routines (stamp extraction and photometry) implemented in C and wrapped as Python extensions using Cython (Behnel et al. 2011).

To fit within the existing network infrastructure at the observatories, EFTE is designed to operate with minimal computational resources for data analysis; a single co-located compute node supports each Evryscope site. Low resource requirements are particularly necessary when looking towards next-generation sky surveys, such as the Argus Optical Array (Law et al. 2022b;c). The upcoming Argus Array Pathfinder instrument, consisting of thirty-eight 20 cm telescopes, will produce up to 180 TiB of data per night at 1-second cadence and 6 TiB of data per night at the base 30-second cadence; maximizing science returns from data-intensive systems like Argus will require time- and cost-efficient algorithms and pipelines. For Argus, all images must be reduced within the observing cadence to provide sufficiently low latency for followup and to avoid a backlog of data, which can require runaway compute resources for “catch-up.” Incoming Argus images are resampled to a pre-defined HEALPix (Górski &

---

[1] This chapter adapted from Corbett et al. (2023), published in the *Astrophysical Journal Supplement Series*. The full bibliographic entry for the paper is as follows:
Corbett, H., Carney, J., Gonzalez, R., et al. 2023, The Astrophysical Journal Supplement Series, 265, 63, “10.3847/1538-4365/acbd41”

Hivon 2011) grid using a custom GPU-based code. By parallelizing direct subtraction based on the EFTE algorithm, the Argus pipelines are able to reduce each image into transient candidates and compressed images in an average of of 925 ms. Corbett et al. (2022) presents a full description of the Argus Array pipelines and data reduction strategy.

The Chapter is organized as follows. In Section 2.1, I outline the overall design and implementation details of the pipeline. In Section 2.2, I describe the initial image calibration and data quality controls for the pipeline. In Secion 2.3, I outline the process of locating each image on sky and solving for the mapping between image and sky coordinates. In Section 2.4, I formulate a direct image subtraction algorithm, suited to the unique science requirements and data properties of the Evryscopes. In Section 2.5, I present an approach to measuring the brightness of stars in Evryscope images using forced aperture photometry with a spatially-varying zeropoint. In Section 2.6, I describe the in-database, high-speed cross-matching system used to associate both transient candidates with previous detections and with a variety of external reference catalogs. Finally, in Section 2.7, I characterize the typical performance of the components of EFTE using a representative sample of on-sky data from Evryscope.

Section 2.1: Pipeline Architecture

EFTE is a hierarchical + distributed system, with two analysis servers on-site at MLO and CTIO streaming reduced data products back to a central PostgreSQL[2] relational database on campus at University of North Carolina at Chapel Hill (UNC-CH). The analysis servers each have dual AMD EPYC processors (36 CPU cores for Evryscope-North, 48 for Evryscope-South), and 512 GiB of RAM (384 GiB at Evryscope-North). The asymmetry between the two sites is due to the additional four years of archival data from Evryscope-South. The central database for reduced data products is hosted on a 36-core server with 24 TiB of flash storage, located on-campus at UNC-CH. This server also hosts a backend application for

---

[2] http://www.postgresql.org/

pipeline monitoring, associating EFTE transients with external alerts, and end-user reporting via a Slack[3]-based web-interface.

In real-time operation, EFTE instances on each analysis server communicate with the Evryscope data acquisition system via a TCP socket connection, receiving notifications for each incoming image once it has been written to a shared network filesystem. EFTE maintains a per-ratchet, in-memory database of recent images to be matched for image subtraction, spawning subprocesses for all analysis tasks. Figure 2.1 shows the primary components of the EFTE pipeline, from the moment that an image is written to disk to reporting candidates.

Section 2.2: Image Quality Monitor and CCD Calibration

Once an exposure is completed, the Evryscope observation daemon sends a TCP packet to an EFTE instance running on the analysis server. Upon receipt of this notification, EFTE will asynchronously record basic metadata including camera, timing, origin, and instrument configuration to the central database located at UNC-CH. Before further reduction, the image goes through a series of general quality assurance steps, including:

- verification of the file against the checksum recorded by the acquisition system
- instrument configuration checks for camera cooling, dome status, and exposure type
- autocorrelation-based checks for tracking errors and alignment failures
- sky-background measurement for saturation and linearity checks.

If these conditions are satisfied (as they are for 98% of images), the image is converted from ADU to electron units and matched to dark and flat fields for CCD calibration.

Dark frames are regularly regenerated using frames taken at the beginning and ending of each night. Cameras are cooled to a constant $-20°C$ during observing, but some few-percent level drift in bias level is observed as a function of the camera external temperature. We

---

[3] https://slack.com/

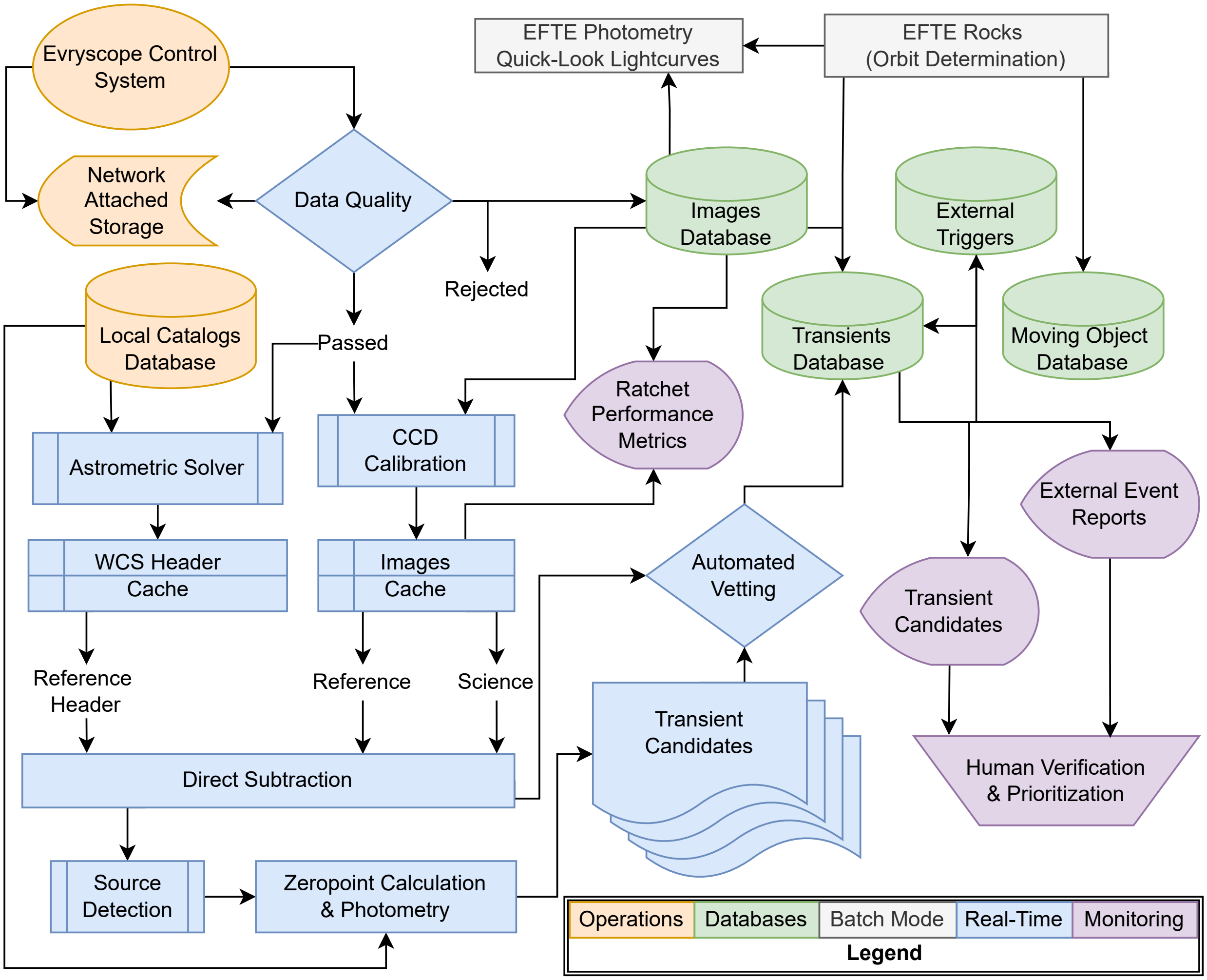

Figure 2.1 Data flow and layout of the EFTE pipelines. Operations (orange), and real-time reduction (blue) components are independent for each observatory, while pipeline monitoring (purple) and shared databases (green) collate data from both Evryscope-North and Evryscope-South.

believe that this is caused by temperature gradients across the readout electronics, and make a quadratic correction to the bias level as a function of the camera electronics temperature, as measured by an on-board sensor in each camera. Additionally, a small ($< 1\%$) linearity correction is applied per pixel based on a cubic fit to pixel value vs. exposure time in lab testing. The linearity correction was determined to be near-identical for all our sensors.

Because of the extreme single-camera field of view, twilight flats contain significant sky gradient that the Evryscope is unable to compensate for through diverse pointings because of its fixed camera positions. Instead, we use photometric flats, calculated based on a 7th order polynomial fit to the normalized flux offsets of reference stars relative to g-band catalog photometry from the ATLAS All-Sky Stellar Reference Catalog (ATLAS-REFCAT2; Tonry et al. 2018). These frames capture the average vignetting patterns of the individual cameras, which can change sharply at the edge of the field. Photometric flat fields are stable at the 1% level over months-long timescales due to focus stability of the Evryscope Robotilter alignment system (Ratzloff et al. 2020a), and are regenerated only when the instruments are cleaned, which typically requires replacing or removing the outer optical windows on each camera.

Bad pixels are replaced with the median of the surrounding 3×3 pixel block and then assigned an arbitrarily high uncertainty in the resulting noise image used for photometry and source detection. Parts of each camera's field of view, particularly those near the center of the frame, will have undersampled PSFs. Simple bad-pixel masking (*i.e.,* assigning pixels a `NaN` or 0 value) will produce sharp artifacts in subsequent analysis requiring pixel resampling, like the image subtraction described in Section 2.4.

Section 2.3: Astrometric Solutions

In parallel with the science-frame calibration steps, the EFTE pipeline produces an astrometric solution for the image using a custom solver developed for the highly distorted Evryscope focal plane. Evryscope astrometric solutions begin with an initial solve based on the center 512×512 pixel region using a local install of `astrometry.net` (Lang et al. 2010). This solution is only used to locate the center of the image. Sources in the image are then cross-matched against the Tycho-2 catalog (Høg et al. 2000), and the offsets are used to optimize a polynomial distortion solution to 5th order in each of x, y and radial position on the sensor, plus cross terms. The solution is then verified against a subset of bright stars from Gaia DR2 (Gaia Collaboration et al. 2018) based on crossmatch performance against detections in an even grid of 15 different sensor regions using the following requirements:

1. $> 80\%$ recovery in at least 7 regions

2. $< 50\%$ recovery in 0 regions
3. Uncertain recovery (due to source confusion or non-detections) in no more than 2 regions.

We selected Gaia DR2 for solution verification due to its reference epoch (J2015.5) coinciding with the beginning of Evryscope observations. Typical RMS offsets from Gaia DR2 positions are ~ 4 arcseconds, or 0.3 pixels.

The complete solution is written into a world coordinate system (WCS) header using the TPV convention for distortion polynomials (Calabretta et al. 2004). The TPV representation is an extension to the standard tangential projection, including additional terms for a general polynomial correction.[4] Due to atmospheric refraction and tracking errors, the solution must be recalculated per-image, but the solver is able to start with a pre-computed baseline distortion solution, averaged over dozens of fields for each camera. We found that starting with an averaged solution decreased the time required for the final optimization by a factor of several on average.

This header is archived to network storage, and serialized and passed back into the in-memory EFTE matching database, where it is associated with the camera and active field. Finally, a footprint of the image, discretized as a GeoJSON (Butler et al. 2016) polygon, is stored in the central database, where it is indexed using PostGIS[5] extension to PostgreSQL, which provides a variety of spatial object types. These footprints support a variety of use-cases, and allow users to easily query for images containing a given target, or search for images intersecting with arbitrary sky regions that can be represented as polygons, such as probability skymaps for gravitational wave and GRB triggers.

---

[4] https://fits.gsfc.nasa.gov/registry/tpvwcs/tpv.html

[5] http://postgis.net/

Section 2.4: Direct Image Subtraction

Like most optical transient surveys, EFTE isolates objects with changing flux by subtracting each science image from an earlier reference frame of the same field from each image. We optimize our subtraction algorithm for speed rather than statistical optimality, electing for per-pixel operations requiring no additional intermediate data products beyond those produced in the initial photometric pipeline. Due to the short (sub-hour) timescales of interest and the dominance of instrumental optical effects on the system PSF, Evryscope images do not require PSF-matching techniques addressed by standard difference-image analysis routines, like HOTPANTS (Becker 2015) or ZOGY (Zackay et al. 2016). However, EFTE was built for extensibility, and implementations of both HOTPANTS and ZOGY are included in EFTE.

The resolution of Evryscope images is limited by the optical distortions from the camera lenses and pixel scale, rather than atmospheric effects, under most practical observing conditions. PSFs vary greatly across the image plane of each camera, as illustrated in Figure 2.2; however, Evryscope image quality metrics have been measured to be repeatable at the few-percent level over many-month timescales (Ratzloff et al. 2020a), creating highly repeatable PSFs for each individual camera.

As a result, we adopt a straightforward algorithm for image subtraction in which the reference and science images are aligned, matched in flux, and subtracted directly. The difference of the two images is then weighted by a propagated uncertainty image to identify significant changes in flux. This approach is valid only if the following conditions are satisfied for the reference and science image couplet:

- Observed PSFs are dominated by telescope optics and pixel scale, and do not vary significantly as a function of observing conditions on the timescale of the lag between the images

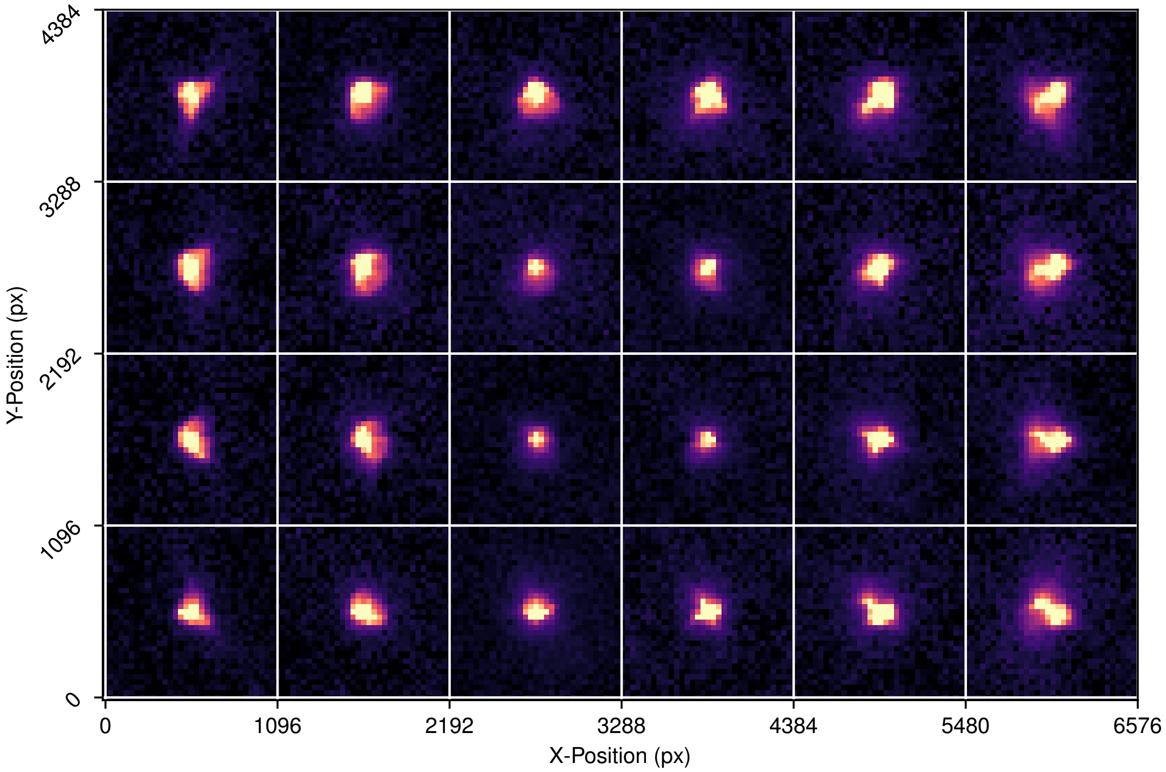

Figure 2.2 Median PSFs across a 6 × 4 grid of sensor regions. PSF variability as a function of chip position is evident; however, long-term measurements of Evryscope optical stability (Ratzloff et al. 2020a) indicate that the PSF is repeatable in time despite aberrations.

- All sources have near-identical pixel coordinates in both images, offset by no more than the PSF-coherence scale, which we define as the pixel distance over which spatial PSF variation is less than thermal and atmospheric effects over a few-minute baseline, or to a 1% maximum change in the normalized PSF. This scale is typically ~ 10 arcminutes, or ~ 50 pixels at Evryscope pixel scale
- The global flux scaling between the two images is smooth

In the following subsections, we describe the process by which we match image couplets for subtraction, and the custom method we use to subtract the images that is optimized for the unique resolution and time domain covered by EFTE.

2.4.1 Reference and Science Image Selection

The primary science targets for the EFTE survey are stellar flares, which have characteristic optical rise-times of minutes. As a result, there is minimal benefit from producing reference frames widely spaced in time from our science images to maximize sensitivity to slowly varying objects. Instead, the image-matching daemon uses a sliding reference frame, taken from the same pointing as the science image. The Evryscopes maintain a consistent pointing over the course of a ratchet, with only few-arcminute drift even at the equator, meaning that the PSF for a given star is essentially constant during each two-hour tracking period, up to resampling effects caused by its sub-pixel position in the 13.2 arcsecond pixels. Additionally, using a reference image from the same pointing means that the science and reference frames are taken under near-identical sky conditions, minimizing the amount of flux scaling necessary.

In the most aggressive case, we could simply subtract consecutive images to achieve near-ideal consistency between the new and reference frames. However, immediate re-use of science images as reference images limits the survey sensitivity to only transients with a detectable change over the two-minute image interval, making confirmation images of highly impulsive events unlikely. In practice, we enforce a short lag, Δt_D, between the reference and science images. Δt_D is typically chosen to be 10 minutes. Over 10 minutes, field drift due to polar alignment error is consistently less than 10 arcminutes (50 pixels). PSF variability over 50 pixels typically produces sub-percent subtraction artifacts, and image registration between the two images can be done with simple transformations with minimal loss in astrometric precision (see Section 2.7.2).

Image re-use effects are also evident at $\Delta t_D = 10$ minutes, but only after the potential fourth confirmation image. Figure 2.3 shows this image-reuse effect on a real flare seen on-sky, in which the same image is both the first science image and last reference image for the transient. While the amplitude and rise time of this event enabled multiple detections up to

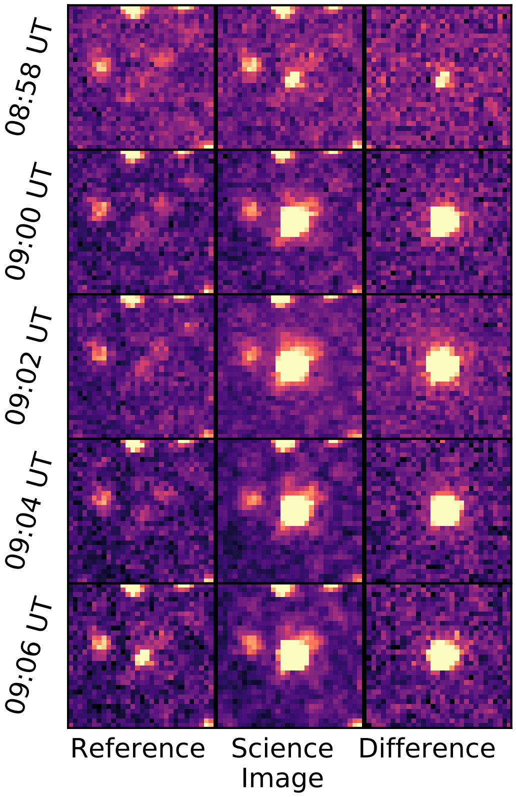

Figure 2.3 EVRT-192099, a 5.5 magnitude flare from a star associated with the 1RXS J174441.6-531551 in the ROSAT All-Sky Survey Bright Source Catalogue (Fresneau & Osborn 2009; Voges et al. 1999). The reference frame from 2019 October 4 at 9:06 UT is the science image from 8:58 UT, showing the sliding reference frame used by our direct subtraction algorithm.

8 minutes after the initial detection, events with shorter rise-times or lower amplitudes may only be detected in a single epoch.

Additionally, the sliding reference frame causes photometry in the unscaled difference image (*i.e.,* the numerator of equation 2.2) to be relative in time. Light curves of EFTE candidates are computed using forced aperture photometry in the science images, as described in Section 2.5.

Over the course of a ratchet beginning with images A, B, C, D, E and F, the pipeline will perform the following subtractions: B-A, C-A, D-A, E-A, and F-B (continuing on to the length of a ratchet, typically 60 images). The rise-time sensitivity of the pipeline increases as a function of the time delay Δt_D between the science image and the previous image from the same pointing chosen as a reference image. Δt_D is in general a tunable parameter of the pipeline which could be increased to trade the viability of the assumptions enumerated above (and thus higher false positive/false negative alert rates) for increased sensitivity to slower rise times. Given sufficient computing, multiple instances of EFTE can run in parallel, enabling sensitivity to different science targets.

2.4.2 Image Registration

Because of the sliding reference frame selection, drift between the science and reference images amounts to a maximum of a few pixels during real-time operations that must be corrected. Additionally, small offsets can have significant effects on the sampled PSF. As such, the images must be carefully aligned and resampled to match both in position and PSF.

For the first image in a ratchet, EFTE must wait for an astrometric solution. However, the astrometric solution for subsequent images from each camera can be inferred by alignment to the first image. The effects of image registration on astrometry performance are addressed in Section 2.7.2. Bootstrapping the astrometric solution in this way reduces delays in the real-time subtraction process due to the astrometric solver to once per ratchet, on the first image. For image alignment and resampling, we use WCS-independent asterism-matching, using the Python *AstroAlign*[6] package (Beroiz et al. 2020) to calculate a rigid transformation between the two images and perform quadratic resampling.

Alternately, in cases where a full WCS solution is available for both images (e.g., in batch reductions not conducted in real-time) the reference and science image can be aligned by resampling the images to a common grid using their WCS solutions using the Astropy-affiliated package *Reproject*. This has the advantage of allowing for non-rigid transformations and accounting for the effects of varying per-pixel sky area across the sensor plane. While astrometric warping due to atmospheric diffraction is negligible for typical Δt_D values used for

---

[6] https://github.com/toros-astro/astroalign

real-time reduction, WCS-based resampling is necessary for longer baselines and inter-night comparisons for fixed fields.

2.4.3 Flux Scaling

Despite the minimal baseline between the reference and science image, we fit a multiplicative flux scaling factor to the reference image to remove any discrepancies with respect to the science image due to variations in transparency and sky brightness, which is particularly important for observations during twilight conditions. Because each individual Evryscope camera covers a large sky area, we allow the flux scaling factor to vary across the image based on the results of forced aperture photometry.

First, we divide each image into 24 × 16 274-pixel square regions of equal pixel area, and select several thousand bright stars from the ATLAS Refcat2. We then calculate the sigma-clipped mean flux ratio between the science and reference images for stars in each of the 384 image sectors, and interpolate this back to full resolution using cubic splines. Finally, the flux-matched reference image $R_m(x, y)$ is calculated from the original, calibrated reference image $R(x, y)$ and the spatially varying flux ratio $F(x, y)$ as

$$R_m(x, y) = R(x, y) * F(x, y). \tag{2.1}$$

To calculate the uncertainty in the flux ratio, we calculate the standard deviation of the flux ratios for reference stars in each region and then interpolate across the full field of the image using cubic splines. The flux ratio uncertainty is propagated forward into the noise characterization for the reference image. Figure 2.4 shows a typical low-resolution flux ratio map for a pair of images with $\Delta t_D = 10$ minutes, showing an average 1.7% change in transparency between the images with some internal structure. The magnitude of the scaling is consistent with transparency changes due to airmass for a camera placed at the edge of the array. Small-scale structure, when present, tends to move smoothly between images and is likely caused by high clouds.

Depending on the science program, flux scaling can be skipped during reduction to minimize latency. For consecutive-image subtraction ($\Delta t_D = 2$ minutes), we neglect flux scaling effects, as the uncertainties in the flux scaling dominate the final noise budget for the image, and the flux scaling is typically sub-percent under normal observing conditions. The primary driver of these uncertainties is likely the sub-pixel response function (sPRF), which is highly local on the Evryscope image sensors, causing the effect to not average out beyond the 1-3% level when interpolating across the image plane. Instead, multiple, slightly offset measurements of the sample star must be modeled simultaneously, as they are for the precision photometry pipeline and in coaddition of multiple images of the same field. However, we include the flux ratio for longer-baseline subtractions, where background variations can dominate over systematics.

2.4.4 Error Analysis and the Detection Image

To identify significant changes in the difference image, we need a robust accounting of the noise sources in each image. For each science and reference image, we model a spatially varying background based on sigma-clipped and interpolated mesh using `sep`, a Python implementation of the core routines from `SExtractor` (Bertin & Arnouts 1996; Barbary 2016). The standard deviation of the background s_B is also measured at this step, based on the sigma-clipped standard deviation. s_B is treated as an empirical measure of the Gaussian noise contributions to each image, including the readout noise and dark current uncertainty. We note that this approach can overestimate the noise due to Poisson contributions from unresolved background star light, and as a result, the detection significance in the direct subtraction image will tend to be an underestimate, particularly in crowded fields (*e.g.,* near the galactic plane).

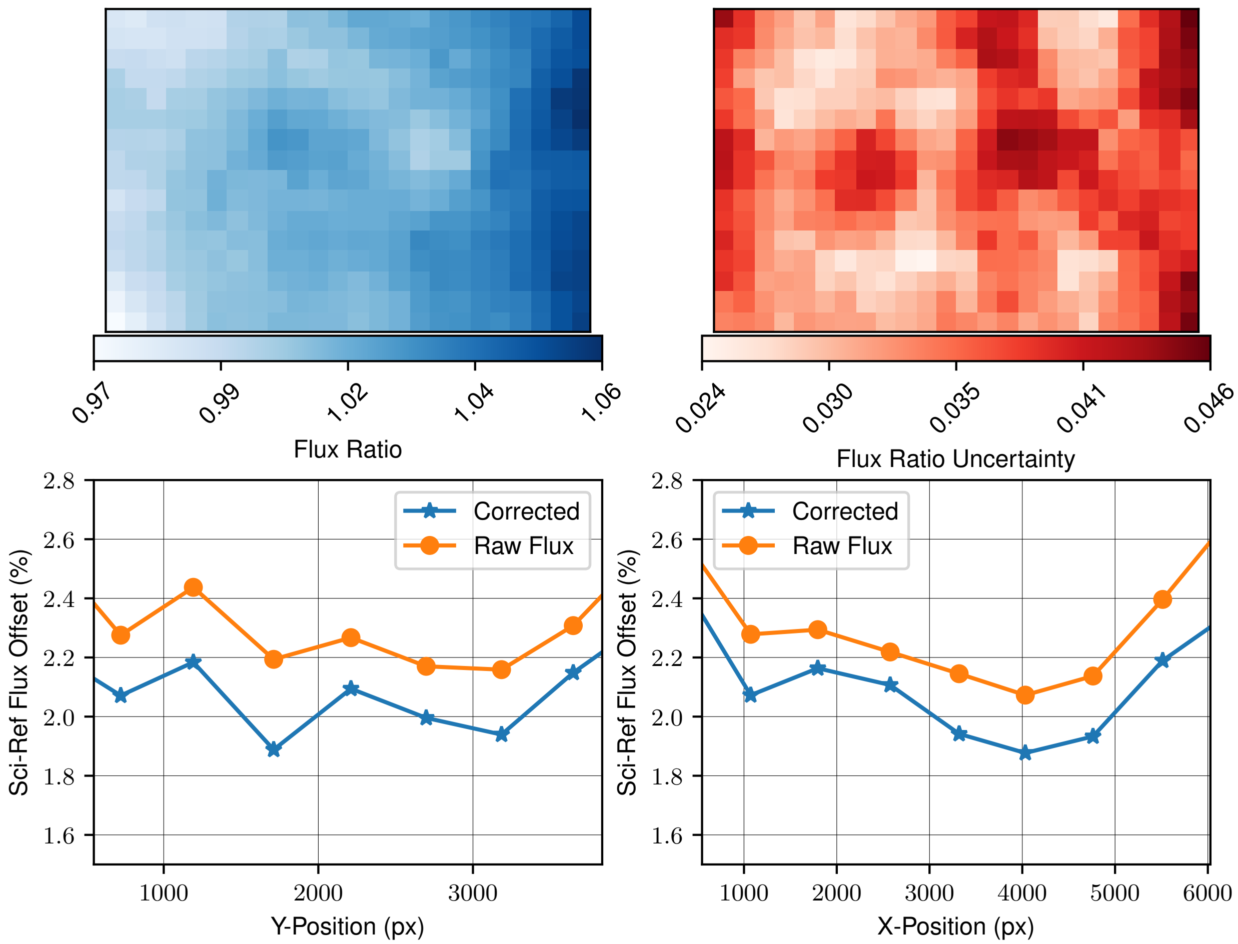

Figure 2.4 **(Top-Left)** Map of the flux ratio between a science and reference image couplet, and **(Top-Right)** the corresponding flux ratio error map. The flux ratio is measured based on forced aperture photometry of several thousand reference stars, and is interpolated across each full-resolution, single-camera image based on the observed flux ratio in an equally spaced grid of 384 image sectors. **(Bottom)** Relative aperture flux residuals before and after correcting with the interpolated flux ratio as a function of x- and y-position on the sensor. The correction improves the flux match between images by $< 1\%$, which is not significant for short ($\Delta t_D = 2$ minute) subtraction baselines. Increases in the flux offset at the edges of the image are caused by aperture losses due to the variable Evryscope PSF.

For a given combination of science image $S(x,y)$ and flux-matched reference image $R_m(x,y)$, both in electron units, the detection image $D(x,y)$ is defined as

$$D(x,y) = \frac{S(x,y) - R_m(x,y)}{\sqrt{s_S^2(x,y) + s_R^2(x,y)}}, \tag{2.2}$$

where s_S^2 and s_R^2 are the total noise images for S and R_m, given by

$$s_S(x,y) = \sqrt{S(x,y) + s_{BS}^2(x,y)}, \tag{2.3}$$

and

$$s_R(x,y) = R(x,y)\sqrt{\frac{R(x,y) + s_{BR}^2(x,y)}{R^2(x,y)} + \frac{s_F^2(x,y)}{F^2(x,y)}}, \tag{2.4}$$

where $s_{BS}(x,y)$ and $s_{BR}(x,y)$ are the measured background standard deviation maps of the science and reference images, respectively, $F(x,y)$ is the flux ratio between the two images, and $s_F(x,y)$ is the spatially varying uncertainty in the flux ratio. $D(x,y)$ image is the simple difference in the two images, scaled by the combined per-pixel uncertainty. The detection image has units of standard deviations. We again use `sep` to mask the detection image at the desired threshold and identify sources.

Figure 2.5 shows an example of an image couplet in a crowded field, along with the resulting direct subtraction image. We also include subtraction images produced using the HOTPANTS and ZOGY algorithms (Becker 2015; Zackay et al. 2016). Direct subtraction produces more false positives (488) than ZOGY (299 in S_{corr}) at the 3-σ threshold, but two orders of magnitude fewer than HOTPANTS (12,258). While ZOGY is a computationally efficient approach, direct subtraction is faster by a factor of ten, largely due to the requirement to calculate a PSF model for ZOGY. Using the direct detection image, we can identify three astronomical transients with the EFTE pipeline using the vetting procedures described in Section 3.1.

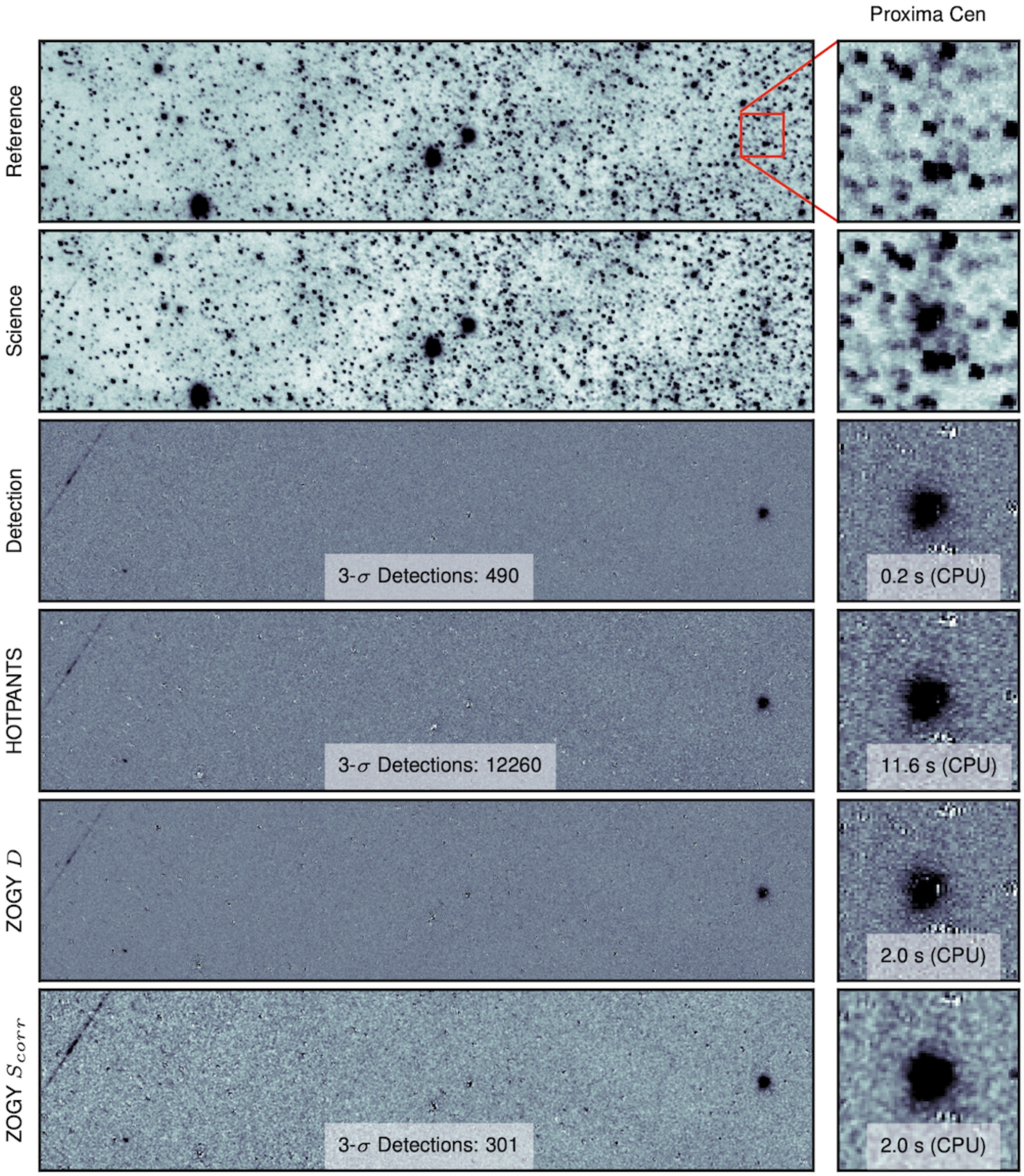

Figure 2.5 **(Left)** A 4° × 1° region near Proxima Centauri from a reference, science, and subtraction images from EFTE, the High Order Transform of PSF and Template Subtraction algorithm (HOTPANTS; Becker 2015), and the Zackay, Ofek, and Gal-Yam algorithm (ZOGY; Zackay et al. 2016). For ZOGY, we include both the scaled S_{corr} image used for point source detection and the proper difference image D. In the subtraction images, a faint satellite streak (left), variable star (bottom left), and M-dwarf super flare (Howard et al. 2018a) (far right) are successfully recovered. The EFTE direct subtraction produces 47% more 3-σ false positive than ZOGY for this field and can be computed is 10× faster for this image size. **(Right)** Cutouts from the left images showing the $1' \times 1'$ region centered on Proxima Cen.

Section 2.5: Photometric Zeropoints and Forced Photometry

To calibrate magnitudes for EFTE transient candidates to a standard photometric system, we build a spatially varying photometric zeropoint based on a subset of the ATLAS Refcat2, a composite catalog consisting of *griz* data from the AAVSO Photometric All-Sky Survey (APASS; Henden et al. 2016), Pan-STARRS Data Release 1 (Flewelling et al. 2016), Skymapper Data Release 1.1 (Wolf et al. 2018), Tycho-2 (Høg et al. 2000; Pickles & Depagne 2010), the Yale Bright Star Catalog (Hoffleit & Jaschek 1991), Gaia DR2 (Gaia Collaboration et al. 2018), plus original data from the ATLAS Pathfinder survey. To ensure that stars used for determining the zeropoint of the image are well-exposed, but not saturated, we select a subset of the catalog between $10 < g' < 12$. We also exclude stars with colors redder than $g - r = 1.5$ that might bias the photometry due to unconstrained chromatic aberrations affecting the PSF. We calculate an instrumental magnitude for each of the reference stars using a forced aperture at the catalog position in the background-subtracted and calibrated science image, typically with an aperture radius of 3 pixels (40 arcseconds).

To model the variation in photometric zeropoint across the field of view, the science image is divided into an 8×12 grid of square subframes, each of which subtends 4 square degrees and contains O(100) reference stars. Within each subframe, we calculate the sigma-clipped median offset between the instrumental magnitudes calculated via aperture photometry and the catalog values. The offsets in each region are then smoothly interpolated over the rectangular mesh of the full-sized using quintic splines to produce a spatially varying zeropoint $z(x, y)$. The resulting image has units of magnitudes and has as its values the photometric zeropoint at each pixel, defined such that

$$m_g = -2.5 \log_{10} F_{aper} - z(x, y), \tag{2.5}$$

where F_{aper} is the measured flux from aperture photometry.

Finally, we calculate magnitudes for each candidate detected as described in Section 2.4.4, based on their centroid positions in the detection image. Centroids are calculated for each candidate by computing their value-weighted average position ("center of mass"). This process uses a custom aperture photometry routine, implemented in Cython for the Evryscope precision photometry pipeline (Ratzloff et al. 2019a), on the science image.

Section 2.6: Candidate Crossmatching and Source Association

EFTE candidates from both sites and their corresponding metadata are stored in a relational database. On insert, candidates are associated with previous candidates at the same position, which collectively form an "event," via an insert trigger within the database. If a candidate has no antecedent, a new event is created, and an additional trigger crossmatches the new event's position with a variety of externally produced reference catalogs. At time of writing, these reference catalogs include the International Variable Star Index (VSX; Watson et al. 2020), the Galaxy List for the Advanced Detector Era (GLADE; Dálya et al. 2018), ATLAS Refcat2, and the ASAS-SN Catalog of Variable Stars (Jayasinghe et al. 2018). Stellar sources are crossmatched with a radius of 26 arcseconds (corresponding to 2 Evryscope pixels and the worst-case astrometric performance for EFTE detections - see Figure 2.9), and galactic sources from GLADE are crossmatched with a 1 arcminute radius.

To accelerate the in-database crossmatching and candidate queries, all candidates, events, and reference catalogs are indexed using the Quad Tree Cube (Q3C) pixelization scheme,[7] a PostgreSQL extension for efficient spherical crossmatching and radial queries (Koposov & Bartunov 2006). Sky areas, such as the on-sky footprints of images or probability contour regions for multi-messenger transient events, are indexed using PostGIS with a custom non-geodetic projection. This projection does not include the WGS-84 (Kumar 1988) reference ellipsoid, and represents the right ascension and declination in the standard barycentric celestial reference system in all EFTE application code.

---

[7] See: https://ascl.net/1905.008 (Koposov & Bartunov 2019)

Candidates can also be crossmatched against external triggers received by EFTE via automated circulars from the NASA Gamma-ray Coordinates Network/Transient Astronomy Network (GCN). Alerts are inserted in the central database by an automated ingest microservice, where they are indexed by position either using Q3C for tightly localized triggers, or as PostGIS polygons for events that are distributed as polygon skymaps, like LIGO/Virgo skymaps (Abbott et al. 2009) or GRB alerts from the Fermi Gamma Burst Monitor (Fermi GBM; Bhat et al. 2009).

Section 2.7: Pipeline Performance Evaluation

2.7.1 Photometric Solutions

To evaluate the performance of the photometric calibration using a smoothly varying zeropoint, as described in Section 2.5, we compare single-epoch forced photometry from 3,217,215 catalog stars from the ATLAS Refcat2 across 500 randomly selected images from the 2018 observation year. The images were required to pass the quality assurance metrics described in Section 2.2, but were not otherwise filtered for sky or instrumental conditions. Figure 2.6 gives the distribution of photometric offsets and offset RMS as a function of magnitude in individual images. The resulting photometry is calibrated to the reference catalog with an RMS offset of 0.05 magnitude between $8 < m_g < 14.0$, measured using 5 iterations of a 5-σ clip to remove outliers due to single-epoch failures.

These numbers likely represent an upper limit on photometric RMS for isolated and dim events, as the distribution is dominated by source confusion beyond $g' = 14$ (e.g., dim catalog stars with a brighter star near or within the 6-pixel aperture), causing anomalously bright and high-precision measurements of dim catalog sources. Sources brighter than $g' = 9$ are occasionally saturated when they appear near the center of the image, though typically, sources as bright as $g' = 8$ are well-calibrated and linear. There is a noise floor around $\sim 5\%$ for single-epoch detections from Evryscope due to variation in the sub-pixel response across the image plane. These effects are modeled in data products from the Evryscope precision

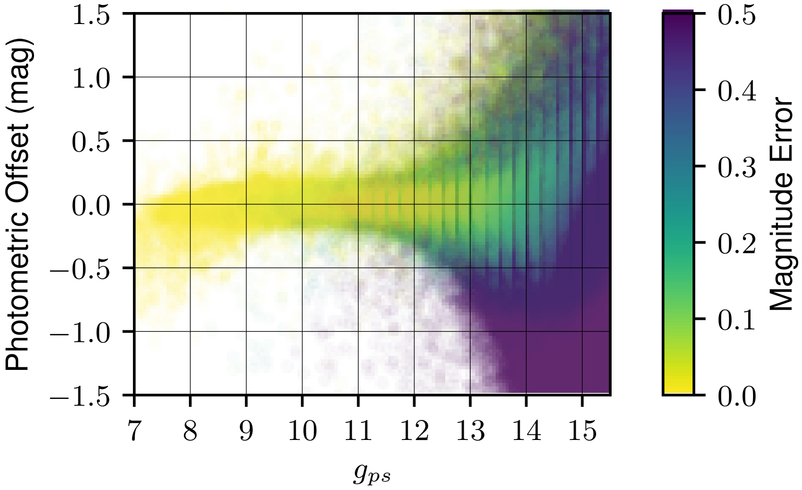

Figure 2.6 Photometric calibration offsets between the ATLAS All-Sky Photometric Reference Catalog and EFTE. Median RMS offset in the region $8 < m_g < 14.5$ is 0.06 magnitude. Anomalously bright and high-precision measurements (upper right) are due to source confusion and blending. Under-reporting of magnitudes due to saturation is evident for stars brighter than $g' = 8$.

photometry pipeline (Ratzloff et al. 2019a), but are prominent in raw single-epoch bright-star photometry from EFTE.

Additional color and airmass terms can be applied to light curves of EFTE photometry as needed, using the equation

$$g_{EVR} = g_{PS} + A + B(g_{PS} - r_{PS}) + k_1 X + k_2 X(g_{PS} - r_{PS}), \tag{2.6}$$

where g_{EVR} is the magnitude in Evryscope g-band, g_{PS} and r_{PS} are the PanSTARRS magnitudes from the ATLAS reference catalog, X is the airmass of the star, and A, B, k_1, k_2 are fitted photometric conversion factors between the Evryscope and PanSTARRS bandpasses. Based on fits to forced-aperture light curves using a robust estimator (Fischler & Bolles 1981), the average photometric conversion terms across all cameras are $A = 0.037 \pm 0.002$, $B = -0.051 \pm 0.004$, $k_1 = 0.021 \pm 0.002$, and $k_2 = -0.051 \pm 0.003$. The light curves used to fit these parameters were chosen from a random sample of 25,000 Northern Hemisphere stars, which we then filtered based on a quality metric which includes source variability relative to nearby stars, saturation, and the shape of the aperture flux growth curve, leaving a cleaner sample of 10,671 lightcurves with an average of 17,140 epochs.

Figure 2.7 shows the photometric offset as a function of $g-r$ and $g-i$ colors before and after applying the calibration offset, as well as the resulting impact on the long-term photometric accuracy of light curves. Application of the color and airmass correction brings the RMS calibration accuracy of long-term light curves from 0.16 mags to 0.06 mags, in line with the single-epoch measurements above.

Public EFTE data products, including both transient alerts and long-term photometric light curves , do not include color and airmass terms. For light curves , calibration for photometric precision, rather than accuracy, is prioritized. Evryscope light curves are first decorrelated from subpixel PSF variations, and then detrended using a customized version of the SysREM algorithm (Tamuz et al. 2005) to correct for systematics, ultimately producing light curves that are self-consistent at the $\leq$20 mmag level at the bright end of Evryscope's operating range, as shown in Figure 2.8.

2.7.2 Astrometric Localization

The custom astrometry routines developed for the Evryscopes are capable of providing 1-2" (0.08-0.15 pixel) RMS astrometry over the field of view of the Evryscopes in single images; however, astrometric localizations from EFTE also depend on the quality of the alignment procedure used for real-time reduction, and must therefore be characterized separately. In addition to the sub-pixel scatter induced by photon noise, EFTE localizations depend on the consistency of the pointing between consecutive images and the accuracy of the rigid transformation calculated to align each image with the previous image for which a WCS solution is available.

We evaluated the quality of this alignment routine by performing source detection in individual science images aligned to a previous target image in the same pointing. We

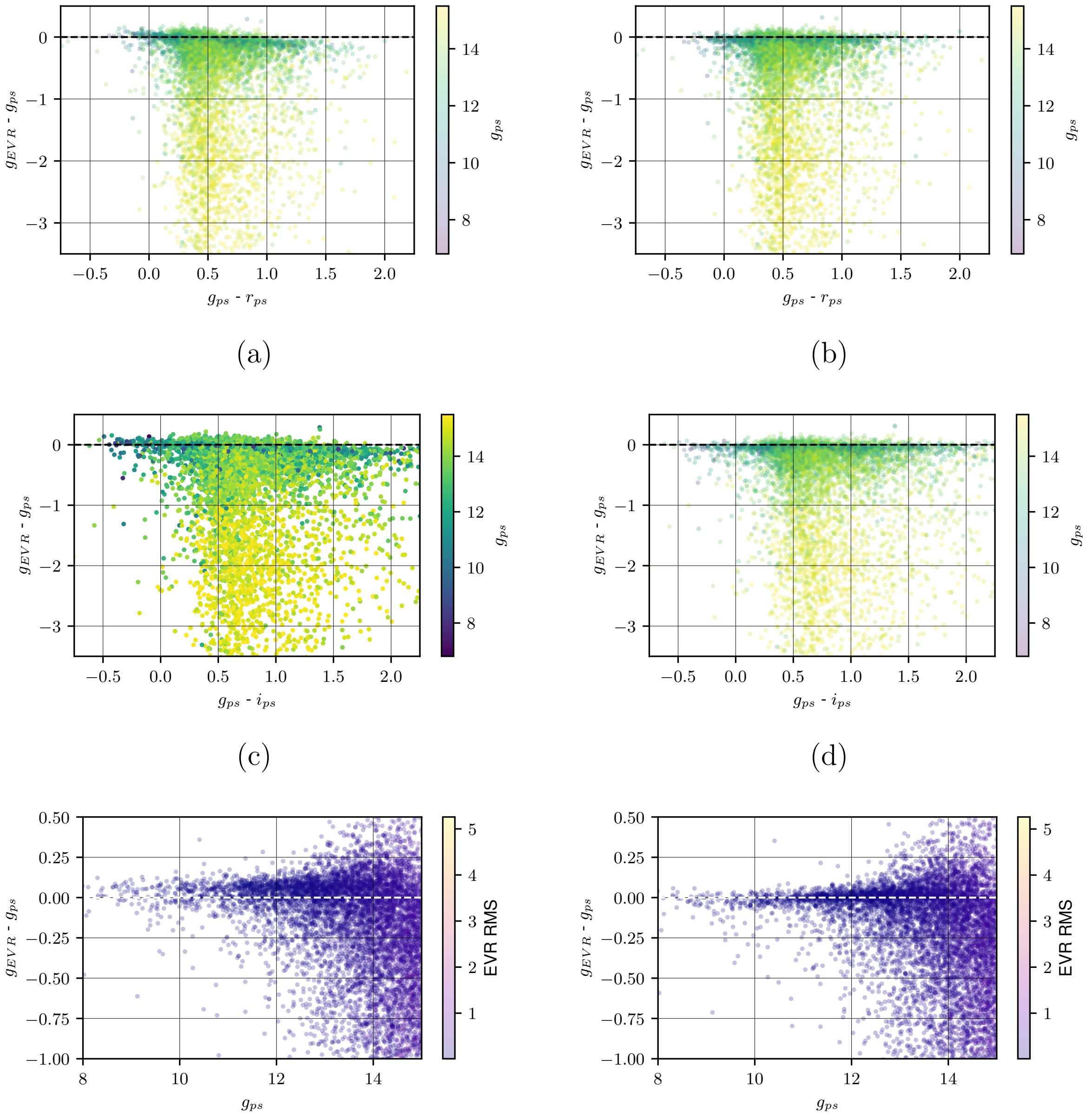

(a)

(b)

(c)

(d)

(e)

(f)

Figure 2.7 **(a)**, **(b)** Photometric offsets between Evryscope and PanSTARRS g-band as a function of $g - r$ before and after calibration with the color and airmass terms above, respectively. Large offsets below the linear trend are caused by blended sources and low-SNR detections that were not filtered based on the light curve quality metric described in Section 2.7.1. **(c)**, **(d)** Same as above, but with $g - i$ colors in place of $g - r$ to demonstrate perfomance over a wider variety of colors. No calibration fits are made as a function of i-band colors. **(e)**, **(f)** Photometric calibration performance for many-epoch light curves as a function of magnitude. The sigma-clipped RMS photometric offset decreases from 0.16 mags to 0.06 mags for sources between $14.5 > m_g > 8$ with application of color terms.

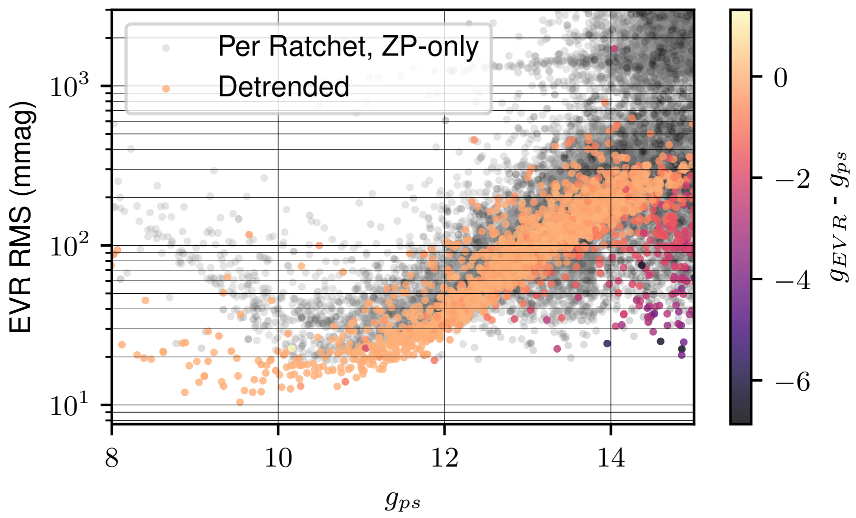

Figure 2.8 Measured RMS of 10,671 randomly selected, long-term Evryscope light curves. Performance in the detrended lightcurves ranges from 20 mmag at the bright end to 20% for dim sources. RMS for raw light curves is an average of the measured RMS in each pointing, neglecting zerpoint offsets between ratchets.

chose target images with a typical Δt_D of 10 minutes, with samples of $\Delta t_D < 10$ minutes representative of what would occur in the first few images in a ratchet.

The detected sources were then cross-matched with sources in the ATLAS Refcat2 (Tonry et al. 2018). As in Section 2.7.1, 500 science images for testing were randomly selected from the 2018 observing data set, across all weather and Moon conditions. Figure 2.9 shows a histogram of the offsets between the catalog positions and the recovered positions in the aligned science image with a re-used WCS solution. Astrometric performance was sub-pixel for 99% of detected sources, with an RMS scatter less than 4 arcseconds between 8th and 14th magnitude. As for the photometry, precision is limited by saturation effects at the bright end, and by source confusion for sources dimmer than 14.5. In all cases, the localization is accurate to within 2 pixels.

2.7.3 Candidate Production Latency

To enable rapid followup, EFTE must produce candidates on timescales comparable to the earliest and most impulsive phases of the astrophysical events of interest, ideally within

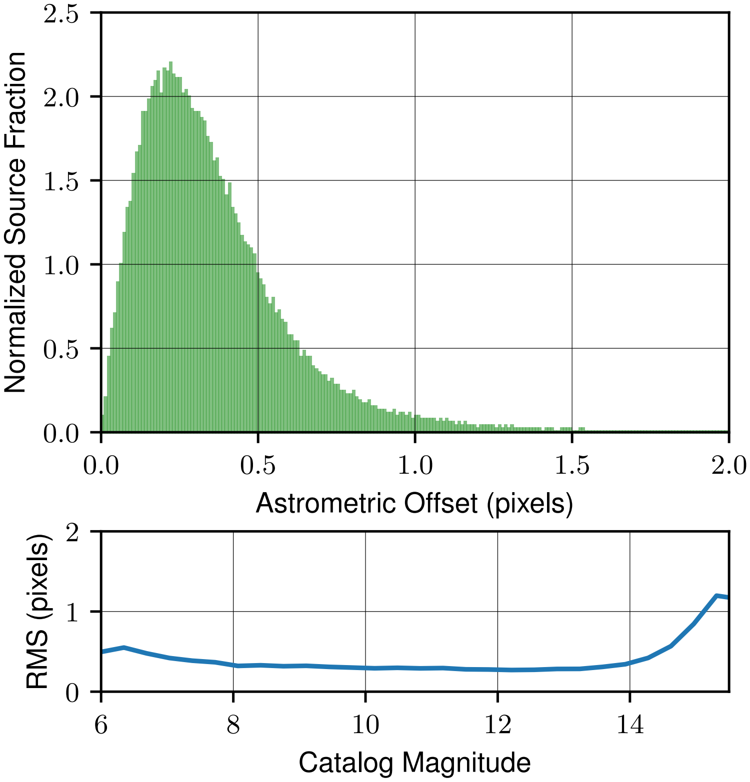

Figure 2.9 (**top**) Astrometric localization performance for the EFTE pipeline, and the RMS localization scatter as a function of magnitude (**bottom**). Performance is sub-pixel at the 99th percentile, with a typical RMS scatter of 7”, excepting stars brighter than 7th magnitude, which are typically saturated, and dimmer than 14th magnitude, where source confusion dominates in the source extraction.

the base cadence of the survey. For Evryscope, this means adding candidates to an actionable event stream within two minutes of the end of each exposure. We consider the candidate production latency as our figure of merit for speed, defined here as the time delay between the shutter close time for the image and candidates being fully inserted into the central EFTE database in Chapel Hill, with all automated vetting and in-database source association and deduplication actions complete.

Figure 2.10 presents histograms of candidate production latency for both Evryscope-North and Evryscope-South during early on-sky testing of EFTE between 25 November 2019 and 1 January 2020. Some variation is seen between Evryscope-North and Evryscope-South, which we attribute to a combination of the difference in on-site compute hardware specifications, camera counts, and varying network connectivity to each observatory.

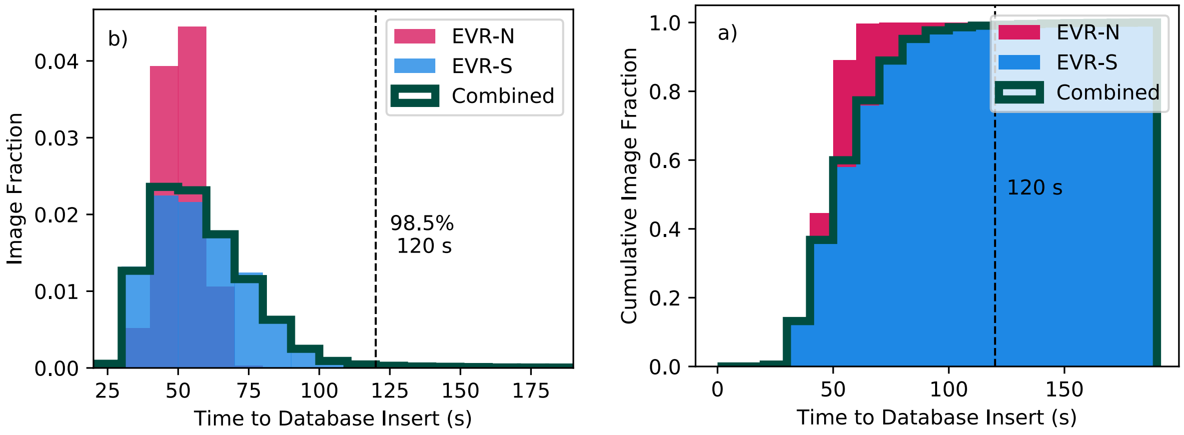

(a) (b)

Figure 2.10 Cumulative histogram (**a**) and distribution (**b**) of time delay between exposure and insertion of vetted candidates into the remote database between 25 November 2019 and 1 January 2020. 98.5% of images are fully reduced into lists of transient candidates within 120 seconds, before the next image is complete.

Cumulatively between both sites, EFTE is able to meet the sub-cadence latency requirement for 98.5% of images.

2.7.4 Injection-Recovery Testing for Completeness

To estimate the expected completeness of the survey, we selected 800 images from the 2021 Evryscope-North data set at random and injected simulated sources using the routine described in Section 3.1.8, and evaluated the recovery probability as a function of magnitude using the routine described in Corbett et al. (2020). The ratio of variables (injected with a minimum contrast of 0.25 mag) to transients without a counterpart in the reference image was 1:6. In total, 960,000 transients were added to the images.

Figure 2.11 shows the fraction of simulated transients recovered from the test set, and the corresponding recovery fraction from Corbett et al. (2020), which used an earlier version of the VetNet model. We note that dropping the VetNet-RB score threshold to 0.0 has a marginal effect on the dim end recovery curve, indicating that the decreased depth (50% at $m_g = 14$ instead of 50% at $m_g = 14.2$) is a property of the slightly different image sample rather than of the updated VetNet model. Sources brighter than $m_g = 13.2$ are successfully

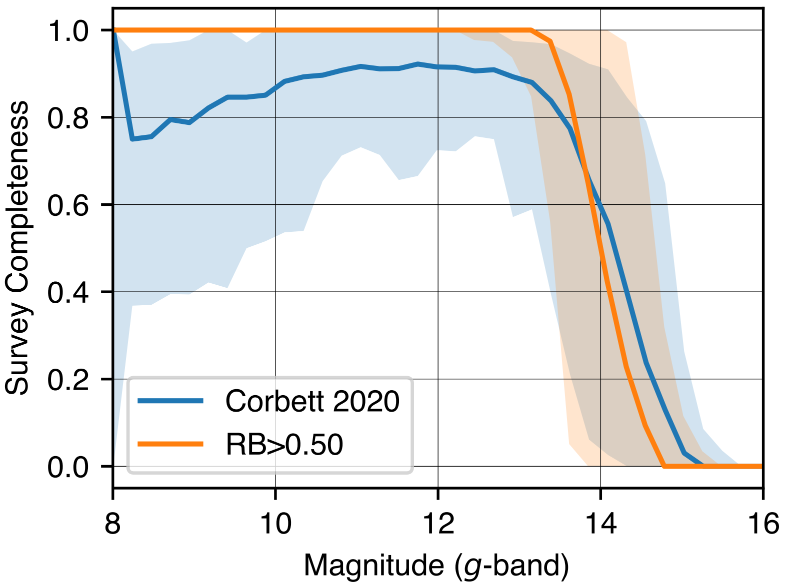

Figure 2.11 Survey completeness as a function of magnitude for both the current EFTE with a threshold VetNet real-bogus score of 0.5, and the previous version described in Corbett et al. (2020). Completeness is measured on a synthetic sample of injected transient and variable sources. Recovery probability for sources brighter than $m_g = 13.2$ is 99.9%, and rapidly falls to 50% at $m_g = 14$. Shaded regions represent the 90% confidence intervals of each curve, based on the percentiles of the per-image recovery functions.

recovered in all images.

CHAPTER 3: VETNET: REAL-BOGUS FILTERING FOR THE EFTE EVENT STREAM WITH CONVOLUTIONAL NEURAL NETWORKS[1]

Section 3.1: Automated Vetting

Despite the optical consistency of Evryscope images chosen for subtraction, the direct subtraction process produces thousands of false positives per image. Observed sources of false positives are plentiful from inside the CCD sensors out to Earth orbit, including:

- Cosmic ray muon tracks
- Compton recoil electrons from radionuclides in materials at the observatory
- Optical ghosts
- Registration and astrometric errors
- Persistent residual charge from bright stars remaining after cycling the detectors
- Flat-fielding errors
- Aircraft strobes
- Tumbling satellites and debris (Corbett et al. 2020)
- Noise artifacts from both photon and astrometric noise.

In total, the event rate from these sources can outnumber the real, on-sky rate of astrophysical transients by orders of magnitude. Human candidate inspection remains

---

[1] This chapter adapted from Corbett et al. (2023), published in the *Astrophysical Journal Supplement Series*. The full bibliographic entry for the paper is as follows:
Corbett, H., Carney, J., Gonzalez, R., et al. 2023, The Astrophysical Journal Supplement Series, 265, 63, “10.3847/1538-4365/acbd41”

standard, but it is not scalable to surveys producing hundreds of thousands of candidates per night. As a result, a reliable, efficient, and automated vetting system for candidates is a core component in any transient survey producing an actionable event stream that can be delegated to followup resources.

Some false-positive sources in the list above can be identified with simple filters: Bright streaks from satellites involve thousands of pixels, and residual charge from bright stars can be flagged based on previous astrometric solutions. Other classes of observed signals can be difficult to identify from simple metrics in all scenarios. To account for this, we use a combination of data cuts based on explicit filters and machine learning (ML) methods.

ML classifiers require large datasets of labelled examples to identify the complex latent associations that form a model. In general, there are two options for producing these datasets; simulation or human classification. Exclusively training on simulated data is risky; the efficacy of the final model is dependent on how representative the simulations are of real data. However, human classification is labor-intensive, and prohibitive at the level of producing thousands or even millions of labelled examples across a representative sample of the survey.

As a result, we have adopted a compound approach, using both hand-labelled on-sky data and simulated events produced via PSF injection. The simulated dataset was used to train an intermediate decision tree model to pre-screen events for human labelling, and to perform initial training of the deep learning model. The real, moderate-purity sample produced by the intermediate model was then hand-classified by humans, producing a smaller, but minimally-contaminated and representative data sample for training the final deep model.

3.1.1 Initial Candidate Filters

While ML techniques can be comprehensive, simple filters grounded in domain knowledge can be both more efficient and more easily interpreted. Starting from an initial deep source extraction ($SNR > 3$ in a minimum of 1 pixel) of the detection image $D(x, y)$, we implement three first-order quality cuts, removing candidates which meet any of the following conditions:

1. Centroid within 15 pixels of the edge of the CCD
2. Ratio of negative-to-positive pixels within a 6-pixel circular aperture > 0.4[2]
3. More than 750 pixels above the detection threshold

Detections near the edge of a CCD are typically caused by small amounts of mount drift between the science and reference images. Large ratios of negative to positive pixels typically indicate a photon or astrometric noise artifact. Extended events > 750 pixels are commonly bright streaks, caused predominantly by aircraft and LEO satellites.

We apply an additional filter after the ML vetting described below; we reject any candidates coming from a subtraction with more than 500 high-confidence candidates. These failed subtractions rarely occur, and are caused by a doubled or streaked image due to wind shake at the instrument, or a breakdown of the assumption of a slow and smoothly varying sky background required for direct image subtraction, as described in Section 2.4.

With no additional vetting, these simple filters reduce the per-image candidate count to $O(10^2)$ using the baseline values stated above; however, these numbers are readily tunable to the science case and corresponding false positive tolerance, either by modifying a configuration file for the EFTE pipeline instance running at each observatory, or by filtering the database queries used to regularly report candidates to end users. Candidates that pass the thresholds for these filters at the pipeline-instance level are inserted into the central database, including small 30×30-pixel "postage stamp" cutouts around their detection positions.

3.1.2 Intermediate Random Forest Classifier

For the intermediate real-bogus model, we used the scikit-learn (Pedregosa et al. 2012) implementation of the ExtraTrees classifier (Geurts et al. 2006), which is a variant of the Random Forest classifier (Breiman 2001), trained exclusively on simulated transients generated as described in Section 3.1.8. This is a decision tree method, reliant on pre-selected features

---

[2] We note that an earlier version of the pipeline, as presented in Chapter 4, used a less restrictive value for the sign ratio (0.311).

for both training and analysis. The final output of the tree is a score with a range between 0 and 1.0, analogous to the probability that a sample is real.

The training set was generated by processing each injection image (Section 3.1.8) using the direct image subtraction algorithm described in Section 2.4. We identified all sources with a greater than 3-sigma significance in at least a single pixel. Based on the histogram of detection-injection separation distances, we use a threshold of 2.5 pixel for identifying injections recoveries within the detection catalogs. From the injection images, the false-positives outnumber recovered injections 9-to-1. While some on-sky background transients are likely to exist in the injection images, we are assuming that this number is small relative to the number of injections. We recover 2,118,592 injected transients, and randomly select an additional 2,118,592 bogus detections to create a balanced training set. The additional bogus candidates are held back for testing.

For each candidate, we consider 16 features, divided up into two primary categories:

- Photometric parameters, including both calibrated and instrumental magnitudes, the background-subtracted aperture flux, the local background RMS, science image SNR, and the local photometric zeropoint.
- Morphological values, including the windowed second-order moments and uncertainties, ellipticity parameters, and the number of pixels subtended by the source.

3.1.2.1 Hyperparameter Tuning for the Intermediate Model

To choose optimal hyperparameters for the ExtraTrees classifier, we performed a randomized grid search. Additionally, we randomly select whether or not to bootstrap samples for each tree on each iteration. We search across 10,000 iterations, each time training an estimator with 5-fold cross-validation and evaluating its balanced accuracy, defined as the average per-class recall. The selected parameters are given in table 3.1.

Table 3.1 Grid search parameters for initial real-bogus ExtraTrees classifier.

Property	Minimum	Maximum	Steps	**Selected**
Estimators	200	1000	100	**248**
Tree Depth	10	110	100	**67**
Max. Features per Split	2	8	6	**8**
Min. Samples per Split	2	10	8	**2**
Min. Samples per Leaf	1	6	6	**1**

3.1.2.2 Intermediate Model Evaluation

The model is trained using the selected parameters from the grid search, and evaluated using a variety of metrics. We evaluate and characterize the using both cross-validation during training, and a dedicated test held back from training.

During training, we utilize K-Fold cross-validation with $k = 5$. This process entails dividing the training set into five equal “folds”. For each of k iterations, we train the model on four of the “folds”, reserving the fifth for validation testing. This produces five trained models, which collectively utilize every sample in the training set as both training and testing data, allowing us to characterize the variation in the final metrics as a function of small inhomogeneities in the training and validation data. In cross-validation, we consider the balanced accuracy score, which is the average accuracy on real and bogus examples, weighted by the prevalence of each class. The mean accuracy in cross validation is 96.6%, with a standard deviation of 0.4.

Because this model is primarily used to bootstrap an on-sky training set for the deep learning model, it would ideally have high recall, defined as

$$Recall = \frac{TruePositives}{TruePositives + FalseNegatives}. \tag{3.1}$$

The precision of the model, defined as

$$Precision = \frac{TruePositives}{FalsePositives + TruePositives} \tag{3.2}$$

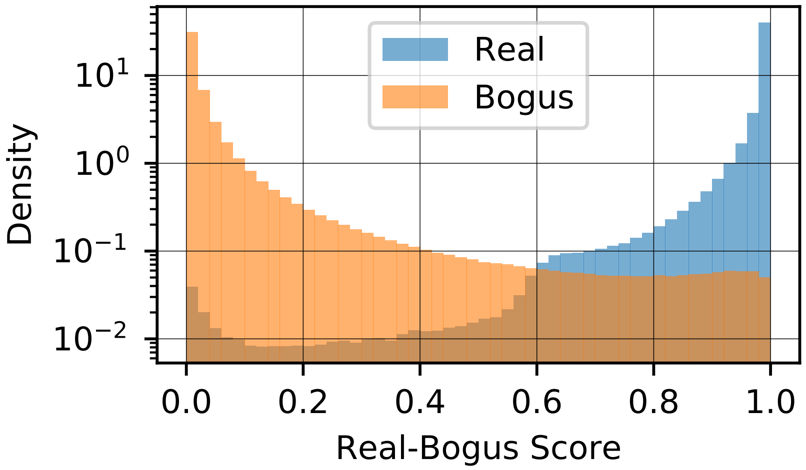

Figure 3.1 Histograms of model scores for the intermediate ExtraTrees model, divided by class.

can be relatively poor, as the results will be vetted by humans before inclusion. Over the test set, the model achieves a near-1.0 precision for bogus events, and a precision of 0.79 for real events. Correspondingly, the recall for bogus samples is 0.97, and 0.99 for real samples. This model is effective at removing bogus samples while maintaining high recall for real samples, at the cost of lower precision for real events. Figure 3.1 shows the score distributions for real and bogus candidates within the test set. With a score threshold at the critical point of 0.6, the model achieves a false positive rate (FPR) of $\sim 2\%$ with a false negative rate (FNR) of $\sim 1\%$.

Figure 3.2 presents a histogram of the number of candidates in the test set as a function of magnitude and score. The distributions are generally uniform as a function of magnitude, with increased uncertainty at the dim end, consistent with the expected degeneracy between dim events, which are likely to be above-threshold in only a single pixel, and common contaminants, like hot pixels and cosmic ray or electron strikes.

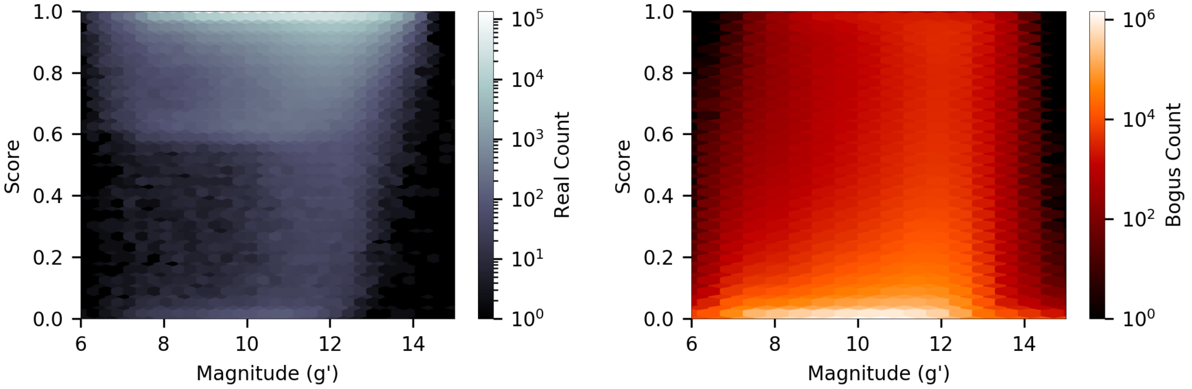

Figure 3.2 Histograms of model scores for the intermediate ExtraTrees model as a function of magnitude. The vertical band of confusion of between 10th and 12th magnitude for real sources likely represents increasing uncertainty for faint sources.

3.1.3 Real-Bogus Classification with Convolutional Neural Networks

For additional reduction of the EFTE false positive rate, we use an ML model based on two-dimensional convolutional layers (LeCun et al. 1989) with weights conditioned directly on image data. This model is a binary ("real/bogus" [RB]) classifier, which assigns each candidate a score between 0 and 1, where a score of 1 indicates that the candidate is likely real. RB classifiers have seen long-standing use in transient surveys, starting with the model built by (Bailey et al. 2008) for the Nearby Supernova Factory (Aldering et al. 2002). Similar approaches have been used for the Palomar Transient Factory (PTF; Law et al. 2009; Bloom et al. 2008), the Intermediate Palomar Transient Factory (iPTF; Brink et al. 2013), the Dark Energy Survey (Goldstein et al. 2015), and most recently, for ZTF (Mahabal et al. 2019; Duev et al. 2019) and GOTO (Killestein et al. 2021).

Deep learning is a type of ML in which "deep" stacks of artificial neural network layers (Mcculloch & Pitts 1943) are used to transform input data into latent-space encodings that can be mapped to the desired output quantities. Convolutional Neural Networks (CNNs) (LeCun & Bengio 1995) are a sub-class of artificial neural networks that build up a latent space representation of pixel data using convolutions, which identify increasingly compressed features of the input as the depth of the network increases, as opposed to requiring preselection of computed - and potentially sub-optimal - features to represent the data. CNNs have found widespread use in astronomy for tasks including source detection and deblending (Stoppa et al. 2022; Burke et al. 2019), in addition to transient real-bogus vetting (Makhlouf et al. 2021; Förster et al. 2016; Duev et al. 2019; Killestein et al. 2021).

In this section, we describe VetNet, a CNN-based vetting algorithm trained to assign real-bogus probabilities to EFTE candidates directly from 30×30 pixel cutouts from the reference, science, and direct subtraction difference images.

3.1.4 Training Set and Data Labelling

Supervised ML classifiers require large datasets of labelled examples to identify the complex latent associations during training. In general, there are two options for producing these datasets: simulation or human classification. Exclusively training on simulated data is risky because the efficacy of the final model is dependent on how representative the simulations are of real data. However, human classification is labor-intensive, and prohibitive at the level of producing thousands or even millions of labelled examples across a representative sample of the survey.

As a result, we have adopted a compound approach, using both hand-labelled, on-sky data and simulated events produced via spatially varying PSF injection. The simulated dataset was used to train intermediate models to pre-screen events for human labelling, including the prototype CNN used in Corbett et al. (2020). We manually classified the on-sky, moderate-purity sample produced by the intermediate model to produce a smaller, but minimally contaminated and representative, data sample for training the production models.

3.1.5 Network Architecture

VetNet uses a sequential, VGGNet-like (Simonyan & Zisserman 2014) model with six trainable layers; four convolutional, and two fully connected output layers. Each set of

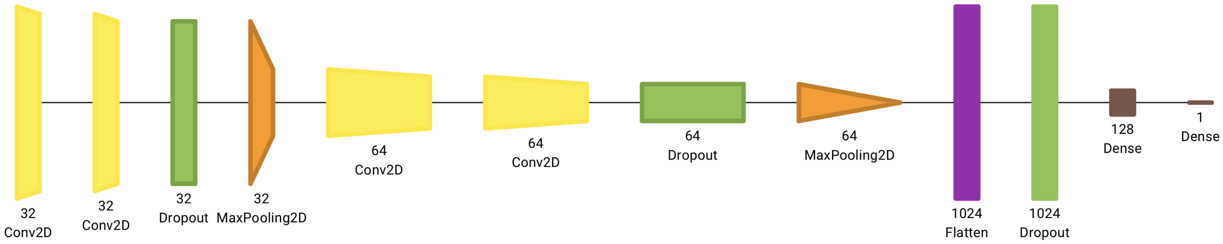

Figure 3.3 Architecture of VetNet, a convolutional real-bogus classifier used by EFTE. The inputs to the network are a triplet of 30×30 pixel cutouts around the center of each candidate, taken from the reference, science, and direct difference images. All trainable layers, save for the final dense unit, use ReLU activation. Pairs of convolution layers are each followed by max-pooling layers and 20% dropout for regularization. Network visualization generated with Net2Vis (Bäuerle et al. 2021).

convolution layers is subject to 20% dropout to prevent overfitting, encouraging the model to build a diverse set of representations of the data distribution. The dropout fraction at each layer was determined using the HyperBand band algorithm (Li et al. 2018) with a binary cross-entopy loss function. Further regularization is provided by a pooling layer, which reduces the dimensionality of each convolution block output by a factor of four. Outputs of each pooled layer are normalized and re-centered on zero using batch normalization (Ioffe & Szegedy 2015) to improve training performance and model stability. All convolution layers use 3-pixel square kernels and ReLu activation (Agarap 2018), save for the final fully connected node, which has a sigmoid activation function that produces an output value normalized between 0 and 1. This output, the VetNet real-bogus (RB) score, can broadly be interpreted as probability that a given candidate is real. Figure 3.3 depicts the architecture of the model, including filter depths and the resulting dimensionality.

VetNet is implemented in Tensorflow (Abadi et al. 2015), using the high-level Keras API (Chollet et al. 2015).

3.1.6 Dropout and Model Uncertainty

CNNs can have an arbitrarily large number of free parameters, and are accordingly able to overfit training data. As a result, methods of regularizing the training process and the weights assigned to the convolutional filters are necessary to maximize performance on actual data at inference time. Dropout (Srivastava et al. 2014) is one common technique, in which a tunable fraction of outputs from a layer are chosen at random and set to zero, preventing them from contributing to the final network outputs.

In addition to slowing overfitting, dropout also can be interpreted as an approximation of Bayesian inference (Gal & Ghahramani 2015a). In this framework, each random sampling of layer outputs can also be considered a sample from the distribution representing network weights in a fully Bayesian network. Evaluating a given sample through these different dropout-induced realizations of the network enables us to similarly approximate the posterior distribution of the network output. The advantage of this approach, called Monte Carlo (MC) Dropout, is that the output distribution includes the systematic uncertainty in the network output due to model selection, distinct from the random uncertainty produced by the variance of the training set (Gal & Ghahramani 2015b). To produce an output from the network, each candidate is processed through multiple dropout-induced realizations of the network, producing a distribution of resulting RB scores. We use the median of this distribution as the RB probability for each source.

Interpretation of MC Dropout is unsettled in the literature (namely, whether it represents a genuinely Bayesian approximation (Le Folgoc et al. 2021)). However, it can be used to produce a number that scales with the degree of consensus within the network and amount of support for a sample within the training set, and that can be interpreted as a confidence metric. This is similar to the interpretation of the sigmoid activation of the network as a whole as a real-bogus probability, despite not representing a normalized probability density function. We adopt the entropy-based metric from Killestein et al. (2021) to quantify the network confidence:

$$\mathbb{C} = 1 - \frac{1}{N} \sum_{i=1}^{N} -p_i \log_2 p_i - (1 - p_i) \log_2 (1 - p_i), \tag{3.3}$$

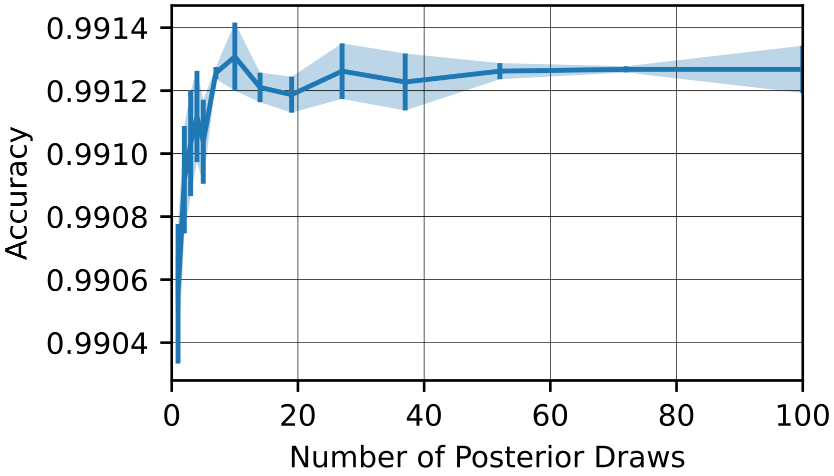

Figure 3.4 Network accuracy vs. number of forward passes through the network for the validation set. Performance converges at 10 samples. Error bars represent the standard deviation of the results across 20 iterations.

where N is the number of samples from the posterior distribution and p_i is the network output for the ith sample. The metric $\mathbb{C}$ is the binary entropy of the Bernoulli process representing real-bogus classification, averaged across posterior draws, and is bounded on the interval $[0, 1]$. In Section 3.2, we demonstrate that $\mathbb{C}$ also matches the subjective confidence of human vetting.

The number of forward passes used to approximate the network output posterior distribution is determined empirically from the validation set. Figure 3.4 shows the accuracy of the classifier as a function of the number of forward passes through the network. The accuracy of the median RB score converges after 10 inferences, which is consistent with the findings in Killestein et al. (2021), despite the dropout rate here being two orders of magnitude higher.

3.1.7 Training Set and Data Augmentation

Two datasets were used to train the VetNet classifier; the 435,452 simulated candidate dataset described in Section 3.1.8, and a human-annotated sample of on-sky detections containing 31,092 candidates flagged as probably real by an earlier iteration of VetNet itself (Corbett et al. 2020). Unlike the simulated dataset, the on-sky data is heavily class-imbalanced, with only 9.6% of examples (2,976) being human-labelled as real. To account for this class imbalance, we randomly exclude 25,140 of the bogus samples from the on-sky dataset, noting that the simulated dataset only contains simulated examples of the *real* class. Bogus examples within the simulated data set are drawn from the same population as the bogus examples in the on-sky dataset. Our approach for maximizing the return from this relatively small sample of on-sky data is described in Section 3.1.9.

We divided the simulated and annotated on-sky datasets into training, validation, and testing subsets using an 80:10:10 ratio. We used validation set for tuning the MC Dropout fractions and the number of posterior draws, and for monitoring the training process.

To extend the effective size of the dataset, random flips and rotations are applied to each batch of training samples. As noted by Killestein et al. (2021) and Dieleman et al. (2015), rotations (other than in 90 degree increments) require interpolation and thus distort the data from the pixel grid; however, in our use case, the data are previously resampled with interpolation by the image alignment process (see Section 2.9). No data augmentation is applied during validation or model evaluation, or for training during fine-tuning with human-annotated data.

3.1.8 Simulated Data Generation

We generated a base training set by injecting simulated transients into 300 randomly selected images across the first two years of full Evryscope science operation at each site. Images were selected uniformly in time, meaning that moon phase, sky conditions, focus changes due to temperature variations, and dust-accumulation on the instrument (leading to measurable changes in the background level and limiting magnitude on few-month timescales) are uniformly represented. Each image was calibrated as in the pipeline (see Section 2.4).

For each image, we generated a uniform sample of 5,000 positions within the image, then deduplicated so that no position was within 50 pixels of any other position to avoid overlapping transients, resulting in an average of 1,200 injections per image. While this does bias the initial training set against contemporaneous, spatially coincident events, this is sufficiently rare that we neglect this scenario. Each injection was assigned a random magnitude, drawn from a uniform distribution bounded between the typical saturation limit of g$\sim$ 7 and the 1.5σ detection limit at the injection position (determined by the photometric zeropoint interpolation procedure described in Section 2.5).

A second round of injections was done to simulate transients with known visible progenitors. From the catalog stars within each image, 500 stars minimally separated by 50 pixels were selected as additional positions for injection. The variability amplitude was uniformly sampled between 0.25 and 8 magnitudes. The upper limit is set by the maximum contrast visible for a pre-detected star in an Evryscope image, *i.e.*, a star at the dim-limit of the survey that reaches the single-exposure saturation limit.

Evryscope PSFs are heavily impacted by optical aberrations, and exhibit a wide variety of morphologies, both between cameras and across the field of view of individual cameras (Ratzloff et al. 2020a), making common analytic profiles (Moffat, Gaussian, Lorentzian) untenable. Further, the coarse pixel scale makes more complex linear models, such as the ePSF (Anderson & King 2000) and those used by PSFEx (Bertin 2011) and `PSFMachine` (Hedges et al. 2021), prone to poor fits due to aliasing and source confusion. We found that the most robust method for simulating transients with morphologically plausible, point-like profiles was to build a model PSF based on nearby, isolated stars. For each injection position, up to 100 nearby stars having a distance less than 137 pixels and significance of 10σ above the local noise are extracted with a 30$\times$30 "postage stamp" window. Each stamp is then multiplied by a smoothly varying (Hanning) window and normalized. The final PSF to be flux scaled and added into the image is the median of the nearby stamp templates, weighted by the relative normalized distance from the injection position and relative flux uncertainty of the template star. Figure 3.5 shows examples of simulated PSFs using this technique across a typical Evryscope focal plane for a range of magnitudes, alongside the resulting signal in a direct subtraction image with a consecutive epoch.

At the end of the transient injection process, the image is "de-calibrated" by adding back in the expected dark current, bias, and background levels, and the image is converted back into ADU units with pixel values beyond the range of an unsigned 16-bit integer truncated, matching the histogram of the simulated images to the distribution expected for science images.

To produce a simulation-augmented dataset, the transient-injected images are reduced using the EFTE pipeline, and any candidates identified within 2 pixels of an injection location are labelled as real, and all others as bogus. Despite the large number of injected sources, this process produces an unbalanced dataset, with artifact detections outnumbering injections at rates up to 1000-to-1. To balance the dataset, we randomly select a number of bogus candidates equal to the number of recovered injections for inclusion in the final data set. This results in a dataset with noisy labels due to both background transients (likely dominated by short-duration reflections from Earth satellites (Corbett et al. 2020; Nir et al. 2021)) and candidates injected below the difference image threshold and recovered coincidentally. From visual inspection of 10,000 injection candidates, uniformly sampled from both known-injections and predicted artifacts, we estimate label contamination to affect $\leq 2.7\%$ of the candidates in the 435,452 candidate dataset. Deep convolutional models have been observed in prior work to be robust to many times this level of label noise (Ghosh et al. 2016; Rolnick et al. 2017).

3.1.9 Staged Training Methodology

A common approach for building specialized models with limited training data is to utilize transfer learning, leveraging the pre-trained feature representations of existing models built with massive related datasets. Rather than training an entire model from scratch, which requires a large annotated dataset over the domain of interest, a pre-trained model can be selectively "fine-tuned" over a representative dataset in a new domain. We adopt a similar approach for making use of the considerable diversity of observing conditions and sky regions

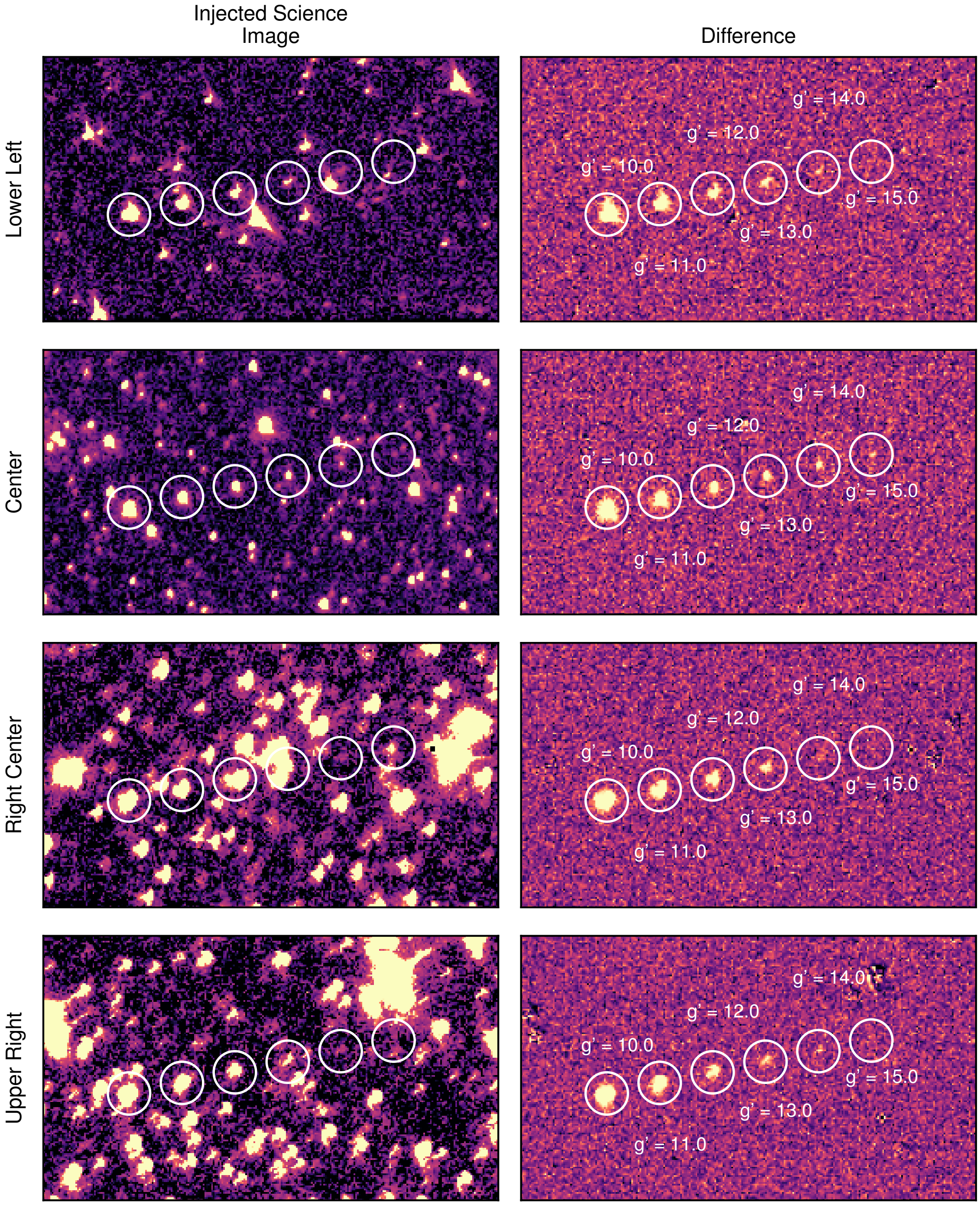

Figure 3.5 **(Left)** Examples of simulated transients with magnitudes $g' = 10, 11, 12, 13, 14, 15$ at the center and edges of a typical mid-galactic latitude Evryscope image. PSFs at each position are modeled as a normalized, aligned, and sigma-clipped combination of nearby isolated stars, producing morphologically plausible, star-like injections. These simulations are used for initial conditioning of our machine-learned vetting system. **(Right)** Difference images for each subimage using a reference frame taken two minutes before the injected science image.

represented in the simulated dataset described in Section 3.1.7, while minimizing the risk of optimizing for properties of the transient injection process (see Section 3.1.8) rather than properties transferable to on-sky data.

Our training curriculum for VetNet was as follows:

1. Train the full model, including all convolutional and fully connected layers, on the simulated dataset until convergence to create the synthetic base model
2. Freeze the weights on all convolution layers from the synthetic base, and re-train the fully connected layers from scratch using on-sky data
3. Unfreeze the convolution layers, train at a minimal learning rate using on-sky data until convergence to produce the final on-sky model.

We used the Adam optimizer (Kingma & Ba 2014) with a binary cross-entropy loss function for all three stages. For the first two training stages, we start with a maximum learning rate of 0.0003, slowed by a factor of two whenever the loss on the validation set plateaued for 10 epochs. Scheduling the learning rate in this way helps the network to converge to a local minimum when near a global minimum and decreases the oscillation around the minimum of the loss function. For the final fine-tuning of the entire model, we reduced the initial learning rate to 0.00001 while maintaining the same scheduled rate decay.

The synthetic base model converges after ∼100 epochs, taking about 6.5 hours when training on an Intel Xeon E5-2695v4 CPU. Fine-tuning with on-sky data converges after ∼150 epochs, but takes less than 10 minutes due to the smaller quantity of data.

In the final stage, we use a single-iteration of the semi-supervised relabelling routine suggested by Killestein et al. (2021); samples in the training set which are classified differently by the network than by human labelers are flipped to the model classification in cases where the model confidence $\mathbb{C}$ is greater than the median. On review, these samples are generally either difficult to classify by hand, with low-significance peaks relative to the surrounding noise, areas of the sensor plane with pathological PSFs, or likely errors in the original labelling

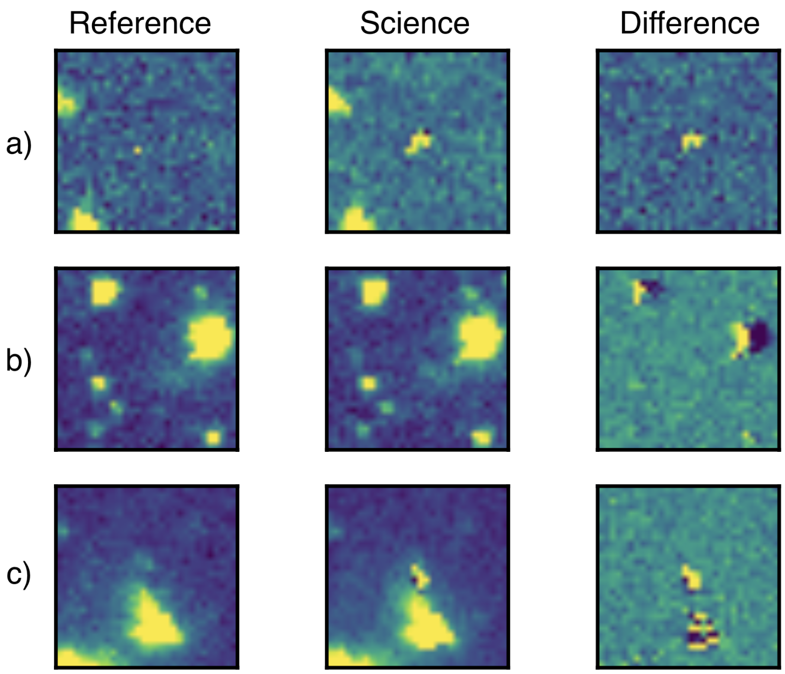

Figure 3.6 Misclassified training set samples re-labelled based on the entropy-based confidence of VetNet predictions. Network reclassifications typically affect samples which are difficult to classify manually. Samples **(a)** and **(c)** were initially classified as real by human vetters, but were relabeled as bogus by the algorithm. Both have pathological PSFs likely caused by interpolation artifacts from resampling near a cosmic ray, particle strike, or unmasked bad pixel. Sample **(b)** is low-significance and off-center, but was manually classified as bogus before being confidently relabelled as real by VetNet.

process. Figure 3.6 shows three representative examples that are re-labelled by VetNet during this process. In total, less than 4.7% of samples are changed in the training set after updating the labels. We note that this is comparable to the label noise in the synthetic dataset (2.7%).

Section 3.2: VetNet Model Evaluation

We evaluated the VetNet CNN model and the intermediate random forest using both the held-back test set described in Section 3.1.7, and an injection-recovery program over a sample of randomly selected images.

3.2.1 On-Sky Test Set

Figure 3.6 shows postage stamp cutouts and classification histograms from the held-back test set of on-sky transients, divided evenly between cases where VetNet classifications and the human-assigned labels agreed and cases where they disagreed. In both categories, the entropy-based confidence score scales with subjective appraisal of the candidates; candidates (h), (k), (i), and (c) are faint borderline detections, assigned accordingly low confidence scores. Candidate (g) is a linear particle collision. Notably, candidates (f) and (l) have anomalously sharp PSFs that were both counted as real by human labellers, but were assigned bogus scores by the network, suggesting that they are morphologically more similar to cosmics. Even in cases where the labels are consistent, the confidence drops in areas with pathological PSFs, as in example (b), but particularly in example (a).

Figure 3.7 shows the performance of the model on the on-sky test set. The magnitude-integrated precision and recall at a VetNet score threshold of 0.5 are 95.4% and 94.4% respectively, with a false positive rate of 5.1%. Depending on the science case and false-alarm tolerance of follow-up resources, these numbers can be tuned using a combination of the VetNet RB score and the $\mathbb{C}$ rating; for instance, a sub-percent FPR is measured above a RB threshold of 0.7.

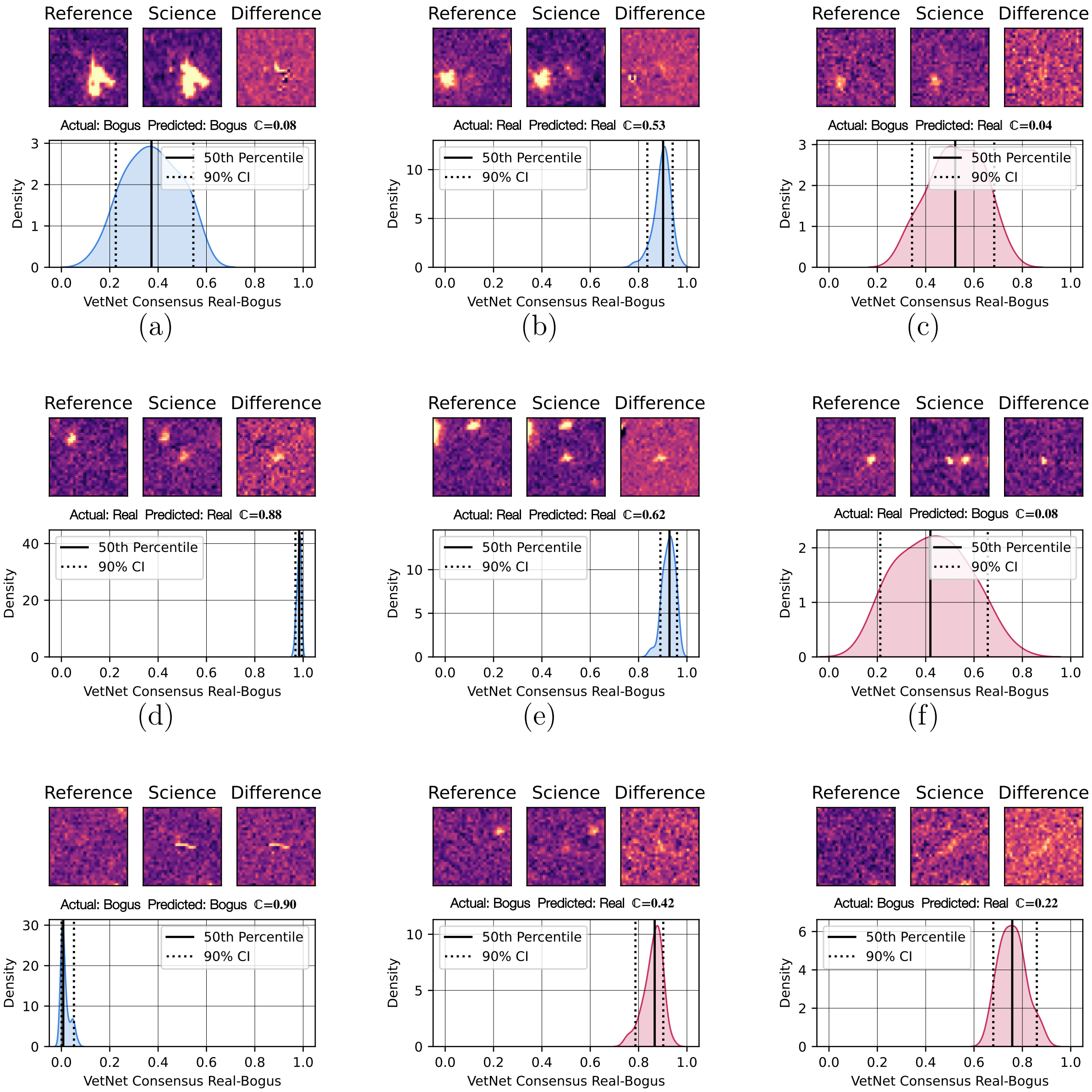
Reference
Science
Difference
Actual: Bogus Predicted: Bogus ℂ=0.08
Actual: Real Predicted: Real ℂ=0.53
Actual: Bogus Predicted: Real ℂ=0.04
Actual: Real Predicted: Real ℂ=0.88
Actual: Real Predicted: Real ℂ=0.62
Actual: Real Predicted: Bogus ℂ=0.08
Actual: Bogus Predicted: Bogus ℂ=0.90
Actual: Bogus Predicted: Real ℂ=0.42
Actual: Bogus Predicted: Real ℂ=0.22
50th Percentile
90% CI
Density
VetNet Consensus Real-Bogus
0.0
0.2
0.4
0.6
0.8
1.0

(a) (b) (c)

(d) (e) (f)

(g) (h) (i)

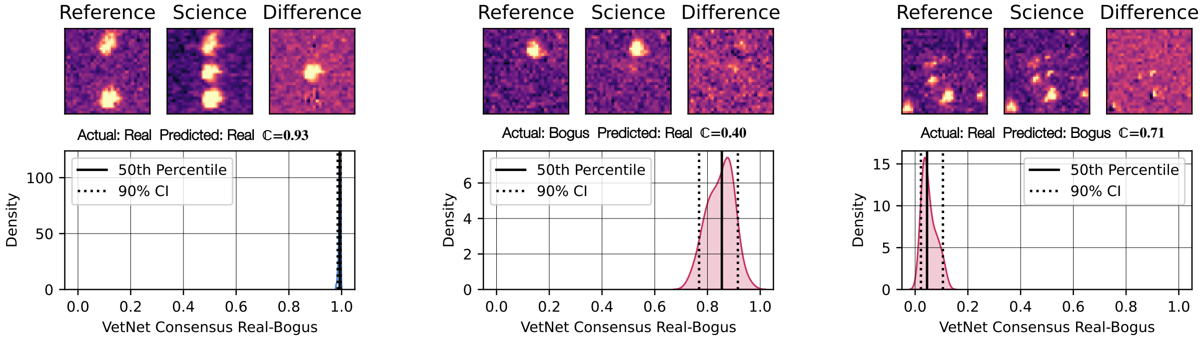

(j) (k) (l)

Figure 3.6 (continued from previous page) Sample on-sky candidates taken from the VetNet test set. “Actual” and “Pred” values represent sky truth class determined by a human inspector and the predicted class by the network, respectively. Histograms are an approximation of the normalized Bayesian posterior distribution for the probability of the candidate representing a real astrophysical event, quantified using the entropy-based $\mathbb{C}$ metric from Killestein et al. (2021). In cases where the sky truth and the network prediction disagree, $\mathbb{C}$ is typically < 0.5, or extenuating circumstances exist, such as the anomalous PSFs in panels **(l)** and **(f)**, or the potential human misclassifications in **(h)**, **(i)**, and **(k)**.

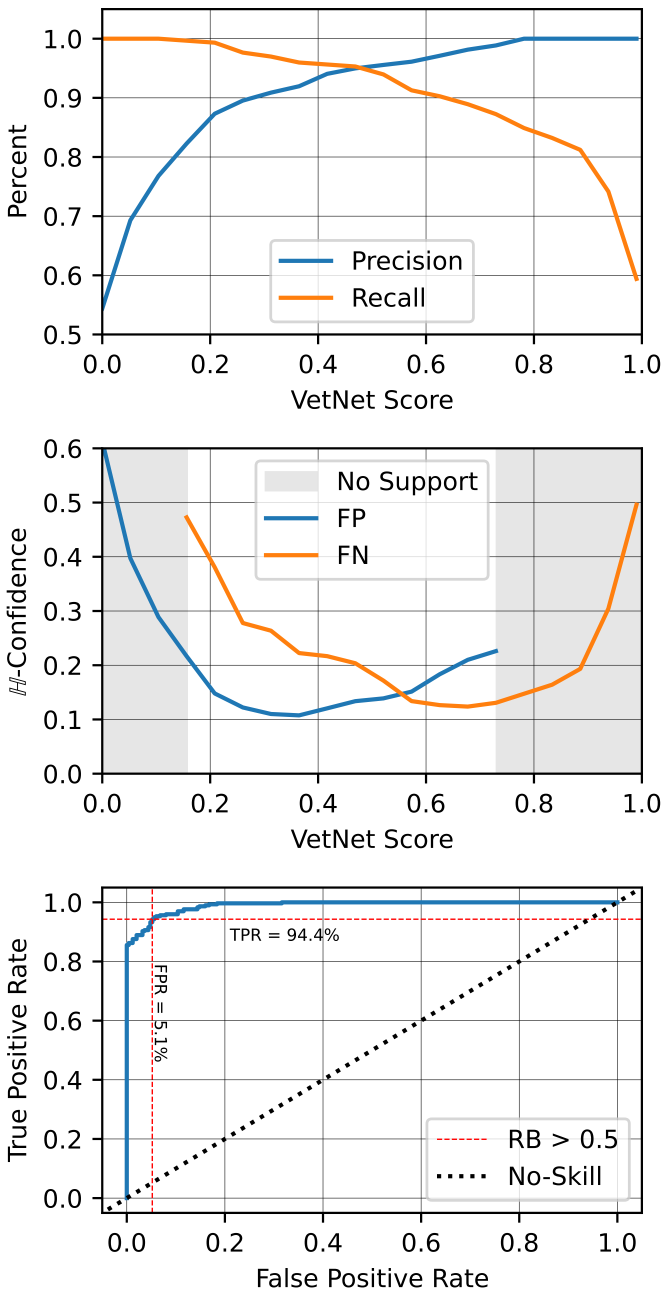

Figure 3.7 Performance of VetNet on the on-sky test set. (**top**) Precision and recall as a function of the VetNet real-bogus score. At the $RB = 0.5$ threshold, the observed precision and recall are 95.4% and 94.4% respectively. (**middle**) Entropy-based confidence scores for false-positives and false-negatives as a function of VetNet real-bogus score threshold. Shaded regions indicate score regions where no false positives or false negatives occur within the on-sky test set. (**bottom**) ROC curve for VetNet. The area under the ROC curve (the ROC-AUC metric) is 0.99, representing the probability that a random real candidate will receive a higher real-bogus score than a random bogus candidate. No-skill line indicates the expected performance curve for a random classifier.

CHAPTER 4: ORBITAL FOREGROUNDS FOR ULTRA-SHORT DURATION TRANSIENTS[1]

The event rate and sky distribution of glints has not received systematic study, and the potential for these events to contaminate searches for ultra-short transients remains. In this Chapter, I use single-image detections from the Evryscope Fast Transient Engine (Section 4.1) to measure the on-sky event rates of satellite glints for the first time. I provide estimates of the flash rate as a function of observed magnitude and sky position (Section 4.2). I discuss the impact of this population on both current and upcoming observatory facilities, and its implications for searches for ultra-short and multi-messenger transients, including the hypothesized optical counterparts to Fast Radio Bursts (FRBs), in Section 4.3.

Section 4.1: Observations and Survey

For this survey, we consider the earliest Evryscope data analyzed by EFTE in real-time, including images collected between 2019 November 24 and 2020 April 16, and we have made no cuts for weather. Images within 10 degrees of the moon are excluded by the data quality monitor. The Evryscope system design and survey strategy are described in Ratzloff et al. (2019a), Law et al. (2015), and in Section 1.2 of this work. EFTE is described and characterized in Chapter 2 and Chapter 3.

---

[1] This chapter adapted from the following paper, published in *The Astrophysical Journal Letters*. ©The American Astronomical Society. Reproduced by permission of IOP Publishing. All rights reserved. The full bibliographic entry for the published article is as follows:
Corbett, H., Law, N. M., Soto, A. V., et al. 2020, Astrophysical Journal Letters, 903, L27, "10.3847/2041-8213/abbee5"

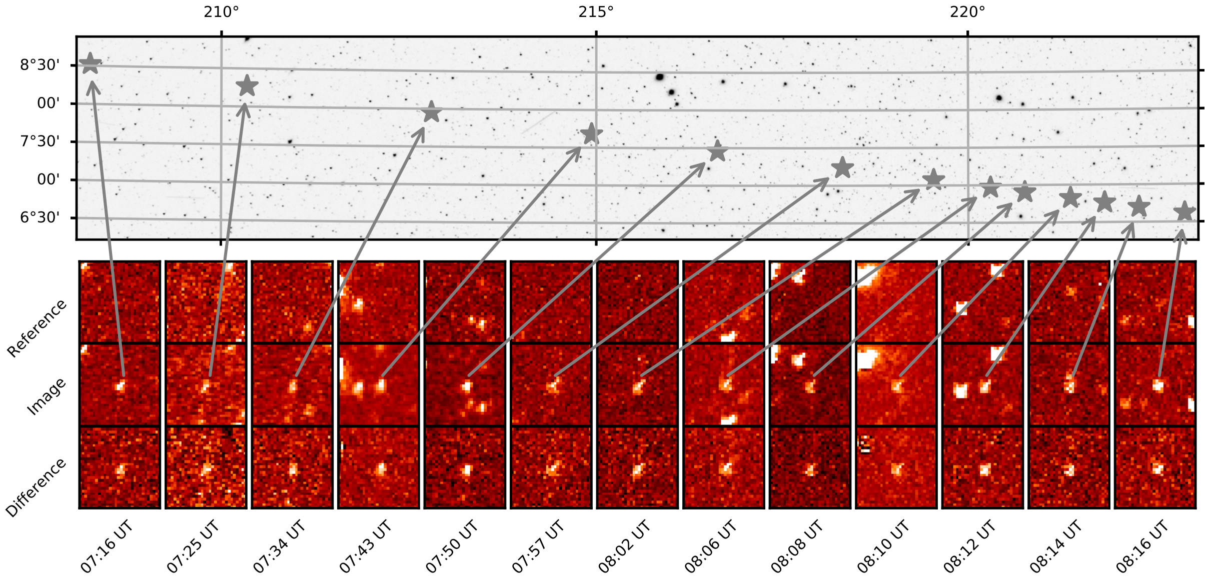

Figure 4.1 **(top)** Example of a typical flash-producing trajectory seen by EFTE, followed over a single Evryscope pointing. **(bottom)** Postage stamp cutouts of the reference, science, and discovery images, demonstrating point-like morphology. Each cutout is 30×30 pixels (6.6×6.6 arcminutes) in size.

4.1.1 Single-Epoch Flash Sample

We observed 3,372,044 high-probability candidates that passed our vetting criteria as described in Section 4.1.2. Of these, we identify 1,415,722 candidates that do not appear in multiple epochs as likely satellite flashes. This cut removes variable stars and persistent artifacts from bright stars.

Single-epoch candidates tend to occur in tracks across the sky on timescales ranging from sub-cadence to hours. Figure 4.1 shows a typical track observed by Evryscope, followed for 1 hour, along with typical 30×30 pixel (6.6×6.6 arcminute) subtraction stamps from the EFTE pipeline. The timescale of the delay between flashes gives an angular speed of 10" second^{-1}, or roughly one Evryscope pixel per second. However, we do not observe any streaking at any epoch, implying that the duration of each individual flash is much less than 1 second. This is consistent with the population of fast optical flashes noted in Biryukov et al. (2015) and Karpov et al. (2016), but observed in images integrated over minutes.

4.1.2 Transient Detection with the Evryscopes

EFTE uses a simplified image-subtraction technique for candidate detection.[2] Evryscope focus and optics, and thus PSFs, are stable on month-to-year timescales (Ratzloff et al. 2020a), and atmospheric seeing is dominated by optical effects under all observing conditions in each Evryscope's 13.2" pixels. This stability means that image subtraction within a single pointing does not require the PSF-matching techniques addressed by standard routines, such as HOTPANTS (Becker 2015) or ZOGY (Zackay et al. 2016). Similarly, because we are targeting the fastest-timescale events, we do not require widely-spaced reference frames; instead, an earlier image from the same pointing is subtracted from each image, typically with a ten-minute separation.

For each single-camera science image $S(x, y)$ and reference image $R(x, y)$, we calculate a discovery image $D(x, y)$ from the per-pixel change in signal-to-noise ratio. Both $S(x, y)$ and $R(x, y)$ are calibrated, background-subtracted, and aligned images in electron units. We measured image background levels using an interpolated and clipped mesh, as implemented in SEXTRACTOR (Bertin & Arnouts 1996). The discovery image $D(x, y)$ is given by:

$$D(x, y) = \frac{S(x, y)}{s_S(x, y)} - \frac{R(x, y)}{s_R(x, y)}, \tag{4.1}$$

where $s_R(x, y)$ and $s_S(x, y)$ are noise images calculated for each image $I(x, y)$ with measured background noise $s_B^2(x, y)$ as

$$s_I(x, y) = \sqrt{I(x, y) + s_B^2(x, y)}. \tag{4.2}$$

While this technique is not statistically optimal, it is efficient (98.5% of images are reduced in cadence) and produces stable artifacts that can be rejected via automated means. We identified all sources where $D(x, y) \geq 3$ in at least three contiguous pixels for automated

---

[2] This formulation of the direct subtraction algorithm is distinct from the current version, described in Chapter 2. The two versions differ by a normalization term.

vetting. We perform aperture photometry for all candidates using the science image, and calibrated the results to the ATLAS All-Sky Stellar Reference Catalog (Tonry et al. 2018).

A typical single image subtraction using this method produces $O(10^3)$ candidates. We require the ratio of negative-to-positive pixels within a 5-pixel diameter to be less than 0.3 to remove dipole artifacts from misalignments and Poisson noise peaks near bright stars, which reduces the number of candidates to $O(10^2)$. These are then processed with a convolutional neural network (LeCun & Bengio 1995) trained on small cutouts from $S(x, y)$, $D(x, y)$, and $R(x, y)$ in both real and simulated data, reducing the final number of candidates to 6^{+13}_{-5} per image when averaged over all weather conditions and cameras.

4.1.3 Survey Completeness

We characterized the completeness of the EFTE survey with injection-recovery testing. The image sample contained 500 pairs with the same ten-minute separation used on-sky, and was representative of all weather and instrument conditions contained in the survey. We injected ∼1200 sources into each image ($8.0 \leq m_{g'} \leq 16.75$), using the normalized median of nearby stars as the injection PSF. We processed each image pair as described in Section 4.1.2 twice, alternating which image in the pair was used as the science frame. We define a recovery as a candidate detected within three pixels of an injection position, with the radius determined by the 99th percentile of the nearest-neighbor distance between the vetted candidates and their nearest injection position.

Figure 4.2 shows the measured completeness as a function of magnitude, along with the 90% confidence interval (CI), which includes measurement uncertainty, variability with observing conditions, and the vignetting effects. Completeness decreases at both the bright and dim ends of the distribution. Saturation causes poorly-constrained centroids leading to non-recovery at the bright end. The average 50% completeness limit of $m_{g'} = 14.2$ is brighter than the Evryscope dark-sky, single-image limit of $m_{g'} = 16$ due to a combination

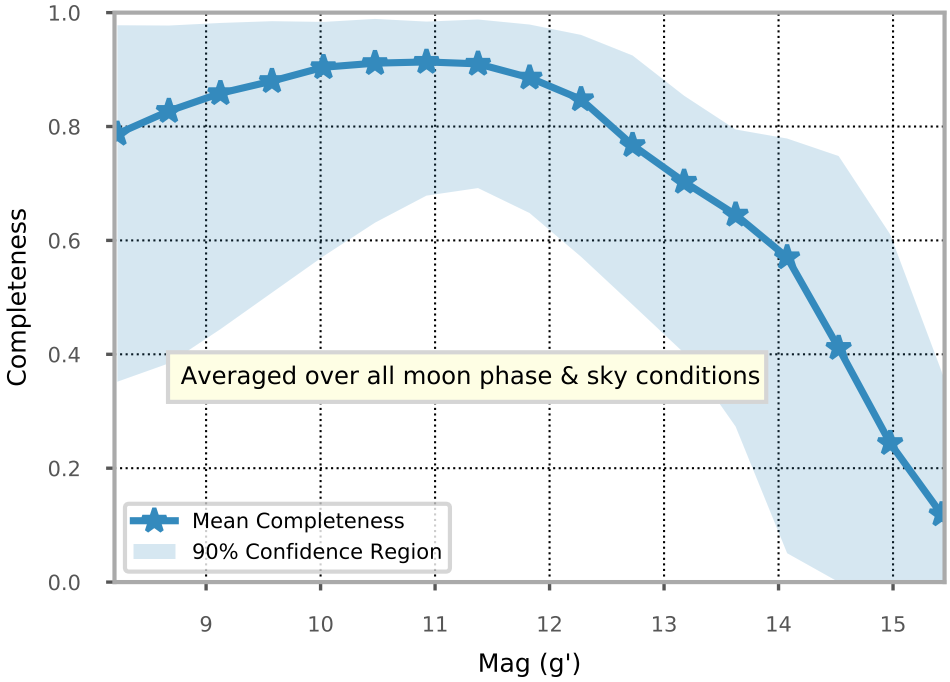

Figure 4.2 Completeness vs. magnitude for the version of EFTE used for characterizing the glint rate, averaged over all observing conditions and cameras. See Section 2.7.4 for a characterization of the completeness in the current production version of the pipeline.

of including all sky conditions in our analysis and using reference images with similar noise profiles to science images.

4.1.4 Candidate Reliability

Despite careful vetting, the median EFTE false positive rate (FPR) is ∼6,800 per hour. In EFTE surveys for rapidly-evolving transients, further vetting is performed by crossmatching with galaxy and stellar catalogs, or by association with gamma-ray and gravitational-wave transient skymaps, combined with direct human interaction. Measuring an all-sky event rate, however, requires knowing the fraction of real events in the sample. To measure this fraction, we visually inspected 27,817 randomly selected single-epoch candidates that passed our automated vetting as described in Section 4.1.2.

Each candidate was assigned a binary classification, where a "real" classification corresponds to a candidate that is morphologically consistent with an astrophysical transient. Of the candidates classified, 2,823 were classified as real. From this, we estimate the real flash fraction (RFF) in the vetted EFTE event stream to be 0.10 ± 0.03. Least-squares fits the to RFF as a function of magnitude and solar elongation produced slopes not different from zero, with and uncertainty set by the standard deviation of the residuals around the fit. Bogus candidates included:

1. Subtraction artifacts from bright stars (50%).
2. Optical ghosts, distinguished based on non-PSF-like shapes and presence in the reference frame (1%).
3. Aircraft strobes, distinguished based on nearby parallel streaks (3%).
4. Particle strikes (46%).

The final category includes both readily-identifiable cosmic-ray muon tracks and signals caused by Compton recoil electrons from environmental radioisotopes, which can be PSF-like. To constrain this population, we reduced a series of 120-second darks with EFTE and searched for candidates meeting our vetting criteria. We place an upper limit on the base rate of PSF-like particle strikes of ≤ 0.1 per image, or ~ 300 sky^{-1} hour^{-1}, which is small compared to the all-sky orbital flash rate (Section 4.2.2).

Evryscope PSFs, and the resulting degree to which stellar sources are undersampled, are variable across each individual camera's FOV. At the center of the field, dim sources can have a FWHM $\ll 1$ pixel. To avoid distortion of these sources, we estimate the prevalence of particle strikes in our candidate sample using the RFF, rather than directly removing them from the images with standard cosmic-ray mitigation tools, such as LA-Cosmic (van Dokkum 2001).

Section 4.2: Event Rates of Flash Events

We calculated event rates for candidates within discrete bins in observed magnitude in a two-minute integration. Raw event rates for each magnitude bin $r(m_o)$ are given by:

$$r(m_o) = \frac{F_m}{c_i f_i N_i}, \tag{4.3}$$

where F_m and N_i are the number of candidates observed within the magnitude bin and the number of images in the survey respectively, c_i is the coverage per image, and f_i is the fill fraction of each image (*i.e.*, the fraction of a single-single camera FOV that contributes to the overlap-deduplicated Evryscope FOV). Per-image coverage is constant at $c_i = 12.348$ deg^2 hours. The fill fraction is determined by camera arrangement ($f_i = 0.965$).

4.2.1 Monte Carlo Rate Correction

We used a Monte Carlo approach to model the effects of completeness and reliability as a function of magnitude (Section 4.1.3). We modeled the per-magnitude completeness as a bounded Johnson distribution (Johnson 1949) using maximum likelihood estimates for the mean, standard deviation, skewness, and kurtosis from injection testing. We corrected for the reliability of the event sample using the RFF described in Section 4.1.4, modeled per magnitude bin as a normal distribution.

For each magnitude bin, we made 100,000 draws from the fitted completeness and reliability distributions, each time calculating a corrected event rate as

$$\Gamma(m_o)_i = \frac{r_{m_o} R_i}{C_i}, \tag{4.4}$$

where C and R represent values drawn from the completeness and reliability distributions, respectively. The reported mean rate is the 50th percentile of $\Gamma(m_o)_i$. The lower and upper bounds of the 90% CI were taken to be the 5th and 95th percentile of $\Gamma(m_o)_i$.

4.2.2 Magnitude Distribution

As noted in Lyutikov & Lorimer (2016), flashes shorter than an image exposure time (typically $\gg 1$ second) will exhibit phase blurring, diluting their flux relative to the surrounding stars by the ratio of the integration time to their intrinsic duration. For sub-second durations, consistent with the example seen in Figure 4.1 and in Biryukov et al. (2015), the peak of the flash light curve will be brighter than is observed in long integrations. In general, the peak magnitude of the flash m_P is given by

$$m_P = -2.5 \log_{10}\left(\frac{T_{exp} 10^{-0.4 m_o}}{\tau_f}\right), \tag{4.5}$$

where τ_f is the equivalent width of the light curve and T_{exp} is the exposure time. We assume a flash duration of 0.4 seconds, based on the mode of the distribution presented in Karpov et al. (2016), when estimating the peak brightness from the observed magnitude.

Figure 4.3 shows the cumulative and normalized magnitude density distributions as a function of observed and estimated peak brightness. The shaded regions represent the 90% CI. For the cumulative distributions, the CI is bounded by the cumulative quadrature sum of the per-bin CI limits. We extrapolate an all-sky event rate from the observed rates in three regions: around the south celestial pole (SCP), within ten degrees of the equator, and across all declinations. Both the all-sky and equatorial distributions peak at $m_o = 13$, whereas the polar distribution peaks at $m_o = 12.2$, with a possible second peak near the saturation limit.

We measured integrated flash rates for $m_o < 14.25$ of $1.0^{+0.27}_{-0.15} \times 10^3$, $4.0^{+1.40}_{-0.60} \times 10^3$, and $1.8^{+0.60}_{-0.28} \times 10^3$ sky^{-1} hour^{-1} in the SCP, equatorial, and averaged all-sky regions respectively. Assuming that the observed population is dominated by satellite glints, we expect a higher rate near the equator because equatorial orbits are confined to a narrow declination band. The SCP region will only contain objects in polar orbits spanning the full declination range, lowering the observed rate.

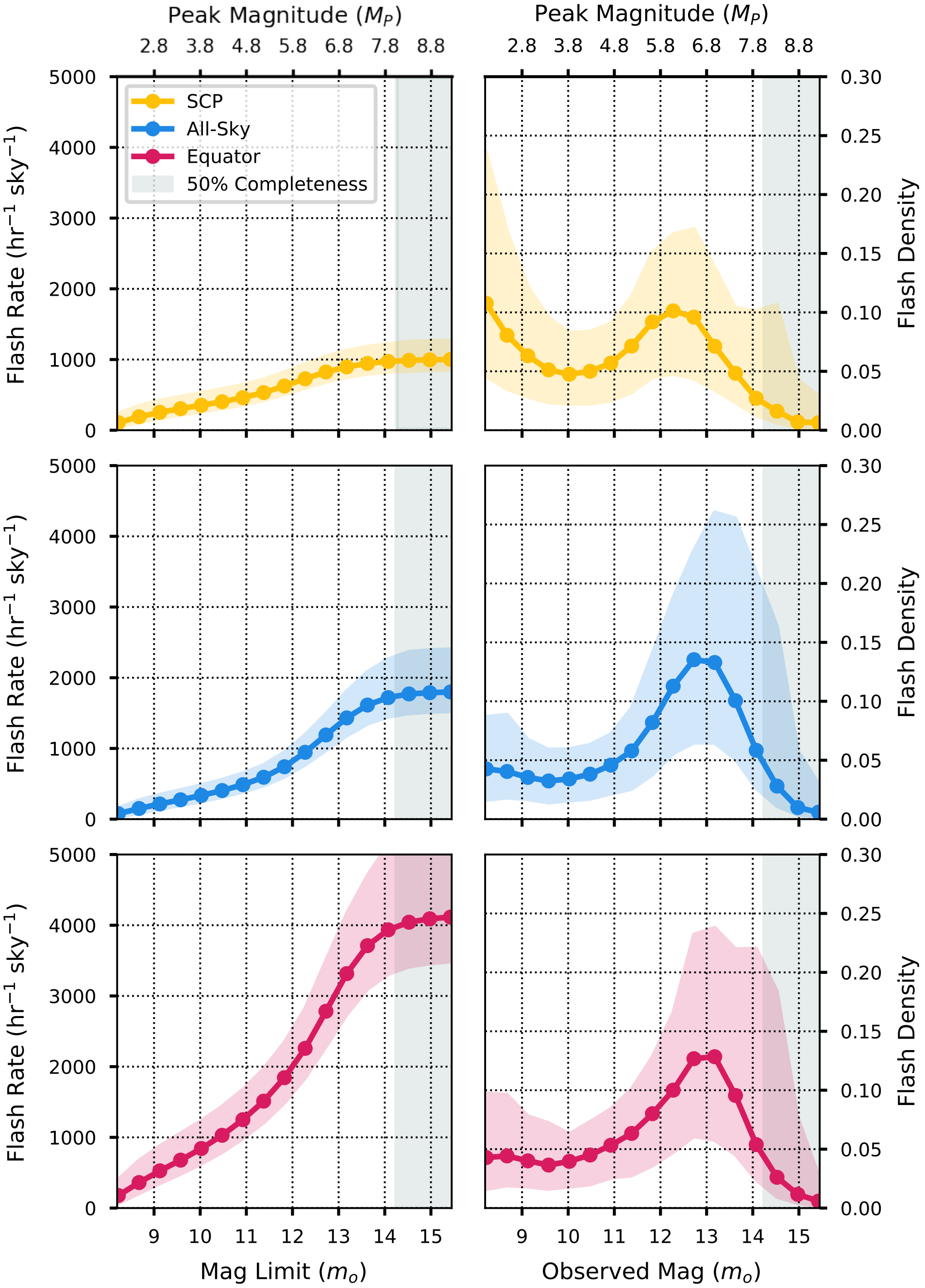

Figure 4.3 Cumulative **(left)** and normalized **(right)** flash rate distributions as a function of magnitude. We consider the event rate around the south celestial pole (SCP) **(top)**, averaged across the sky **(center)**, and around the equator **(bottom)** as a function of both observed magnitude in 120 second integrations and limiting peak magnitudes assuming a 0.4 second flash duration. Rates are corrected using the technique described in Section 4.2.1 to account for survey completeness and contamination. Shaded region gives the 90% CI on each distribution.

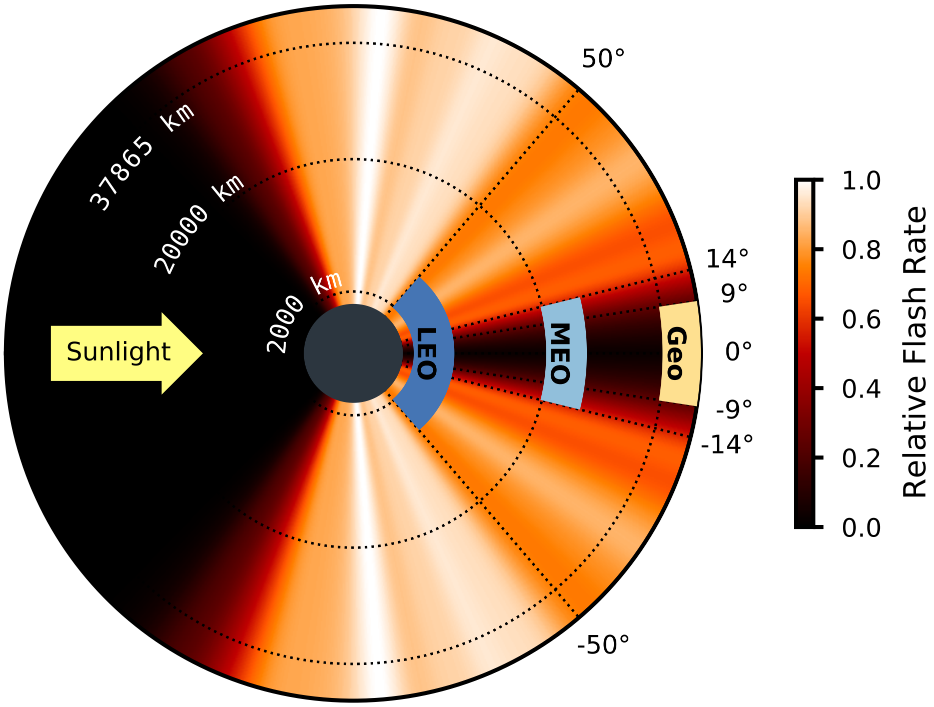

Figure 4.4 Geometry of Earth's shadow relative to the position of the solar antipode. The angular size of the shadow depends on altitude, ranging from 9 degrees for a typical geosynchronous orbit, to 50 degrees at the upper limit of low-Earth orbit. The color gradient represents a kernel density estimation for the relative flash rate as a function of antipode distance based on the visually-sorted sample from Section 4.1.4, and is reflected across the Sun-Earth axis.

4.2.3 Solar Geometry Dependence

If the observed flashes are caused by reflections from satellites, none should be expected from the region of the sky covered by Earth's shadow. The solid angle subtended by the shadow depends on satellite altitude, following the geometry illustrated in Figure 4.4. For low-Earth orbit (LEO) altitudes ($< 2,000$ km), the shadow covers a 50 degree radius around the solar antipode. The angular size shrinks to a 14 degree radius for medium-Earth orbit (MEO), or a 9 degree radius for geosynchronous orbit. We evaluated the distance between each of the human-vetted candidates from Section 4.1.4 and the solar antipode. Shaded regions depict the angular extent of Earth's shadow for LEO, MEO, and geosynchronous satellites.

The prevalence of flashes decreases steadily with proximity to the shadow in the region covered for LEO objects, before falling in the solid angle covered for MEO and higher orbits. Approximately 34% of the flashes occurred within 50 degrees of the center of the shadow. Few flashes occur within the region within Earth's shadow for MEO and geosynchronous orbits, with 3.5% within 14 degrees of the antipode and only 1.1% within 9 degrees, which suggests that the majority of the flashes are generated by satellites in middle- and high-Earth orbit. No Evryscope observations occur within ∼80 degrees of the sun.

Section 4.3: Implications for Fast Transient Searches

Earth satellites produce thousands of potential false alarms mimicking fast transients. One option to mitigate this fog is to duplicate monitoring across a substantial (∼ 3 kilometer for Evryscope-scale resolution) baseline, enabling parallax-based coincidence rejection. However, this requires construction of multiple facilities. An alternative approach is to track glint-producing objects directly in the event stream, using calculated orbit fits to reject candidates that occur in tracks. This approach is currently in development for the EFTE event stream (Vasquez Soto et al. 2023, in prep).

Degradation of the night sky by “megaconstellations" of LEO satellites is anticipated to be a major environmental challenge for astronomy in the coming decade (McDowell 2020). The construction of these constellations will increase the number of artificial satellites in orbit by a factor of many, with a corresponding increase in the amount of reflected sunlight visible in astronomical images. However, due to their high angular speeds and controlled rotation, reflected light from satellites similar to Starlink is unlikely to produce PSF-like glints during normal operations.

4.3.1 Visual Observers

The all-sky magnitude distribution in Figure 4.3 shows that the instantaneous peak brightness of many flashes should be detectable to the unassisted human eye. For a typical suburban sky with limiting magnitude $V \approx 4$, we predict a naked-eye-visible event rate of 340^{+150}_{-85} sky^{-1} hour^{-1} based on the all-sky averaged cumulative event rate of $1.8^{+0.60}_{-0.28} \times 10^3$ sky^{-1} hour^{-1} ($m_o < 14.25$). At the darkest sky sites, with limiting magnitude $V \approx 6$, this rate increases to 740^{+200}_{-140} sky^{-1} hour^{-1}. Within the equatorial region, the expected naked-eye event rate increases to 840^{+390}_{-220} sky^{-1} hour^{-1} ($V \approx 4$), or 1800^{+500}_{-350} sky^{-1} hour^{-1} ($V \approx 6$), based on the cumulative equatorial event rate of $4.0^{+1.40}_{-0.60} \times 10^3$ sky^{-1} hour^{-1}.

The time resolution (Cornsweet 2014) and biochemical adaptation time (Dunn & Rieke 2006; Yeh et al. 1996) of the human eye are comparable to orbital flash durations. We expect the naked-eye detectability of these flashes to vary strongly with observer ability.

4.3.2 Narrow-Field Imaging

The impact of orbital flashes on narrow-field imagers is negligible. For a 10×10 arcminute FOV, we predict approximately 1.2 flashes per 1,000 hours of exposure time based on the all-sky averaged event rate, or 2.7 flashes per 1,000 hours of exposure time based on the equatorial region event rate. While these are relatively rare events, they could account for occasional flashes that have been remarked on by amateur astronomers and some rejected single-image detections in tiling sky surveys.

4.3.3 Multi-Messenger Coincidence Searches

The flash rate measured here also implies a high coincidence rate for multi-messenger events. The Canadian Hydrogen Intensity Mapping Experiment (CHIME) is able to localize FRBs to the nearest arcminute (The CHIME/FRB Collaboration et al. 2018), reducing the expected flash count within the error radius to a likely-acceptable 3.8×10^{-5} hour^{-1} based on the all-sky averaged event rate. Wide-angle surveys like Evryscope can be expected to have a false alarm rate (FAR) of 1 per 3 years for apparent FRB optical counterparts due to orbital flashes. For FRBs localized to the equatorial region, the expected event rate and FAR increase to 8.5×10^{-5} hour^{-1} and 1 per 1.3 years, respectively.

In contrast, gamma-ray bursts (GRBs) from the Fermi Gamma Burst Monitor (GBM) have a median 90% localization area of 209 sq. degrees (Goldstein et al. 2020), leading to an expected flash count of 9.1 hour^{-1} based on the all-sky averaged cumulative event rate. With simultaneous coverage and physical constraints on the timescale of the bright early optical component, the expected flash count drops to 0.15 minute^{-1}. For GRB localizations within the equatorial region, the rates increase to 20 hour^{-1}, or 0.33 minute^{-1}.

Events with larger localization regions or weakly-constrained early lightcurves, like gravitational wave events from LIGO/Virgo, will be more heavily impacted. For a typical 1200 sq. degree sky map, the expected flash is 53 hour^{-1} assuming the all-sky averaged event rate, or 120 hour^{-1} within the equatorial region. The resulting FAR will increase linearly with both localization area and trigger rate.

4.3.4 Vera C. Rubin Observatory

We predict that point-like flashes will occur in images from Vera C. Rubin Observatory at a rate of 6.4×10^{-4} flashes per image (15 seconds of 3.5 sq. degrees), based on the all-sky averaged event rate. Assuming $O(1000)$ pointings, we expect Rubin to observe on the order of 1.3 flashes per night from this population. In the worst case scenario of all pointings being confined to the equatorial region, this rate increases to 1.4^{-3} flashes per image, or 2.8 flashes per night. Due to the 15-second exposure time of Rubin, the average observed magnitude of the flash distribution will be shifted to $m_g \sim 10.7$, 100× brighter than the g-band bright limit of $m_g = 15.7$ (LSST Science Collaboration et al. 2009). Our observed magnitude distribution drops off at the faint end, but there is the potential for a second distribution to exist beyond the Evryscope depth limit, as is seen for geosynchronous debris observed by the DebrisWatch survey (Blake et al. 2020).

We estimate that a worst-case scenario 10 millisecond flash from a geosynchronous satellite will produce a 0.15” streak, likely indistinguishable in Rubin’s 0.2” pixels. Longer-duration flashes, like the 0.4 second events we have assumed here, would produce obvious 6” streaks.

However, fully constraining the expected morphology of orbital flashes in Rubin data will require modeling of their duration via orbital characteristics of the population.

CHAPTER 5: EVOLUTION OF FLARE CONTINUUM TEMPERATURES AND PROPERTIES FOR TWO STELLAR FLARES[1]

Stellar flares are impulsive and stochastic events observed when a star's magnetic field reconfigures, accelerating a beam of particles downwards into the atmosphere of the star, heating the photosphere and producing a dramatic brightening across the electromagnetic spectrum (Allred et al. 2015). Flares are rare on individual stars, with some notable exceptions (*e.g.*, AD Leonis), but are most often generated by common late-type stars, leading to frequent detections in light curves from wide-field photometric surveys (Howard & MacGregor 2022; Pietras et al. 2022; Aizawa et al. 2022).

Translating observed optical single-band light curves to the UV flux estimates necessary for gauging impacts on planetary photochemistry (Segura et al. 2010; Loyd et al. 2018; Howard et al. 2018b) and potential pre-biotic chemistry, (Ranjan et al. 2017; Rimmer et al. 2018) is an uncertain process which often involves canonical scaling relations to a fixed blackbody temperature of 9000 K (Osten & Wolk 2015). This scaling temperature is based on empirical fits to the complex spectra of flares observed from highly active stars during spectroscopic "staring" campaigns (Lacy et al. 1976; Osten et al. 2010; Hawley et al. 1995; García-Alvarez et al. 2002), and particularly on The Great Flare of AD Leo (Hawley & Pettersen 1991). However, flares have been observed to occur with a wide range of temperatures (Loyd et al. 2018; Froning et al. 2019; Howard et al. 2020), even within campaigns targeting only the most active stars, with the events in the Kowalski et al. (2013) Flare Atlas ranging from 9,000 K to 14,000 K. The hottest flares observed can exceed 40,000 K (Robinson et al. 2005) at peak, but such events are rare in staring campaigns, which are biased both towards the

---

[1] This chapter is adapted from a paper currently in preparation. Anticipated bibliographic information is as follows: Corbett, H., Galliher, N., Gonzalez, R., Glazier, A., & Law, N. M. 2023, AAS Journals, *(in prep)*

most active stars and the more common low-energy regime of the power-law flare frequency distribution (Candelaresi et al. 2014).

In Howard et al. (2020), we analyzed a sample of 42 superflares simultaneously observed in light curves from both Evryscope and the Transiting Exoplanet Survey Satellite (TESS), and found that flares in the dataset routinely exceeded 14,000 K (43%), and occasionally have peak temperatures beyond 30,000 K (5%). Propagating these temperatures into the scaling relations for UV flux predicts a 16× increase in integrated UV energy, with corresponding 10-100× increase in the atmospheric photo-dissociation rate. While the color-temperature measurements in Howard et al. (2020) are broadly consistent with the population of measured flare temperatures from active stars stars [including a recent observation of a 25,000 K flare on AD Leo (Stelzer et al. 2022)], broadband temperature measurements are unable to isolate thermal continuum emission from spectral line emission, which can represent up to 50% of the flare flux in the decay phase (Hawley et al. 2007).

In this Chapter, I present initial results from a coordinated observing campaign to perform real-time spectroscopic followup of EFTE stellar flare detections using the Goodman High-Throughput Spectrograph (GHTS; Clemens et al. 2004) on the 4.1 meter Southern Astrophysical Research (SOAR) telescope. This campaign contributes high-cadence monitoring of the continuum and line contributions to the broadband flare flux, and enables time-dependent measurements of the thermal flare continuum. In Section 5.1, we present two flares discovered during the program and describe the low-latency spectroscopic observations. In Section 5.2, I provide an overview of the Evryscope transient discovery pipeline and describe the reduction of the SOAR data. In Section 5.3, I place constraints on the quiescent properties of the stars based on their catalog photometry and ID spectroscopy with SOAR. In Section 5.4, we constrain the bolometric energy release from the flares from their light curves using template models. In Section 5.5, I discuss the observed evolution of the flare continuum emission, and summarize and conclude in Section 5.6.

Table 5.1. EFTE flare discovery coordinates, peak magnitudes, and timestamps for detection and alert generation.

Flare	Date (UT)	First Detection (UT)	Trigger Time (UT)	N_{Det}	EVR Peak Mag m_g
EVRT-2509887	2019-12-05	03:45:25	03:48:48.285	6	10.3
EVRT-3586872	2020-02-15	05:40:57	05:45:33.53	3	12.7

Section 5.1: Observations

5.1.1 Detection of the Flares with Evryscope

EFTE produces a real-time event stream of candidate events, which can then be filtered based on cross-matching with reference catalogs, number of detections, magnitude, and various per-detection quality metrics. During the EFTE-SOAR program, we monitored the event stream using a Slack[2]-based dashboard. To produce an alert to observers, events were required to meet standard EFTE quality metrics, cross-match with a known catalog source, and produce at least two detections during a ten minute time window, separated by at least 120 seconds. The minimum separation is required due to the size of overlap between adjacent Evryscope cameras (312 deg^2 for Evryscope-South, 271 deg^2 for Evryscope-North) and the event rate for satellite glints (Corbett et al. 2020), which can produce O(100) apparent multi-epoch detections in images from adjacent cameras that also overlap in time. On average, this resulted in 3-4 high-confidence candidate flares per night, one or two of which were selected per night for spectroscopic followup. Table 5.1 lists the positions, detection times, peak magnitudes, and the number of EFTE detections for the two flares selected from the event stream for spectroscopic followup presented here.

---

[2] https://slack.com

5.1.1.1 EVRT-2509887

EVRT-2509887 was first detected in an Evryscope-South image taken on 5 December 2019 at 3:45:25 UT, located at RA $21^{\mathrm{h}}49^{\mathrm{m}}30^{\mathrm{s}}$ Dec. -60°57'43" with a g-band magnitude of 10.6. EVRT-2509887 was located in an overlap between two cameras in the Evryscope array, and a second detection was made 42 seconds later at 03:46:35 UT.[3] The flare was subsequently detected in five additional frames, at approximately one-minute cadence. The bottom panels of Figure 5.1 show 30×30 arcminute cutouts around each of the Evryscope detections. Normally, the second epoch would not be considered a confirmation image in this circumstance, due to the frequency at of satellite glints within the overlap region; however, this event was automatically cross-matched with a dim ($g \sim 20.754$) and red ($g - r = 2.686$) counterpart in the ATLAS reference catalog (Tonry et al. 2018) and was manually selected by an observer in real-time due to the plausible cross-match with a likely late-type dwarf and potentially extreme amplitude ($\Delta m \sim 10.15$). The quiescent counterpart is likely 2MASS J01271715-6057334. Photometry for this star across the Two Micron All-Sky Survey (Cutri et al. 2003; 2MASS), Gaia (Gaia Collaboration et al. 2016; 2018; DR2), the ATLAS All-Sky Stellar Reference Catalog (Tonry et al. 2018; ATLAS-REFCAT2), and AllWISE (Cutri et al. 2013) are presented in Table 5.2, along with estimated stellar parameters from `StarHorse2` (Anders et al. 2022), which are derived from data in Gaia Early Data Release 3 (Gaia Collaboration et al. 2021).

5.1.1.2 EVRT-3586872

EVRT-3586872 was first detected in an Evryscope-South image from 15 February 2020 at 05:40:57 UT with a g-band magnitude of 13.1. The candidate cross-matched with a red star ($g - r$=1.2) in Tonry et al. (2018) and was previously identified as an 'NSINE' variable in Heinze et al. (2018), a type exhibiting irregular but broadly sinusoidal variability, consistent with evolving spots on a rotating M-dwarf. An alert to observers including this catalog

---

[3] Cameras in the Evryscope are deliberately desynchronized in time to avoid readout bottlenecks.

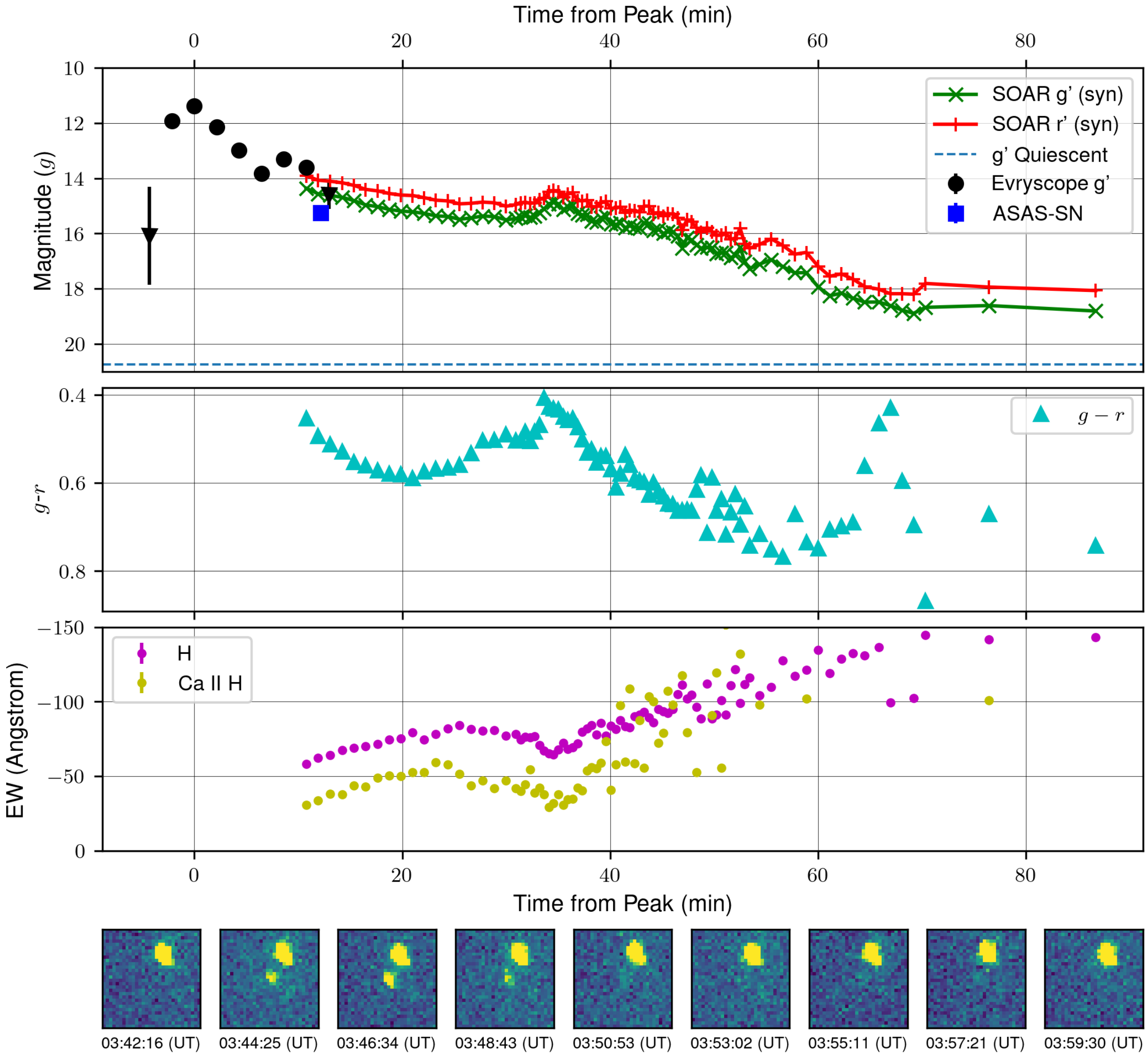

Figure 5.1 Light curves for EVRT-2509887 from Evryscope, ASAS-SN, and SOAR.

data was produced by EFTE at 5:45:33 UT, and observations with SOAR began at 5:55:48 UT. The top panel of Figure 5.2 shows the initial light curve from Evryscope and a *g*-band equivalent light curve extracted from the flux-calibrated SOAR spectra.

5.1.2 Time-resolved Spectroscopy

During the nights set aside for EFTE-SOAR observations, we monitored the EFTE event stream using the filters listed in Section 5.1.1. We selected the most likely flare events based

Table 5.2 Catalog photometry for 2MASS J01271715-6057334, the likely quiescent counterpart of EVRT-2509887.

Filter	Magnitude	Reference
g	20.754 ± 0.12	Tonry et al. (2018)
r	18.068 ± 0.11	-
i	16.329 ± 0.10	-
z	15.364 ± 0.10	-
J	13.381 ± 0.023	Cutri et al. (2003)
H	12.806 ± 0.026	-
K	12.423 ± 0.021	-
G	17.017231 ± 0.0012	Gaia Collaboration et al. (2022)
G_{BP}	19.436512 ± 0.0488	-
G_{RP}	15.614601 ± 0.0034	-
W_1	12.27 ± 0.023	Cutri et al. (2013)
W_2	12.056 ± 0.022	-
W_3	11.659 ± 0.192	-
2MASS ID	J01271715-6057334	
EVRT	EVRT-2509887	
RA (d:m:s)	01:27:17.10	Gaia Collaboration et al. (2022)
Dec (hr:m:s)	-60:57:33.55	-
T_{eff}	2,663.35 K	(Anders et al. 2019)
$\log g$	5.084859 cm/s^s	–
Mass	0.120301 M$_{sun}$	–
Metalicity	-0.004696	–
Distance	47.027 pc	–

on the requirements described above, with a preference for sources that cross-matched with a red ($g - r \geq 1.0$) source from the ATLAS All-Sky Stellar Reference Catalog (Tonry et al. 2018). For selected candidates, we would rapidly relay the coordinates of the transient to SOAR operators, manually align using the Goodman Acquisition Camera (GACAM), and begin observing with the GHTS. Table 5.4 lists the spectra collected with SOAR.

Both EVRT-2509887 and EVRT-3586872 were observed using the 400 ln/mm grating in the M1 configuration, providing spectral coverage between 300 nm and 400 nm. We selected the 1.0 arcsec slit for EVRT-2509887 and the 1.2 arcsec slit for EVRT-3586872, producing slit widths of 6.7Å and 8Å respectively along the spectral axis. The slit was oriented at the parallactic angle for all observations. Spectral resolution was seeing limited at ≤6.7Å throughout. The choice of the Goodman blue camera or red camera was decided by

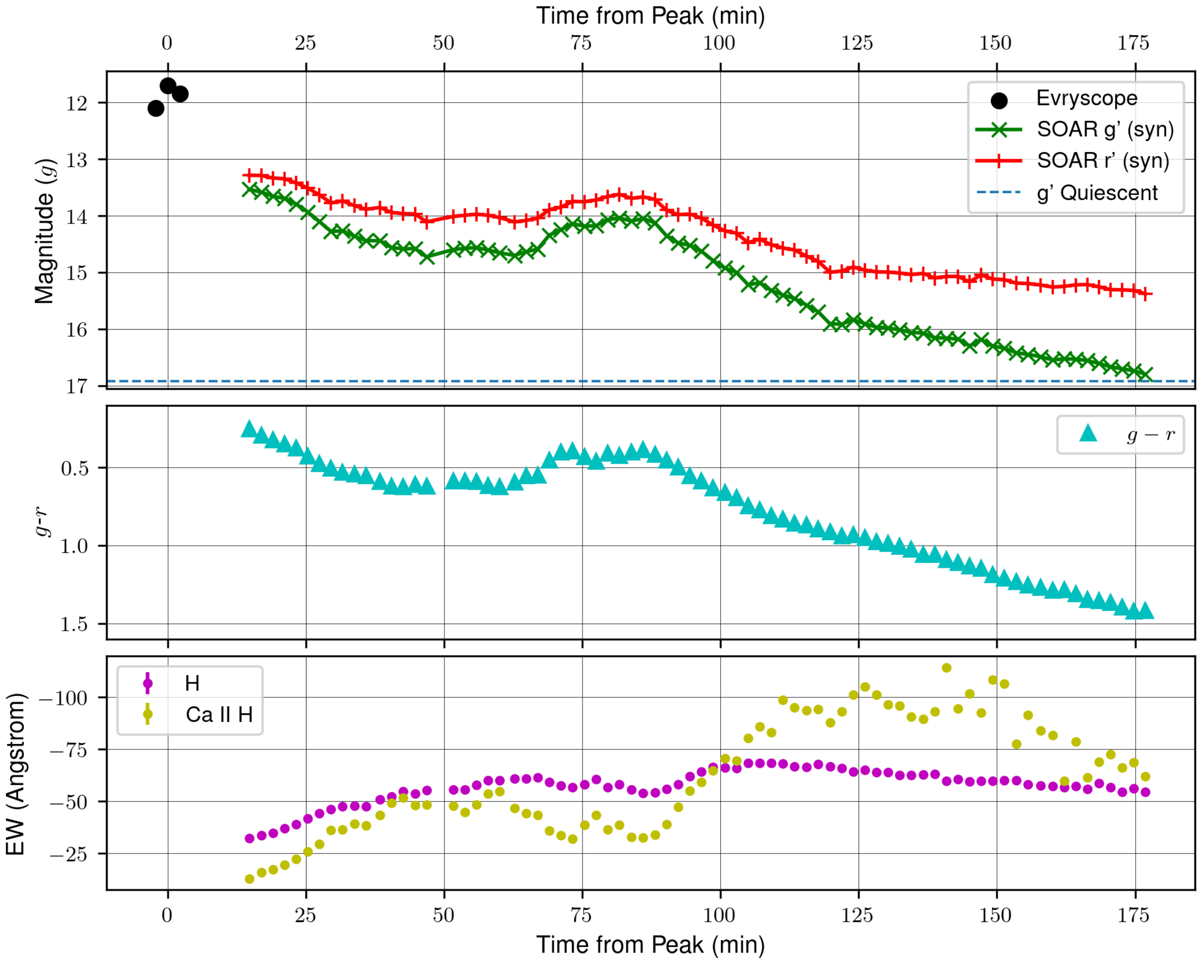

Figure 5.2 Light curves for EVRT-3506872 from Evryscope and SOAR.

other ongoing science programs with which EFTE-SOAR nights were shared. Observations with the blue camera were made with a reduced spectral ROI with 1×2 spatial-axis binning and the 200 KHz, ATTN2 readout mode, which produces a read noise of 4.74 electrons RMS and readout times of ~ 7.2 seconds. Red camera observations used a reduced spectral ROI with 2×2 in the 344 KHz ATTN 0 readout mode, which produces a 7.05 electron read noise and a readout time of 6.1 seconds.

The median latency between the EFTE trigger and the first spectra in the SOAR time series across the EFTE-SOAR program is 10m40s; however, latency is decided by a combination of human vetting time and relative position of the flare to the current SOAR

Table 5.3 Catalog photometry and physical parameters for stellar flare EVRT-3586872, an early flare detection from EFTE.

Filter	Magnitude	Reference
g	16.916 ± 0.01	Tonry et al. (2018)
r	15.73 ± 0.011	–
i	14.275 ± 0.009	–
z	13.649 ± 0.010	–
J	12.093 ± 0.023	Cutri et al. (2003)
H	11.528 ± 0.026	-
K	11.245 ± 0.021	-
G	14.997908 ± 0.0012	Gaia Collaboration et al. (2022)
G_{BP}	16.559830 ± 0.0488	-
G_{RP}	13.784114 ± 0.0034	-
W_1	11.114 ± 0.023	Cutri et al. (2013)
W_2	10.914 ± 0.021	-
W_3	10.727 ± 0.093	-
2MASS ID	J08593584-2340201	
EVRT	EVRT-3586872	
RA (d:m:s)	08:59:35.81	Gaia Collaboration et al. (2022)
Dec (hr:m:s)	-23:40:20.71	-
T_{eff}	3,255.66 K	(Anders et al. 2022)
$\log g$	4.902207 cm/s^s	–
Mass	0.3500 M$_{sun}$	–
Metalicity	0.001444	–
Distance	76.303 pc	–

bore sight. For EVRT-2509887, we were able to begin time series observations after 8m02s, and 10m14s for EVRT-2586872.

Exposure times for each target were chosen dynamically based on estimates of the SNR of bright emission lines in the spectrum. For EVRT-2506887, we initially selected a relatively long integration time of 60 seconds, anticipating a rapid decline in brightness. The SNR remained high (≥ 50) 30 minutes post peak, so we elected to decrease the cadence 20 seconds. We again adjusted the exposure time back to 60 seconds, and ultimately 600 seconds as the SNR faded. In contrast, EVRT-3586872 was observed at a 120-second cadence throughout.

Table 5.4. Summary of flare observations with Evryscope and SOAR.

Flare	Cadence (seconds)	N_{Spec}	dTrigger m:s	Start (UT)	End (UT)	Camera	Slit
EVRT-2509887	60.0	33	08:02	03:56:50	04:56:23	Blue	1.0 arcsec
–	20.0	50	–	04:17:20	04:39:49	–	–
–	600.0	2	–	04:57:59	05:08:17	–	–
EVRT-3586872	120.0	76	10:14	05:55:48	08:37:59	Red	1.2 arcsec

5.1.3 Identification Spectra for EVRT-2509887

Given the dim ($g = 20.75$) candidate counterpart identified for EVRT-2509887, we revisited the target on 29 December 2019 to confirm an M-dwarf origin. We again observed the target with the 400 ln/mm grating and the 1.0" slit, collecting 4× 1800 second exposures in the M1 configuration (300 nm - 705 nm) and 3× 1200 second exposures in the M2 configuration (500 nm - 905 nm).

Section 5.2: Data Reduction

5.2.1 Transient Detection with the Evryscopes

The Evryscopes are backed by a data reduction pipeline optimized for low-latency detection of rapidly rising transients. The Evryscope Fast Transient Engine (EFTE) leverages the optics-limited point spread functions (PSFs) and rapid observing cadence of the Evryscopes to simplify the difference image analysis typically used by transient surveys to identify new sources. Incoming images are simply normalized to their noise level, and subtracted from a previous normalized image from the same pointing, separated in time by an average of 10 minutes. Because the reference and science images have similar noise profiles, the 3-σ limit of EFTE is brighter than either individual image; the survey reaches $\sim 50\%$ completeness for $g > 14$, integrated over all observing conditions and moon phases (see Section 2.7.4 for a full characterization). Candidates are identified in the EFTE direct subtraction image and high-probability candidates, as determined by the automated vetting system (see Chapter 3), are passed through to human monitors via a web interface. Photometry for each candidate is done in the science image, using a forced aperture at the position of the detection in the subtraction image. The photometry is differentially corrected based on a spatially-varying zeropoint, determined from a sigma-clipped offset from g-band data in the ATLAS Refcat2 (Tonry et al. 2018).

5.2.2 Reduction of SOAR Data

All data from SOAR were reduced with a custom, Python-based reduction pipeline. Each image was bias-subtracted and overscan regions were trimmed. We used `astroscrappy` (McCully et al. 2018), an optimized Python implementation of the L.A. Cosmic algorithm (van Dokkum 2001), for cosmic ray rejection.

Directly after each time series, we collected HgAr calibration lamp spectra for wavelength calibration. While bracketed lamp spectra during the course of the observations would better account for deformation and shifting of the spectrum as a function of airmass, we elected to maximize time on target, and instead apply a linear offset to the lamp wavelength solution for each image, based on the position of the 5577Å atmospheric forbidden line of atomic oxygen. After applying this offset, the centroids of the Hβ and Hα lines are stable to ±.8 Å, which is sufficient for robust identification of spectral lines.

Due to the number of spectra collected, we use an automated extraction routine for both the target and background sky spectra. For extraction of the spectrum within each image, we bin by a factor of 10 in the spectral axis and then fit a linear extraction region and gaussian FWHM to the binned pixel. The parameters of the extraction window and profile are averaged across for each target, and interpolated across the range of the un-binned 2D data to produce a gaussian extraction window for the target. These windows are then multiplied by each 2D image and summed in the spatial dimension to produce a 1D spectrum.

To measure the background sky spectrum, we offset the gaussian extraction window by ±2.1 arcsec, ±3.0 arcsec, ±4.5 arcsec, and ±5.7 arcsec in the spatial (y) axis, and then extract a 1D spectrum using the same procedure as for the target. The sky spectra were then aligned using the peak of the 557.7 nm O_2 line, and sigma-clipped to remove residual starlight. No sources other than the target were detectable in the slit in any of the exposures.

Both sets of spectra were flux calibrated using spectrophotometric standard stars, CD-34 241 for EVRT-2509887 and EG-21 for EVRT-3586872. Observations of standard stars were observed in the same setups used for the target spectra and reduced as described above. For each standard, we retrieve a tabulated spectrum in flux units (Hamuy et al. 1992; 1994), interpolate it to the grid of the observed spectra with Goodman, and then calculate a wavelength-dependent flux ratio relating the e^- per second to the catalog units of ergs cm^{-2} $s^{-1}Å^{-1}$ $\times 10^{16}$. To avoid distorting the flux calibration based on the instrumental line profile, we mask prominent absorption lines with minima greater than 5% below the local continuum level.

Section 5.3: Quiescent Properties of the Flares

Figure 5.4 shows the two flare candidates within the color-magnitude diagrams of nearby stars from Gaia DR3 (Gaia Collaboration et al. 2022) and relative to the M/L-dwarf sample presented in Kiman et al. (2019). EVRT-3586872 is centrally located on the single-star main sequence, and, based on its position relative to the Kiman et al. (2019) population and relatively cool T_{eff} from `StarHorse2` Anders et al. (2022), likely has an M4 spectral type. The nature of the quiescent counterpart to EVRT-2509887 is less clear; the position in the lower tail of the Gaia CMD is again consistent with a single star system, and the position in the Kiman et al. (2019) plot suggests a slightly over-luminous M6. We compare this classification with the identification spectrum from Section 5.1.3, and suggest that the star is likely later on the main sequence and is perhaps an ultra-cool dwarf with spectral type M8 or M9. The identification spectrum and template spectra from Kesseli et al. (2017)

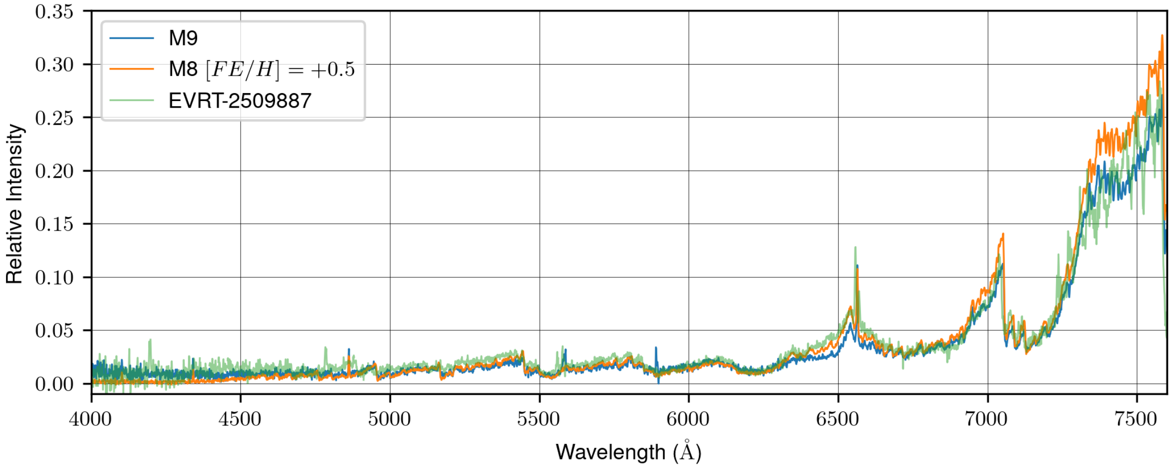

Figure 5.3 Identification spectrum for EVRT-2509887 compared to template spectra from Kesseli et al. (2017).

are shown in Figure 5.3. The overall quiescent spectrum is broadly consistent with a late-M dwarf. Based on the agreement between the observed and template spectra in the CaH and VO features (near 7000 Å and 7500 Å, respectively), we favor a later M9 spectral type.

Section 5.4: Energetics of the Flare

We extend the flare light curves beyond the Evryscope limiting magnitude using synthetic photometry derived from the flux-calibrated SOAR spectra (see Section 5.2.2). We calculate synthetic late-time flare photometry from SOAR spectra with `PyPhot` (Fouesneau 2022), using the AB-magnitude zeropoints and the g_{ps}, r_{ps} bandpasses. For a full discussion of calibration between the Evryscope and PanSTARRs photometric bandpasses, please see Section 5.1 in Corbett et al. (2023). The top panels of Figure 5.1 and Figure 5.2 show the Evryscope light curves from EFTE along side the synthetic SOAR photometry.

Flare energies, and quantities required to calculate flare energies (such as a star's quiescent luminosity [L_0]), are calculated following the procedures described in Section 2.5 of Howard et al. (2019) and the references therein, with slight modifications. Since both flare light curves contain only a few points pre-peak, we begin by fitting each light curve with a simple

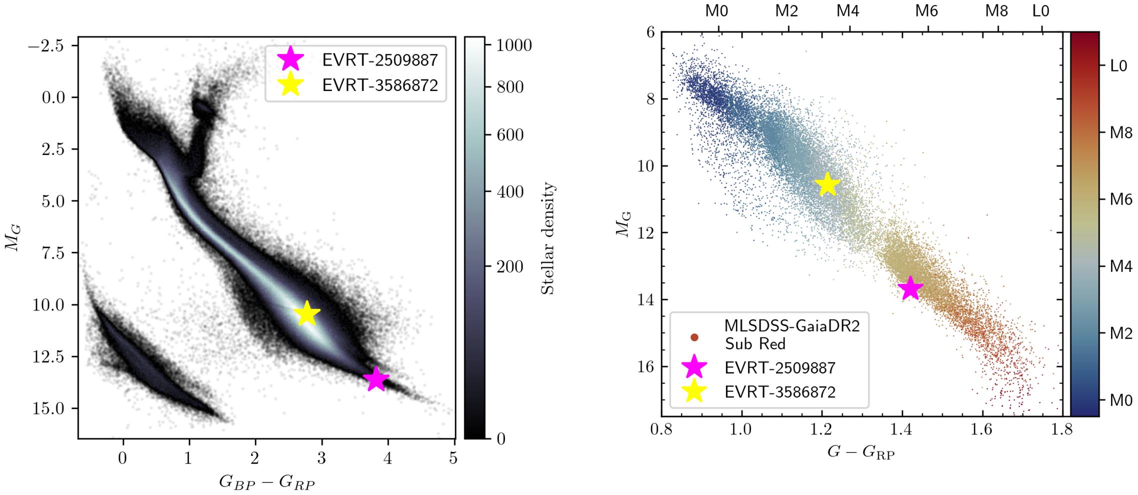

Figure 5.4 **(a)** Gaia CMD with the catalog magnitudes of EVRT-2509887 and EVRT-3586872 superimposed. **(b)** Flare stars relative to the Kiman et al. (2019) M/L-dwarf sample based on their photometry at quiescence. The positions on both diagrams are consistent with that the two stars are M-dwarfs on the single-star main sequence.

single-peaked flare model as described in Davenport et al. (2014). While the decay phases of these light curves are complex and not well described by this simple model, they capture the characteristic rising phase of the flares. For estimating the flare energy, we replace the pre-peak light curve values with modeled values, giving us a better representation of the rising-phase shape and start time of the flare. The light curve post-peak, during the complex decay phase, is unaltered for the energy estimates.

For each of these composite light curves we compute the fractional flux, $\Delta F/F = \frac{|F - F_0|}{F_0}$. Here, instead of using the median value of the light curve as the scaling factor, F_0, we convert the catalog magnitude to flux and use that as the baseline. We compute the equivalent duration (ED) as the area under the curves using the trapezoidal rule. The flare energy in the g bandpass is calculated as $ED \times L_0$ and the bolometric correction of $f_g = 0.19$ from Howard et al. (2019) is used to estimate bolometric energies. Both light curves, with associated stellar properties and known uncertainties, are used in a Monte Carlo simulation over 10,000 iterations to determine flare energies and uncertainties. We find EVRT-2509887 and EVRT-

3586872 have bolometric energies of $2.1^{+.4}_{-.3} \times 10^{34}$ erg and $1.5^{+.2}_{-.2} \times 10^{35}$ erg respectively, placing both towards the high end of the range for stellar superflares (Candelaresi et al. 2014).

Section 5.5: Flare Continua and Blackbody Temperatures

Time series spectroscopy of both targets began during the initial decay phase of the flare light curve; however, both events also exhibit a clear secondary peak in their g-band light curves accompanied by an increasingly blue color index. In this section, we describe our procedure for temperature measurement from the flare continua and present both temperature curves for the entire decay phase and measurements of the blackbody temperatures during the secondary peak. Both flares are poorly described by thermal emission alone. At the blue end of the spectrum, thermal emission is dominated by Balmer continuum. Similarly, the continuum beyond the Hβ line turns up, potentially indicating the presence of higher-order hydrogen continua or diverse multi-region thermal signatures.

5.5.1 Monte Carlo Curve Fitting

To isolate flare emission for temperature modelling, we subtracted out a quiescent spectrum from each spectrum in the SOAR flare series to produce differential spectra. For EVRT-3586872, the g- and r-band flux had returned to nearly their catalog values at the end of SOAR monitoring: $g = 16.8$ and $r = 15.4$, compared to $g = 16.916$ and $r = 15.73$ in Tonry et al. (2018), so we used the final 120-second exposure in the time series to represent the quiescent flux. The apparent color in the final spectrum ($g - r = 1.43$) is slightly redder than the 1.19 catalog value, which may suggest a slight bias in the catalog values due to frequent flaring. In contrast, EVRT-2509887 remained 1.84 magnitudes brighter than quiescent in g-band, 87 minutes after the initial peak, precluding us from using the final time series spectrum. Instead, we use the M1 configuration data described in Section 5.1.3, also used for spectral typing. Synthetic photometry measured from the EVRT-2509887 identification spectrum is offset from the quiescent g-band photometry listed in Table 5.2 by $+0.53$ mag;

it is possible that this arises from an error in the SOAR flux calibration, but could also be evidence of a previous flare biasing the catalog magnitudes.

For each of the differential spectra, we fit a physically scaled blackbody curve following Hawley et al. (2003):

$$F_\lambda(t) = X(t)\frac{R_*^2}{d^2}\pi B_\lambda(T), \tag{5.1}$$

where X is the fill-fraction of the flaring region across the stellar disk, d is the distance to the star, and B_{lambda} is the Planck function:

$$B_\lambda(T) = \frac{2h\nu^3/c^2}{e^{\frac{h\nu}{kT}} - 1}. \tag{5.2}$$

The distances to EVRT-2509887 and EVRT-3586872 are not included in the Gaia DR3 (Gaia Collaboration et al. 2022) main source list, so we instead use the estimated distances of 47.027 pc and 76.303 pc from `StarHorse` (Anders et al. 2019) and `StarHorse2` (Anders et al. 2022), respectively. Based on the radii reported for stars with similar spectral types and temperatures in Parsons et al. (2018), we estimate the radii of EVRT-2509887 and EVRT-3586872 to be 0.11 $R_\odot$ and 0.27 $R_\odot$.

We fit Eq. 5.1 to each differential spectrum using the continuum windows (BW1-BW6) selected in Table 4 of Kowalski et al. (2013), which were selected to avoid prominent spectral lines common during the flare impulsive and decay phases. The optical bandpass primarily contains the Rayleigh-Jeans tail of the thermal spectrum, making temperature measurement beyond 10^4 K from optical data inherently sensitive (Arcavi 2022). Beyond this, the measurement is complicated by the potential for flux calibration errors; to account for these errors and produce a robust estimate of the continuum temperature, we iteratively fit each spectrum using all possible combinations of 5 out of the available 6 continuum windows. For each set of windows, we fit the curve 100 times, each time replacing the flux values with random variables drawn from a normal distribution set by the differential flux and the propagated uncertainty due to read noise. We take the 50th percentile of the distribution of the best fit temperatures assign uncertainties based on the 16th and 84th percentiles of the distribution. We use a simplex minimizer for the temperature fits Nelder & Mead (1965).

5.5.2 Temperature Evolution Curves

Figure 5.5 shows the temperature evolution and g-band synthetic light curves of the two events over the SOAR time series based on the fitted blackbody radiation curves. EVRT-3576872 exhibits a steep cooling trend at the beginning of the time series, before turning up into a complex re-heating approximately 45 minutes after the flare peak, first rising to 11,500 K at +53.7 min min, then cooling by 1,000 K before peaking at $t_2 = 71.1$ minutes after the primary peak with a temperature of 13,300 K. The color index of the flare during this period of reheating (see Figure 5.2) stalls at $g - r = 0.61$. The g-band light curve shows only a modest 0.1 mag bump in amplitude, coincident in time to the initial +2,500 K rise in temperature during the second peak. The second temperature peak in this complex flare reaches 13,670 K, and is followed by a corresponding 0.56 mag amplitude peak in the light curve 10 minutes later. The tertiary flare (t_3 in panel (b) of Figure 5.5) is associated with a short (< 6 minute) and low-amplitude (0.15 mag) drop in the g-band light curve, which may be related to rapid changes in the characteristic continuum (see discussion in Section 5.8).

The temperature evolution of EVRT-2509887 is less clear, largely due to the decreased SNR at 20-second cadence near the secondary peak; however, the overall trend is comparable. A steady rise in temperature towards the secondary peak is accompanied by a small, symmetric bump in the g-band light curve, with a lag between the peak temperature and the peak of the light curve. For EVRT-2509887, the lag between the peaks is quite short at ~ 1.5 minutes. Due to the noise in the temperature measurements near the peak, this lag was measured based on the gaussian centroid of the temperature and light curve within ±10 minutes of the peak.

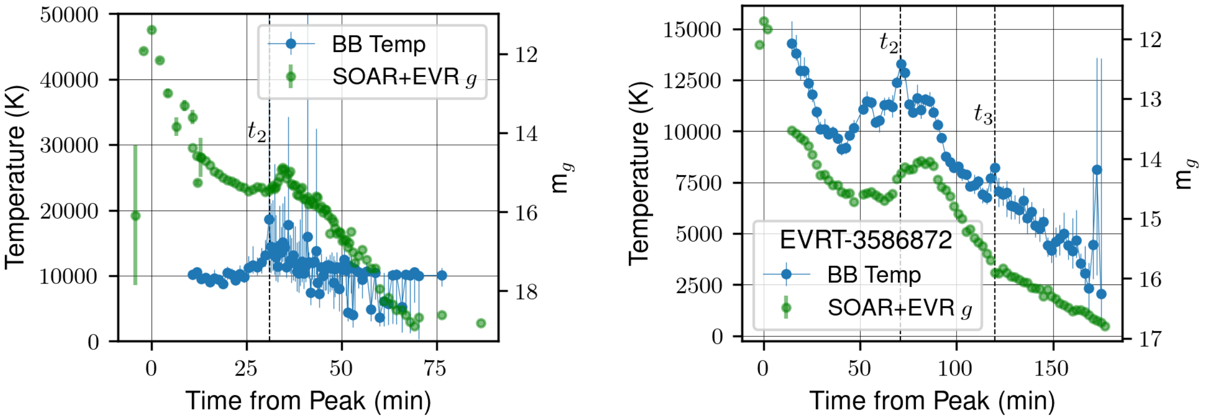

Figure 5.5 Temperature evolution of EVRT-2509887 **(a)** and EVRT-3586872 **(b)** based on a blackbody fit to continuum regions BW1-BW6 from Kowalski et al. (2013). Shaded region denotes the 90% confidence interval determined using the MC fitting routine described in Section 5.5.1.

5.5.3 Continuum Temperatures During Secondary Peak

To better constrain the temperatures near the secondary peaks, we average the differential spectra around t_2 for each flare. We resampled each differential spectrum to a shared wavelength range using cubic splines, and selected range of times to represent the peak based on the standard deviation of a Gaussian fit to temperature data. For EVRT-2509886, this produces a 19.6 minute window, centered 33.4 minutes after the peak of the flare; EVRT-3586972 evolves more slowly during the secondary peak, and the same procedure produces a 43.2 minute window, centered 69.4 minutes after the flare. Figure 5.6 shows the average spectra within these time windows, along with the best fit Planck curves over the continuum regions, using the bootstrap procedure described above. We find best-fit temperatures of 12400^{+4100}_{-2100} K and 12100^{+300}_{-200} K for EVRT-2509887 and EVRT-3586872, respectively, within the wavelength range 4000-5000 Å. Bluewards of this, the spectrum is dominated by the Balmer continuum, as predicted by Allred et al. (2006) and previously observed for EQ Peg, YZ CMi, EQ Peg A, EV Lac, AD Leo, GJ 1243, and GJ 674 (Kowalski et al. 2010; 2013; Froning et al. 2019).

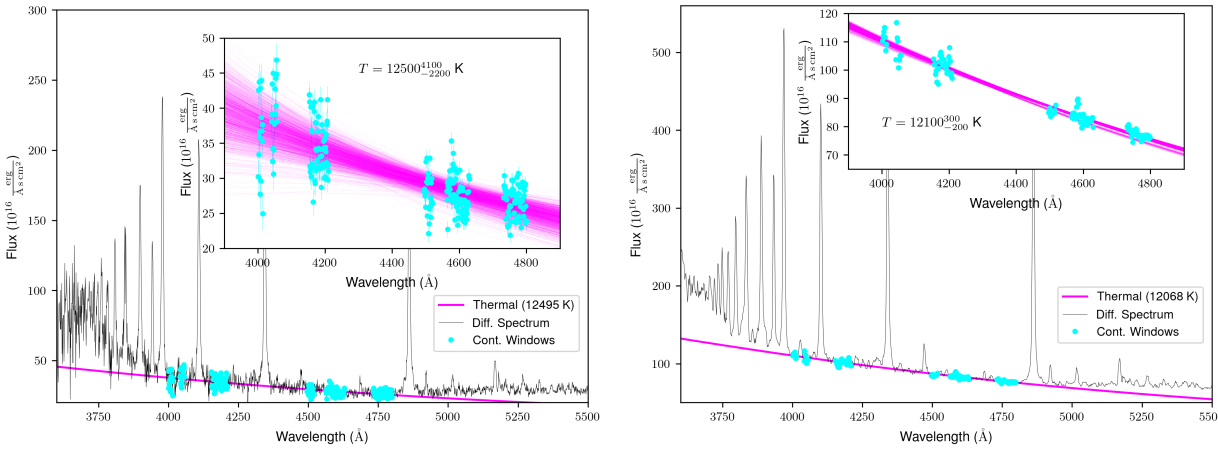

Figure 5.6 Averaged differential spectra across a Gaussian time window centered on the secondary peak of the flares. The inset panels show the distribution of blackbody fits during the bootstrap procedure described in Section 5.1. The best-fit temperatures are $12,400^{+4100}_{-2100}$ K and $12,100^{+300}_{-200}$ K for EVRT-2509887 and EVRT-3586872, respectively. The continuum emission is poorly described by a single blackbody, and both deviate from a thermal spectrum at the end of the spectrum, due to Balmer continuum emission in the blue and "Conundruum" in the red.

5.5.4 Non-Thermal Red Continuum

In addition to the Balmer continuum emission at wavelengths shorter than 3646Å, we observe continuum emission to the red of the Hβ line which deviates from the expected emission from a single isothermal blackbody source. Kowalski et al. (2013) also observed this discrepancy in some flare spectra from their active star sample (calling it "Conundruum" flux), and provide an overview of potential contributions, including emission from multiple flaring regions, iron line blanketing similar to what is seen in active galaxies (Puetter et al. 1981), calibration issues, or contributions from higher-order Balmer continua (*i.e.*, Paschen ($n = 3$) or Brackett ($n = 4$) continua). They also note that the red continuum can be present in the rising, peak, and decay phases of flare spectra. Red excess emission has also been cited as a possible explanation for observed broadband color temperatures (Osten et al. 2016). In our observations, both the blue (Balmer continuum) flux and red continuum flux track with the g-band light curve, with excess particularly visible during the secondary peak.

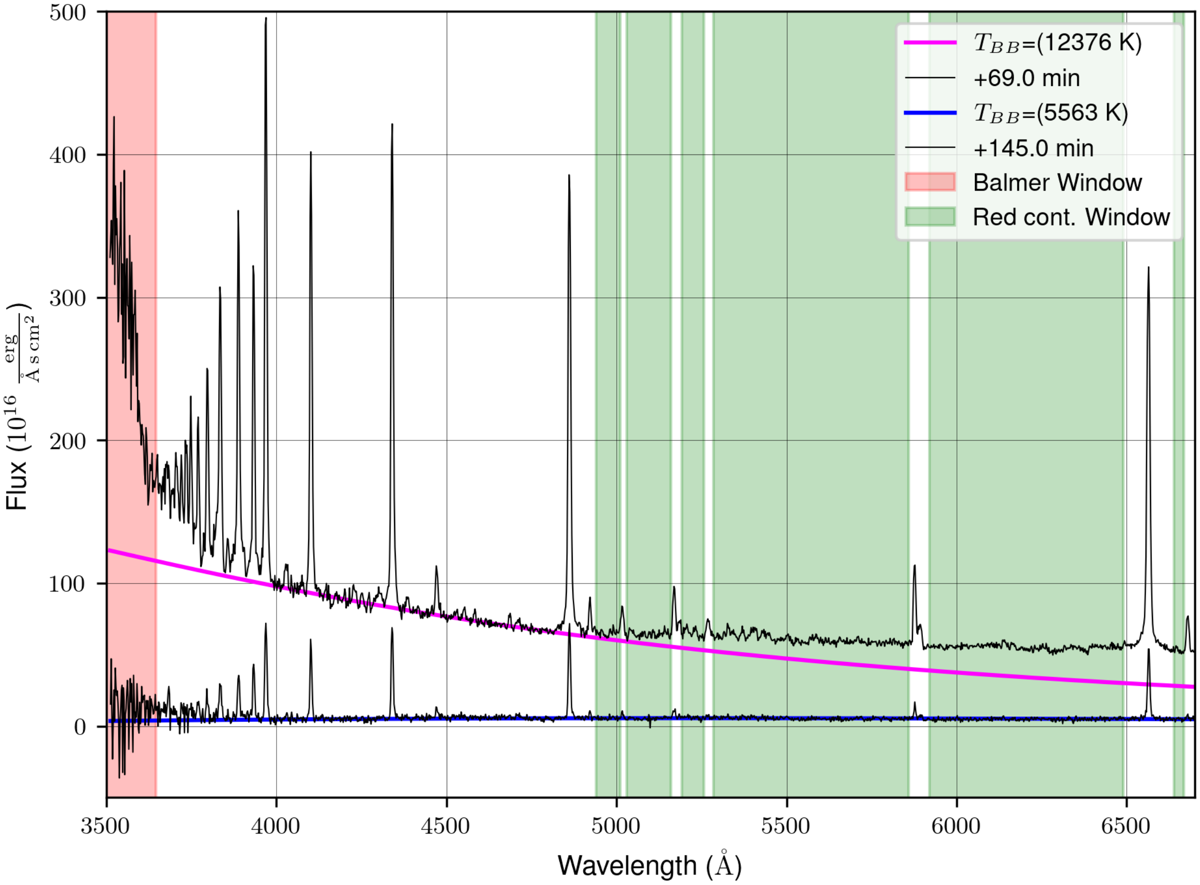

Figure 5.7 Quiescent-flux subtracted spectra for EVRT-3586872 at +69 and +145 minutes from flare peak. Near the secondary peak, Balmer continuum and "conundruum" flux, potentially higher order hydrogen series, dominate the excess emission, decaying to a mostly thermal spectrum at the end of observations. Shaded region indicates the window regions used for calculating the relative contributions of non-thermal emission.

Figure 5.7 shows differential spectra for EVRT-3586872 at secondary peak and at the end of the observations (near quiescence).

5.5.5 Relative Flux Contributions

To measure the relative flux contributions of the line emission and the balmer, red, and thermal continua, we use the fitted blackbody curves and integrate the flux in each differential spectrum within three sets of windows:

- Blueward of the Balmer jump at 3646Å

Table 5.5 Continuum windows used for measurement of the red continuum contribution to the flare energy budget.

Start (Å)	End (Å)
4940	5011
5030	5160
5192	5257
5285	5859
5920	6490
6639	6668

- Within six windows around covering the red continuum region, but avoiding spectral lines, listed in Table 5.5
- Around each spectral line, including the upturn in emission before the Balmer jump.

Figure 5.8 shows the per-epoch contributions of each of these components of the flare spectrum, relative to their ratios at the first SOAR epoch (t_0). For instance; at t_2 on EVRT-3586872, line emission makes up $\sim 30\%$ more of the total observed flux than line emission in the first spectrum. Up to their respective secondary flare peaks (t_2), all four components decay similarly in both EVRT-2509887 and EVRT-3586872, with nearly symmetric exchange between the red vs. Balmer continuum and line vs. thermal emission. Beyond t_2, the relative components of EVRT-2509887 are difficult to interpret and likely noise dominated; however, two clear transitions occur during the course of EVRT-3586872, just before each of the peaks in the temperature curve.

Approximately 20 minutes before t_2 (+54 minutes from peak), the contribution from the red continuum increases by 13% relative to t_0, roughly aligned with an 8% decrease in Balmer continuum emission and a slight increase in the g-band light curve and an upturn in the fitted temperatures. This is consistent with the color index plotted in Figure 5.2, which remains relatively flat with a slight increase following g-band. By +64 minutes, both red and Balmer emission have returned to their t_0 fractional levels, and finally invert as the temperature increases toward t_2. This leaves the Balmer continuum emission as the dominant source at secondary peak, averaging 6% larger fractionally than at t_0. Correspondingly, the red

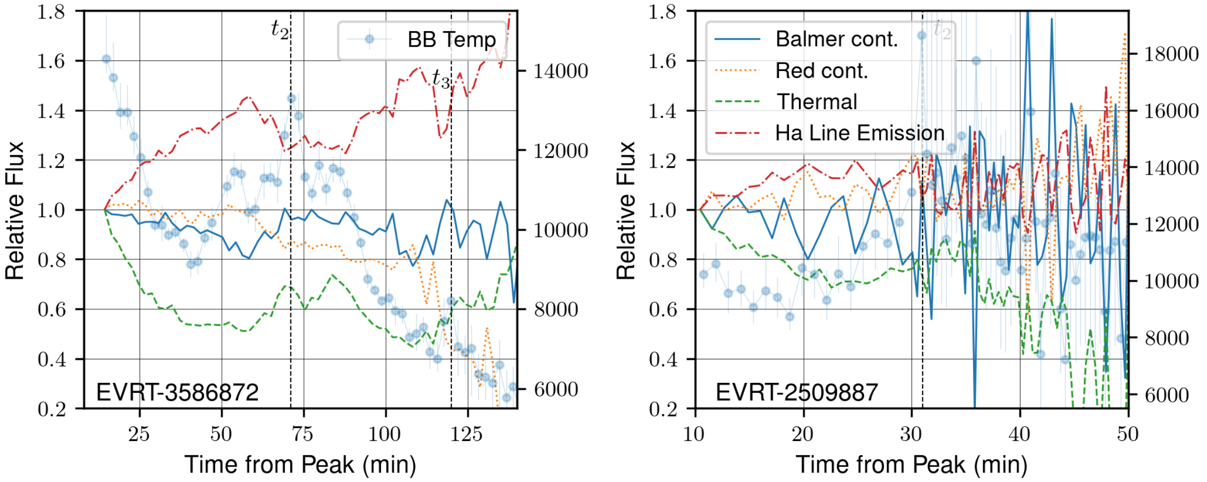

Figure 5.8 Relative flux contributions during the decay phase and secondary.

continuum decreases by 13%, with the balance going into line emission, which is dominated by the pre-Balmer jump ramp. A similar pattern plays out in the lead up to t_3; the red continuum and the balmer continuum flip at +109 minutes, and then diverge with back to its t_0 fractional contribution. In this case, the red continuum never recovers, and the differential spectra are dominated by the blackbody radiation with fading emission lines.

In both flares, the red continuum contributes up to 20% of the total optical flux, and will effect color-temperature measurements made with broadband photometry. Even if the red continuum is produced by a secondary, cooler region of the flare, considerable degeneracies exist between the relative sizes of the emission regions and their temperatures. Attempting to fit a single region will result in an artificially low temperature and corresponding UV flux, similar to the known systematics caused by line emission distorting broadband color temperatures.

Section 5.6: Summary and Conclusions

In this Chapter, we have presented time-series spectroscopy of two high-amplitude stellar flares, EVRT-3586872 ($\Delta m_g = 4.2$ mag) and EVRT-2509887 ($\Delta m_g = 10.5$ mag), detected by the Evryscope Fast Transient Engine (Corbett et al. 2023), a pipeline optimized for low-latency followup of rapidly evolving transients. The spectral time series from SOAR for each flare begins ∼10 minutes after Evryscope-detected peak and covers a wavelength range between 4000 Å and 7000Å. Based on catalog photometry for EVRT-3586872 and catalog photometry combined with an R∼300 quiescent spectrum for EVRT-2509887, we identify the host stars producing the flares to be an isolated M4 dwarf and a M9 ultra-cool dwarf.

Using a Monte Carlo fitting algorithm, we fit a blackbody temperature to the continuum of each flare, revealing an initial descent from a hot ($> 15,000$ K) peak and a complex of secondary peaks with temperatures as high as 18,000 K for the M9 flare and 13,300 K for the M4. In addition to the likely thermal emission, we observe a strong and variable Balmer continuum, as well as a poorly-understood red continuum, potentially caused by a second, cooler blackbody region or by higher-order Hydrogen continua. We find that the red continuum makes up an increasingly large fraction of the flux during the decay phase of the flare, but this trend reverses during the secondary peak. The pre-secondary peak increase in the intensity of the red continuum could support the hypothesis that this "conundruum" flux is driven by the $n = 3$ and $n = 4$ Paschen and Brackett continua.

CHAPTER 6: RAPID PROTOTYPING OF CORE TECHNOLOGIES FOR THE ARGUS OPTICAL ARRAY[1]

Section 6.1: Introduction: Overview of the Argus Optical Array

The Argus Optical Array will be a new type of deep synoptic survey instrument, leveraging the economy of scale for small optical telescopes and low-noise CMOS image sensors to image the entire sky above an airmass of ∼2 with arcsecond resolution. Relative to monolithic survey instruments, this approach has previously been demonstrated to provide competitive information grasp and survey speed per unit time and cost (Law et al. 2022c; Ofek & Ben-Ami 2020) and is an evolution of previous array telescope designs using DSLR camera lenses, including the Evryscopes (Law et al. 2015; Ratzloff et al. 2019a), SuperWASP (Pollacco et al. 2006), HATNet,Bakos et al. (2004), and MASCARA (Talens et al. 2017) To minimize maintenance requirements, arrays of telescopes (O(1000) for full-sky coverage) can be mounted on a shared tracking mount assembly and housed in a climate-controlled enclosure. This approach minimizes the number of moving parts overall, and constrains the thermal environment for the optics, promoting long-term stability.

We are currently undertaking a phased prototyping process, evaluating hardware for an eventual 900-telescope array which would provide comparable collecting area to a 5-meter monolithic mirror telescope. By using a large array of 200-mm, commercially-available telescopes, this collecting area can be spread out over an 8000 sq. degree field of view, enabling simultaneous monitoring of $O(10^7)$ stars and galaxies. The full survey description

---

[1] This chapter has been adapted from the proceedings of the Society of Photographic Instrumentation Engineers Astronomical Telescopes + Instrumentation 2022. The citation for the published article is as follows:
Corbett, H., Soto, A. V., Machia, L., et al. 2022b, in Ground-based and Airborne Telescopes IX, ed. H. K. Marshall, J. Spyromilio, & T. Usuda, Vol. 12182, International Society for Optics and Photonics (SPIE), 121824D, “10.1117/12.2629489”

and science justification for the Argus Optical Array is given in Law et al. (2022c), and an updated mechanical and optical design can be found in Law et al. (2022a). A full treatment of the general utility of multiplexed array observatories relative to monolithic systems for high-speed sky surveys can be found in Ofek & Ben-Ami (2020).

The first stage in this process, the 9-telescope Argus Array Technology Demonstrator (A2TD) based on the design concept of the Evryscopes (Ratzloff et al. 2019a; Law et al. 2015), was completed in 2021. A2TD provides a lab-local test bed for rapid prototyping of control systems, data management, and other enabling technologies for Argus Array array, including a novel automated polar alignment and single-axis tracking drive (Vasquez Soto et al. 2022), on-sky testing of climate control systems (Machia et al. 2022), and mechanical and structural support(Gonzalez et al. 2022).

The second stage of development, Argus Pathfinder, contains 38 telescopes, enabling it to survey the seasonal northern sky between declinations of -20° and 72° every night. Pathfinder operates at 30-second cadence, with a $5-\sigma$ limit of $m_A = 19.6$ in single images, where m_A is the magnitude in a wide passband ranging from 350 nm to the blue edge of the Fraunhofer A line and the O^2 telluric band at 750 nm. This depth is equivalent to $m_g = 19.1$ or $m_r = 18.3$ under dark sky conditions. Argus Pathfinder underwent an initial science deployment to the Pisgah Astronomical Research Institute in Dec 2023, an educational center and observatory in western North Carolina, and is currently in a commissioning phase.

At all stages of the prototype series, the Argus Array uses a unique observing strategy; rather than building sky coverage by observing a sequence of tiles, Argus (like the predecessor Evryscope system) tracks a large contiguous field of view in short intervals, “ratcheting” through the accessible right ascension range each night. This approach builds up sky coverage while minimizing the average airmass across the field of view. Each ratchet concludes with a slew back to the next field position, defined by the pointing of the meridian of the array. Two observing cadences will be used for Argus Pathfinder and for the full Argus Optical Array;

a standard survey with either 30- or 60-second exposures, and a secondary fast survey at 1 second cadence.

Despite the design's usage of commercial off-the-shelf optical components, building the Argus Optical Array will require development and evaluation of several enabling technologies. The primary technological readiness areas and their evaluation goals are:

1. Motion control systems: Sidereal tracking around the axis of Earth's rotation with negligible impact on the instrument PSF (i.e., less than atmospheric seeing).

2. Camera and telescope control systems: Scalability to hundreds of telescopes at up to 1-second cadence.

3. COTS 200 mm, f/2 telescopes: Usable image quality across a $>$ 45-mm diameter image circle

4. 35-mm format CMOS image sensors: Long-term stability and evaluation of noise characteristics on sky.

5. Analysis Pipeline: Scalable operations and data product generation within the observing cadence.

In this Chapter, we present the Argus Array Technology Demonstrator (A2TD), a 9-telescope test bench for rapid development and testing of the core enabling technologies of the Argus Optical Array. The system design for A2TD is illustrated in Figure 6.1. The A2TD seeks to meet the needs of the Argus Array instrument team to iterate through designs addressing the four technological readiness areas listed above within the following constraints:

1. **Timescale:** We targeted a 6-month process for on-sky operations, beginning May 2021.

2. **Modularity:** Flexibility for swapping out camera systems, operating with a partial array, and upgrading components as new designs are available.

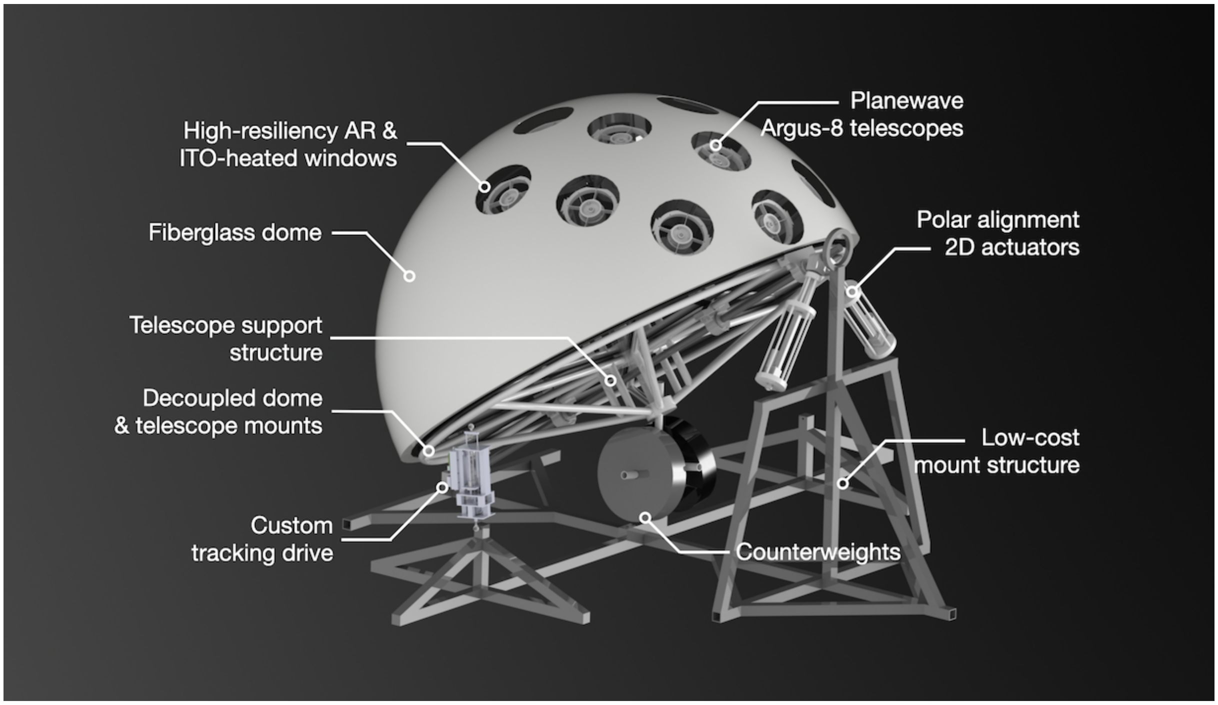

Figure 6.1 The Argus Array Technology Demonstrator concept design with its major components.

3. **Size:** The telescope array should be sufficiently large to be representative, while fitting within an 8-foot commercially-available fiberglass dome during operations and a standard box truck for transport.

4. **Budget:** Not including optical and camera hardware included in the NSF-funded Argus Array, the A2TD budget was $18,000.

We initially planned the A2TD instrument to be a rapidly deployable proof-of-concept observatory, intended for installation at a dark sky site in North Carolina; however, a project retrospective several months into system design determined that the development of the robotic observatory components necessary for a full deployment of the system would retire no additional risks given the years-long performance of such systems to support the existing Evryscope instruments built by our team. Further, our early experience with a maintenance shutdown of the EvryArgus system (see Section 5.1 in Ref. 164), and the continuing unsure nature of travel during the pandemic, incentivized us to convert the 400 kg A2TD instrument into a form that could be set up in a few hours at our local build facility in Chapel Hill, NC to perform human-supervised on-sky testing, but not necessarily undergo a full robotic deployment to a potentially unreachable remote site.

In Section 6.2, I describe the telescopes, cameras, and other optical components evaluated on the A2TD. In Section 6.3, I provide an overview of the mechanical design of the system. In Section 6.4, I outline the compute architecture used for the A2TD and the differences between the test bed model and the architecture selected for the Argus Array Pathfinder. In Section 6.5, I present a brief overview of the on-sky results from the A2TD system and its components. In Section 6.6, I summarize the instrument design and status.

Section 6.2: Optical Design

The system optics for A2TD consist of nine independent telescopes, paired with back-illuminated CMOS detectors, which observe through anti-reflective optical windows when the instrument is in a weather-safe configuration.

6.2.1 Telescopes

The initial reference design and early on-sky testing used the f/2.0, 8-inch Rowe-Ackermann Shmidt Astrograph (RASA) commercially available from Celestron[2]. These telescopes are low-cost ($2079 USD at the time of writing), and provide excellent image quality (RMS spot size $\leq 4.55\mu$m with $\leq 10\%$ vignetting) within their advertised 32-mm corrected image circle; however, this range does not fully include 35-mm format sensors, like those discussed in Section 6.2.3, which are necessary to meet our field-of-view requirements with ~1000 telescopes.[3] For a full description of the RASA optical design, see Ref. 30. An additional telescope, a custom design (the Argus-8 in Ref. 164) developed by Planewave

---

[2] https://www.celestron.com

[3] We note that an alternate design route exists, using smaller (4/3-inch) format sensors fully-illuminated by the RASA8; however, to achieve all-sky coverage with these sensors requires 3-4× as many telescopes.

Instruments[4] will be integrated into A2TD for on-sky testing leading up to the construction of the Argus Pathfinder instrument. The Argus-8 provides a 33% improvement in pixel scale, and produces a stable PSF across the full sensor plane.

6.2.2 Optical Window

Each telescope within the A2TD observes the sky through an independent optical window when the dome enclosure is in place, as shown in the reference design in Figure 6.1. Though the A2TD instrument is rarely operated in this configuration, we evaluated multiple options for exterior-facing windows, including the indium-tin oxide coatings named in Figure 6.1. However, conventionally specified optical glass is not typically suited for the demands of exterior use, which can involve hail, regular rainfall, consistent wind loading, and daily thermal cycling. Custom windows at the size and scale of the telescope apertures can cost thousands of dollars per unit, which is not scalable for to the full Argus Optical Array. We found anti-reflective architectural glass (Schott AMIRAN) to be the best match for our price and performance needs, and measured no detectable changes in the PSF FWHM above a 5% seeing-induced noise floor during on-sky testing. This includes measurements at a variety of angles of incidence out to 35 degrees from normal, relevant for the pseudo-focal Argus Optical Array design described in Law et al. (2022a), which requires only a single exterior-facing window.

6.2.3 Camera Specifications and Evaluation

The A2TD instrument supports multiple camera manufacturers and models, primarily the QHY600M from QHYCCD and both air-cooled and a custom, liquid-cooled variant of the Atik Cameras Apx60 used in the Argus Pathfinder instrument. Both cameras use the 62 megapixel, Sony IMX455 back-illuminated CMOS sensor. This sensor provides 1.7 electron readout noise, 0.004 electron per pixel per second dark current at -10 °C, and has a peak

---

[4] https://planewave.com

quantum efficiency near 450 nm of ∼92%. The sensor is available in either a -K "industrial" or a -C "consumer" variant; advertised differences include a ceramic LGA, fewer pixel defects, and a higher MTBF for the industrial variant, at significantly higher cost. Both cameras will undergo long-term evaluation within the controlled environment of the Argus Pathfinder.

Section 6.3: Mechanical Design

The details of the mechanical design of A2TD, Argus Pathfinder, and Argus Optical Array can be found elsewhere in the Proceedings (Law et al. 2022a). In this section, we will provide a general overview of the major components at the A2TD scale and their justification.

6.3.1 Hercules Mount Structure

The base of the A2TD system is the "Hercules" tube steel structure (see Figure 6.1), encompassing all stationary structural components of the instrument. The Hercules structure was designed to maximize transportability, and breaks down into six smaller components for shipping or storage. The assembled base structure, with the telescope support structure and tracking arms removed, will fit in a standard 12-foot trailer. The Hercules mount is described in full in the Gonzalez et al. (2022).

6.3.2 Telescope Support Structure

The telescope support structure is a circular aluminum spoke platform that supports the dynamic components of the instrument, and is pictured in Figure 6.2. The tubing is connected to the axle of the Hercules mount via two pillow blocks, placed at the middle of the radius along the axle. Telescope mounts, made of 3D-printed dovetails and aluminum extrusion, are bolted to a plywood top secured to the tubing. The placement of the telescopes within A2TD does not produce a contiguous field-of-view; instead, the telescopes are distributed in airmass to produce data representative of an all-sky field of view. Additionally, modifying the system to provide a continuous field of view in declination would require a much larger structure, ultimately driving costs higher and compromising our size envelope goal. An overview of field of view packing techniques for array telescopes is provided elsewhere in the Proceedings (Galliher et al. 2022a).

Figure 6.2 Telescope support platform, installed on the low-cost "Hercules" mount structure, during lab integration testing.

We fit the platform with a fiberglass dome and per-telescope viewing windows, as pictured in Figure 6.1. The dome is isolated from the platform and has an independent tracking drive to minimize image quality effects of wind buffeting. The dome is weather-sealed for robotic deployment using standard rubber gaskets around the windows, and a custom vinyl fabric skirt which runs between the edge of the dome and the bottom of the tracking platform. Because we determined that the robotic deployment of the A2TD was out of scope, the system has been operated primarily without the dome installed.

6.3.3 Tracking Drives

The tracking system for A2TD is a scaled-down variant of the tracking drive mechanism for the reference design of the full Argus Optical Array as described in Ref. 164 and the current pseudo-focus array design presented in Law et al. (2022a). The AT2D dome and telescope platform track the sky independently using identical tracking drives, placed on opposite sides of the instrument. The dome tracking drive will be repurposed as the primary tracking drive for the Argus Pathfinder.

6.3.4 Polar Alignment

Precise tracking with a single-drive right-ascension instrument mount requires repeatable, accurate (few arcminute) alignment with Earth's rotation axis. For both A2TD and Argus Pathfinder, portability and ease of deployment with minimal site preparation are design goals. Differential settling of the ground underneath the instrument can shift the polar alignment out of specification over time, and a semi-automated procedure for re-alignment, potentially with no on-site support, is essential for recovery. To achieve this degree of pointing accuracy and resilience for the $\sim$400 kg A2TD instrument, we developed automated polar alignment system using a pair of linear actuators supporting the polar end of the instrument axle. This system is described fully elsewhere in the Proceedings (Vasquez Soto et al. 2022).

Section 6.4: Control System Architecture

The underlying architecture for the A2TD control system is a modular set of asynchronous HTTP web servers, implemented using FastAPI[5], running on a cluster of 13 Raspberry Pi 4 single-board computers. Of these, nine are "ocular" nodes, responsible for control of a single optical system, including a telescope, camera, and focuser. Three of the remaining nodes export motion control APIs for dome tracking, telescope platform tracking, and polar

---

[5] https://github.com/tiangolo/fastapi

alignment. The final node is used for orchestration, communicating with each of the ocular and motion control nodes via their respective HTTP APIs. We also produced command-line clients for each of the subsystems, so that they can be manually addressed for debugging, and for subsystem testing independent of the full instrument. Figure 6.3 shows a single fully assembled ocular node, including the Raspberry Pi computer.

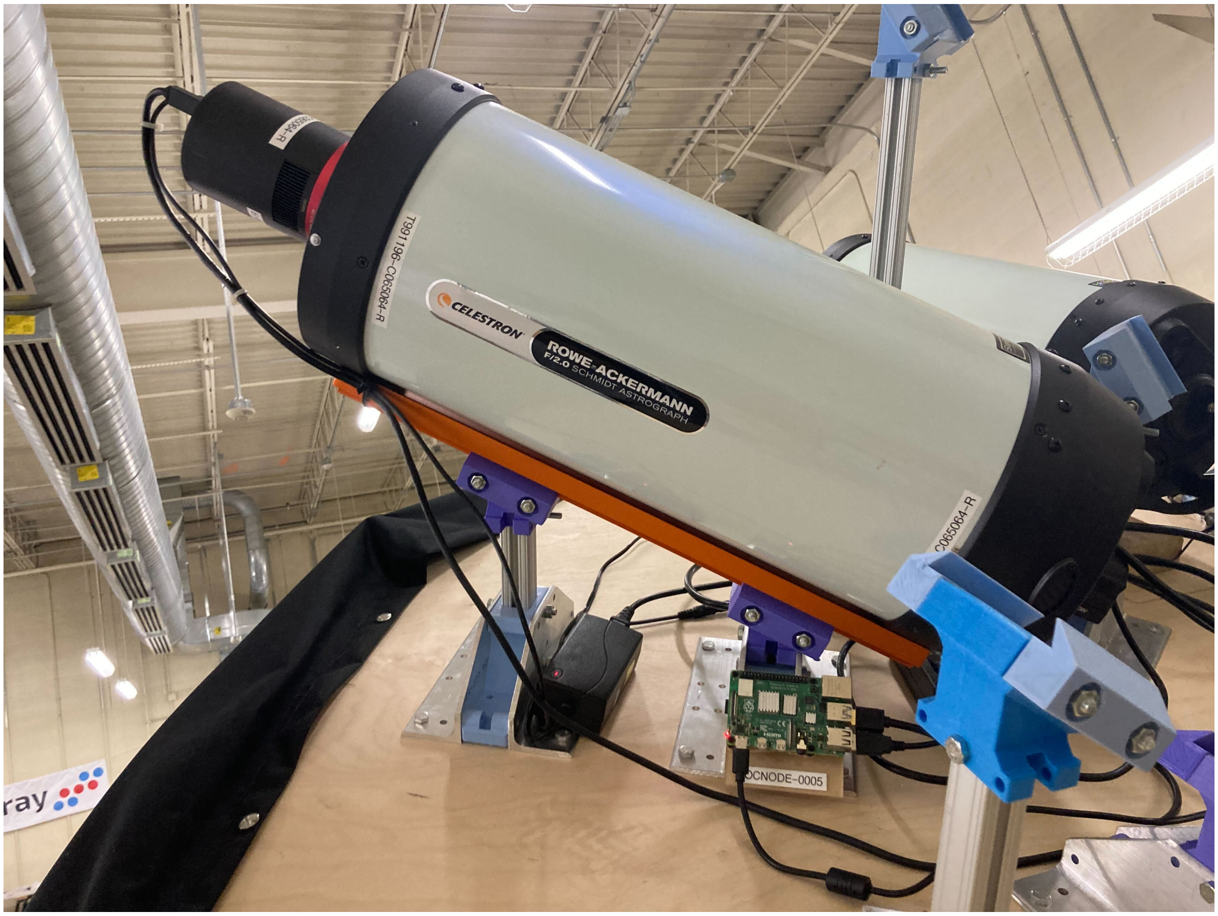

Figure 6.3 A modular telescope and camera assembly, with an attached "ocular node" control server (Raspberry Pi 4).

One notable issue with the Raspberry Pi-based architecture is scalability to the 1-second cadence observing mode. Due to the limited compute performance and the single-lane PCIe interface for the USB controllers on the single-board computers, readout times of several seconds are typical. This has motivated an alternate architecture for Argus Pathfinder and future project stages; rather than one node per camera, cameras are multiplexed into 48-

telescope units which connect to a single x86 control and analysis server via high-speed PCIe 3.0 x16 interface cards. This configuration maintains the HTTP interface at the 48-telescope sub-array level, while providing higher transfer speeds (>90% duty cycle at 1 second cadence) and GPU-based data processing with no network latency. The hierarchical control and data analysis pipeline for Argus is described in Corbett et al. (2022a).

Section 6.5: Overview of On-Sky Results

The A2TD and the standalone ocular node telescope assemblies have been used on-sky to support rapid design iteration and risk retirement. In this section, we provide a summary of the key findings and references to full results.

1. **Optical Alignment**: We developed a routine for tilt aligning camera and telescope pairs, using bench test data of a near-field focus and shims. From on-sky testing, we measure up to a 50% improvement in edge of field FWHM for the corrected Celestron RASA-8s relative to pre-correction imaging.

2. **Thermal Stability Testing**: We installed an ocular node in a custom thermal enclosure to measure variability in the optical PSF as a function of temperature and constrain the stability necessary for the Argus Pathfinder and Argus Optical Array enclosures. We measure $< 10\%$ differences in the PSF half flux diameter (HFD) for temperature fluctuations of ± 6 °C around the optimal focus. This process and the climate control design for Argus Pathfinder are described in Machia et al. (2022).

3. **Optical Window Testing**: We observed no changes in the PSF HFD above a 5% seeing-induced noise floor during on-sky testing through Schott AMIRAN architectural glass. We have also measured this glass to provide no degradation of the Strehl ratio of the PSF at up to 30-degree angle of incidence, and $< 5\%$ out to 55 degrees, beyond the operating parameters of the Argus Pathfinder window.

4. **Polar Alignment**: We have tested the automated polar alignment system described in Section 6.3.4, and achieved a sub-10-arcminute alignment with the pole, corresponding to a few-pixel drift over the course of a 15-minute ratchet and a negligible impact on PSF stability in single images. For a full description, see Vasquez Soto et al. (2022).

5. **Sidereal Tracking:** We have demonstrated tracking at the sidereal rate with sub-pixel RMS offsets over 15-minute pointings.

Section 6.6: Summary

In this Chapter, we have described the Argus Array Technology Demonstrator (A2TD), a platform for rapid, iterative development of core technologies for the Argus Optical Array, which is a new synoptic survey instrument able to observe the entire visible sky using O(1000) small telescopes arranged with a contiguous 8000 square degree field of view. The Argus Optical Array leverages newly available and cost-effective astrographic optics aimed at the amateur market, along with high-efficiency, low-noise CMOS image sensors, but has required the development of new technologies to minimize maintenance requirements for polar alignment and sidereal tracking, and for observatory operations that scale to one thousand optical systems and cameras. We addressed the needs of the development process for these new enabling technologies by building the A2TD, a modular demonstrator system for rapid iteration of motion control, optical, and software.

CHAPTER 7: THE SKY AT ONE TERABIT PER SECOND: ARCHITECTURE AND IMPLEMENTATION OF THE ARGUS ARRAY HIERARCHICAL DATA PROCESSING SYSTEM[1]

With its 54.9 GPix combined mosaic imager, the Argus Optical Array will produce 4.3 PiB of raw data per night when observing in the 1-second cadence mode, and 145 TiB per night at base cadence, numbers that are comparable to the entire data sets of the many data-rich astronomical surveys currently operating. In both operating cadences, the dead time between consecutive images is sub-millisecond, with images read out to an internal camera buffer before transfer to a control computer over USB 3.0, requiring a many-gigabit per second data transfer rate, up to a terabit (125 GiB) per second. The prototype Argus Pathfinder system, containing 38 telescopes, will produce accordingly less data, but still up to 180 TiB per night at 1-second cadence, 24% more than the full Array at 30-second cadence. Table 7.1 contains the system parameters of Argus Pathfinder and the Argus Optical Array instruments, including properties of the dataset. To reduce this data into an event stream of astrophysical transients, long-term lightcurves, and image data products requires both a physical compute architecture capable of the necessary throughput and a performant software pipeline.

In this Chapter, I introduce the Argus Hierarchical Data Production System (Argus-HDPS), the unified control and analysis pipeline for the Argus Optical Array project. In Sections 7.1 and 7.2, I describe the science and engineering requirements of the system. In

---

[1] This chapter has been adapted from the proceedings of the Society of Photographic Instrumentation Engineers Astronomical Telescopes + Instrumentation 2022. The citation for the published article is as follows:
Corbett, H., Soto, A. V., Machia, L., et al. 2022a, in Software and Cyberinfrastructure for Astronomy VII, ed. J. Ibsen & G. Chiozzi, Vol. 12189, International Society for Optics and Photonics (SPIE), 1218910, “10.1117/12.2629533”

	Argus Pathfinder	**Argus Optical Array**
Telescopes	38x 203 mm F/2.8 (1m-class equiv.)	900 x 203 mm F/2.8 (5m-class equiv.)
Detectors	61 MPix sCMOS 1.7e- RN 80 μs dead time $>$ 90% QE at 475 nm	61 MPix sCMOS 1.7e- RN 80 μs dead time $>$ 90% QE at 475 nm
Field of View	9 sq. deg per telescope 344 sq. deg instantaneous	9 sq. deg per telescope 7916 sq. deg instantaneous
Nightly Sky Coverage	19,370 sq. deg. (15 minutes per night)	19,370 sq. deg. (2-10 hours per night)
Pixel Sampling	1.38 arcsec/pix	1.38 arcsec/pix
Site	North America Pisgah Astronomical Research Institute	North America Pisgah Astronomical Research Institute
Exposure Time	1 second high-speed 30-second base-cadence	1-second high-speed 30-second base-cadence
Wavelength	Wide-band (350-750 nm)	Wide-band (350-750 nm) or alternating g', r'
Pixel Count	2.3 GPix	54.9 GPix
Mosaic Image Size	4.7 GiB	110.1 GiB
Nightly Raw Data	180 TiB (high-speed) 6 TiB (base-cadence)	4.3 PiB (high-speed) 145 TiB (base-cadence)
Throughput at 92% duty cycle	464 Gbps (high-speed) 15.5 Gbps (base-cadence)	11 Tbps (high-speed) 367 Gbps (base-cadence)

Table 7.1 Survey and dataset parameters for the Argus Pathfinder and Argus Optical Array instruments. Data types assume 16-bit pixel data.

Section 7.3, I outline the data flow and physical compute hardware underlying Argus-HDPS. In Section 7.4, I describe the algorithms and implementation status of the pipeline. Finally, in Section 7.5, I summarize and present pipeline performance results on data from A2TD.

Section 7.1: Science Requirements and Data Products

Transient alerts and images are produced at multiple effective cadences, using coaddition to perform deep searches for slow-rising transients at timescales out to 5 days. To minimize data backlog and support rapid community followup of transient events, HDPS must produce alerts and reduced images within cadence for cadences less than 1 day; i.e., 30-second images must be reduced and alerts generated within 30 seconds. As the data rate slows for longer, multi-day coadds, sub-cadence latencies can be achieved using daytime operations.

Full-frame images from the full Argus Optical Array will be prohibitively large to store, requiring up to 145 terabytes per night at 30-second cadence and 4.3 petabytes per night at 1-second cadence. To support long-term retention of image data, HDPS must reduce incoming images into pre-defined data products, including:

1. Images, segmented into 13.7×13.7 arcminute sky regions.
    (a) Full-resolution segments (HEALPixGórski et al. (2005) NSIDE=256) at base cadence, cached locally for at least 5 days
    (b) Full-resolution segments, coadded at 15-minute to 5-day cadences
    (c) Sparse full-resolution segments, containing transient detections and pre-selected science targets
    (d) Low-resolution segments with 10× reduced resolution (13.8 arcsec/pixel).
2. Transient alerts, distributed via community brokers
    (a) From single images, at both 1- and 30-second cadence
    (b) In deep coadds, up to 5 days
3. Photometric light curves
    (a) Transient sources: from image subtraction, sequentially released via alerts
    (b) Detrended long-term lightcurves for an input catalog of O(10^7) sources

Reduced image data from Argus, including deep coadds, sparse full-resolution images covering science targets, and low-resolution 13.8-arcsecond per pixel images of the entire sky, will be stored long-term and made available publicly."

The production of long-term photometric light curves, containing tens of trillions of photometric measurements across a five year survey, is a unique challenge among the Argus Optical Array data products. Removing systematics from the lightcurves inherently depends on long-term trends in time, and for this reason, we elect to produce precision lightcurves in periodic data releases, rather than within the observing cadence. Per-epoch photometry, however, will be produced in real time, using the pipelines we have developed for the Evryscopes (Ratzloff et al. 2019a). Calibrated and detrended lightcurves for pre-selected science targets will be generated and released on a schedule.

Section 7.2: Engineering Goals

Analysis and control pipelines are a long-term investment in the project, and scalability in software instrumentation will enable rapid iteration of the physical instrument and continuity towards the full Argus Optical Array. In addition to the science-driven goals above, we are developing Argus-HDPS with the following engineering goals:

1. Scalability and adaptability from the prototype stage to the 900-telescope Argus Optical Array
2. Integration between the control system and analysis system to minimize latency and intermediate storage requirements
3. Maintainability of the codebase, using standard version control,[2] dependency management,[3] and automated testing[4] tools
4. Reliability for long-term operation and production of a stable dataset, including hardware-in-the-loop testing of cameras and focusers

Particularly at the current stage, adaptability to a heterogeneous instrument has been essential to enable rapid prototyping while navigating the supply chain constraints early in

---

[2] https://git-scm.com

[3] https://python-poetry.org

[4] https://pytest.org

the prototyping process, and will remain an important feature of HDPS to support long-term evaluation of telescopes and cameras with Argus Pathfinder. Between the A2TD and Pathfinder instruments, Argus-HDPS includes support for two camera manufacturers (Atik Cameras[5] and QHYCCD[6]), five camera models, and two telescopes with associated focusing hardware (the Celestron[7] RASA-8 and a custom Astrograph from Planewave Instruments[8])

Section 7.3: System Architecture

To meet the science and engineering goals of the Argus Optical Array, while coping with data rates into the terabit-per-second regime, we use a converged data collection and analysis pattern, in which images are reduced into data products within the observing cadence. In Figure 7.1, we present a flowchart of the basic components of Argus-HDPS, including the core processes and data products.

Integration between hardware control and data analysis systems is essential for reliable data caching and storage management, and for latency optimization at the fastest cadence. HDPS uses a modular software architecture for hardware control, based on a stable contract between core system components (optical and mechanical control, weather and instrument state monitoring, and pipeline instances), defined using HTTP APIs.

7.3.1 Camera Control

Each camera is directly connected to a camera command (CC) compute node capable of reducing its data in real time. We have developed Argus-HDPS wrappers for the vendor-supplied camera SDKs from Atik Cameras and QHYCCD, which abstract the basic functions of the cameras to a standard, shared Python API. Each CC node communicates with state machine processes exporting this API using an internal socket server. To minimize latency,

---

[5] https://www.atik-cameras.com

[6] https://www.qhyccd.com

[7] https://www.celestron.com

[8] https://planewave.com

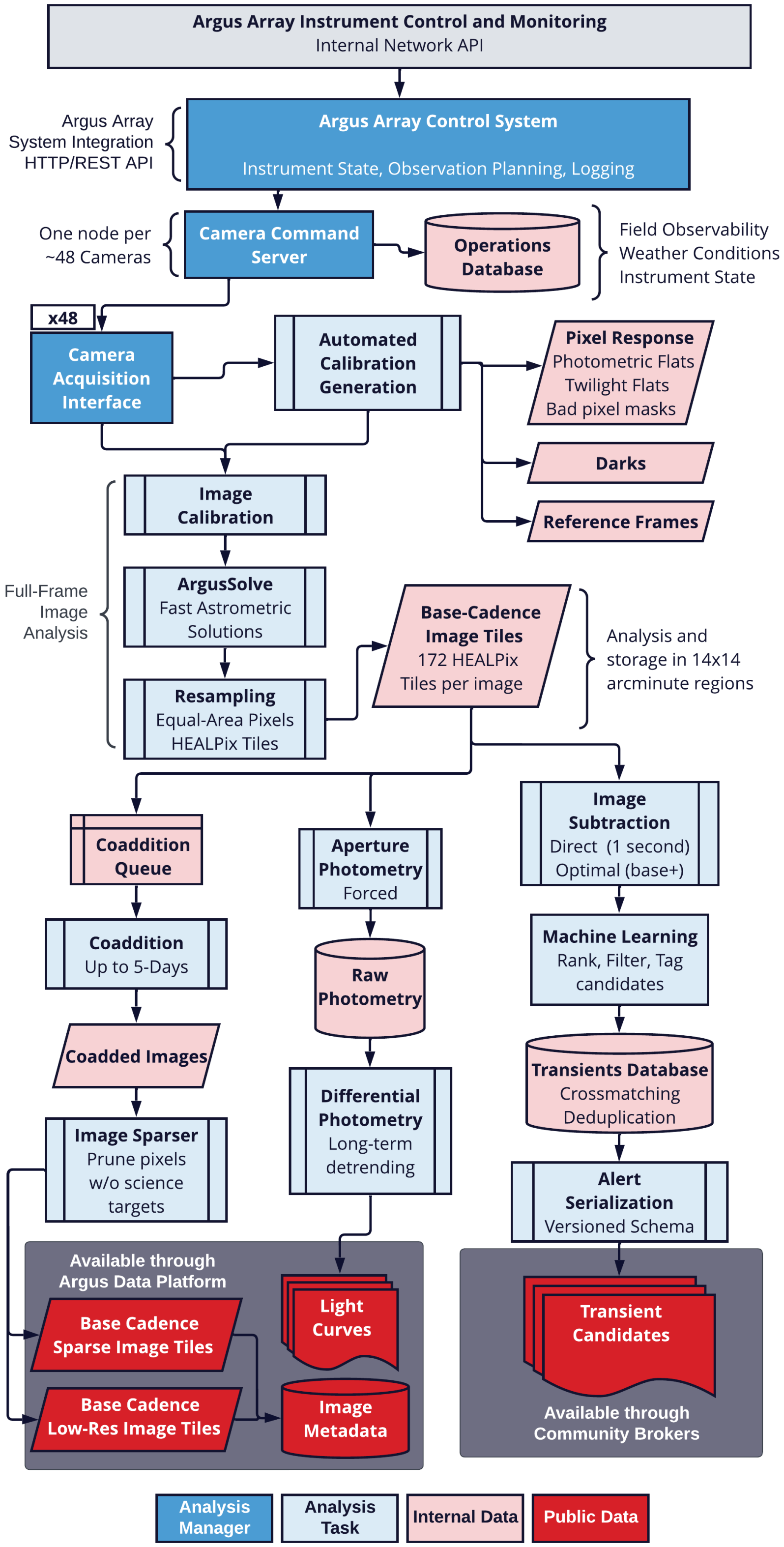

Figure 7.1 Pipeline components, processes, and data products for the Argus Optical Array.

camera control processes copy the image data, along with corresponding metadata, directly into a shared memory object store (Apache Plasma[9]), from which images are written to disk on a rolling basis. Cameras attached to each CC node can be controlled collectively using an asynchronous HTTP API by the instrument control system. The control system can control an arbitrary number of CC nodes (19 for the full Argus Optical Array).

7.3.2 Compute Nodes

CC nodes are standard many-core x86 rack-mounted servers, co-located with the instrument. Individual cameras connect to the CC nodes via USB 3.0 and high-density PCIe expansion cards. CC nodes will each be equipped with a GPU for image analysis. GPU requirements are primarily driven by memory size and bandwidth; in addition to the images themselves, each camera has a corresponding set of calibration frames (darks, flats, bad pixel masks, plus intermediate background and noise maps) and reference frames, which must also be transferred to the GPU at the start of each ratchet. Each compute node is also equipped with ∼50 TiB of local storage for temporary caching of full-frame data at 30-second cadence, and enough RAM to cache data at 1-second cadence for up to one minute.

Section 7.4: Pipeline Implementation

Once each full-frame image has been recorded in the in-memory object cache, analysis is delegated to analysis processes. Each analysis process pre-allocates the relevant reference and calibration frames on the CC node's GPU resources at the start of each pointing. CMOS image calibration, source detection, and resampling to the HEALPix grid are done directly on the GPU, and source catalogs are transferred to system memory for cross-matching and astrometric fitting on the CPU. In the current implementation, image subtraction and coaddition are also done on the CPU.

---

[9] https://arrow.apache.org

7.4.1 Image Management

The highest-data-rate components of Argus-HDPS are those which interface with with the full-resolution 61-MPix images from the cameras. These images are both unwieldy to access, with 122 MB file sizes that incur a disk read penalty on the order of the exposure time, and require external indexing via a database to be searchable in space or time. To support these standard usage patterns, we have developed a hierarchical, equal-area storage system for Argus Array data, inspired by, but distinct from, the Hierarchical Progressive Survey (HiPS) format described in Fernique et al. (2017).

In the full-frame images, we perform standard image calibrations (dark subtraction, flat fielding, masking of bad pixels) and fit an astrometric solution using a custom high-speed solver. The ArgusSolve astrometry algorithm is based on the quadrilateral hashing (Lang et al. 2010) and the fitting (Ofek 2019). Combined with an optimized implementation in Python, a one-directional mapping from celestial to pixel-plane coordinates for full-frame images can be produced in ~ 100 milliseconds. A full WCSLIB-compatible FITS header (Calabretta 2011) can optionally be generated for the full-frame image in ~ 5 s.

7.4.1.1 Image Segmentation

Each full-frame image is reprojected into equal-sky-area tiles (based on the HEALPix (Górski et al. 2005) pixelization scheme with NSIDE=256), providing 786,432 potential 13.7×13.7 arcminute sky regions across the celestial sphere, of which 58.6% will be observable by a Northern Hemisphere Argus Optical Array. The resulting segment images are stored in a structured tree of directories, grouped based on membership of each segment in the hierarchy of HEALPix tiles with NSIDE=4,16,64. Grouping the directories in this way is done to minimize the number of files per directory. Within each directory, images are stored per-night as multi-extension cubes in a FITS-like format modified to support 16-bit floating point data. Given a time and sky position, this scheme allows the path for a given spatial/temporal image tile to be uniquely determined without an external index, while maintaining a number of files on disk that is manageable with standard filesystems.

7.4.1.2 Sparse Image Segments

Each set of image segments for a single full-frame image is approximately the same size as the original data; however, each image tile can be further partitioned and selectively compressed. We have developed a "stamping" procedure, in which "minipix" segments of each image tile (at a higher HEALPix level, corresponding to NSIDE=16384) not containing science targets (either those detected in image subtractions or pre-cataloged by the science team) are set to zero and the resulting image compressed. To minimize the impacts on serendipitous science cases, full resolution images at base cadence will be cached at least up to the longest coaddition epoch (5 days), and low resolution maps, at a pixel scale of 13.8 arcsec per pixel, will be saved for the whole sky. The compressed sparse and low-resolution segment images combined take up $\sim 5\%$ the storage space of the full-resolution segments.

7.4.1.3 Deep Coaddition in Sky Segments

Because the full-resolution image tiles are pre-aligned to a fixed HEALPix grid, coaddition is greatly simplified. Coaddition on Argus sky tiles is optimized for point-source detection using a per-image matched filter, which is the statistically optimal method for background-limited images (Zackay & Ofek 2017). Figure 7.2 shows a deep coadd of a set of 30× 30-second exposures, made using the algorithm described in Zackay & Ofek (2017). These images were collected from a site local to our UNC-Chapel Hill lab, so the achievable depth is not representative of median performance at a dark-sky site; however, the 5-σ limiting magnitudes of $m_g = 17.8$ at 30s and $m_g = 19.8$ at 15 minutes are reproducible from the same calculation we use to predict dark sky performance, given typical sky brightness for a moderately-dark suburb ($m_V \sim 19$ per sq. arcsec). We reduced the images in Figure 7.2 using the Argus-HDPS GPU/CPU pipeline, including image segmentation, reprojection, and astrometry.

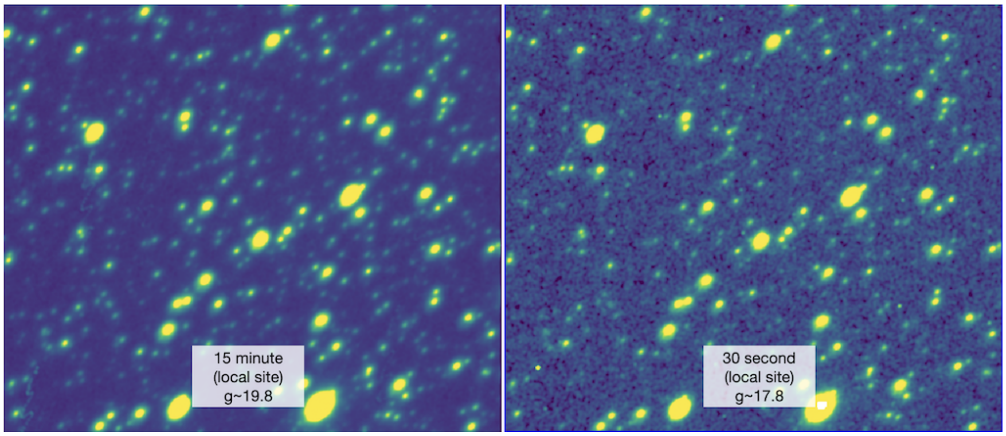

Figure 7.2 A 15-minute coadd of data from a Celestron RASA8 node of A2TD. Full-frame images from each sensor are reprojected into HEALPix segments, which are then used for further analysis tasks (photometry, image subtraction, and coaddition.)

7.4.2 Transient Alerts

Argus Pathfinder will produce transient candidates at a rate of approximately one million per night, and the full Argus Optical Array could meet or exceed the alert rate of the Rubin Observatory. Transient detection is performed using image subtraction in the reprojected HEALPix image segments, leveraging long-term coadds as reference frames. We have implemented two different algorithms for image subtraction in Argus-HDPS, and both will undergo long-term on-sky evaluation with Argus Pathfinder; the ZOGY algorithm described in Ref. 273 for image subtraction at base cadence and in deep coadds at 15-minute cadence or greater, and the direct image subtraction method we previously developed for the low-latency transient discovery pipeline for the Evryscopes (Corbett et al. 2020; Corbett et al. 2023), for real-time operation in 1-second cadence data. Figure 7.3 shows an image segment with a simulated transient source, a reference image, and subtraction images made using both subtraction algorithms.

In collaboration with the Arizona-NOIRLab Temporal Analysis and Response to Events System (Saha et al. 2014; Matheson et al. 2021; ANTARES;), we are prototyping a public transient alert system for low-latency release of candidates from the Argus Optical Array. To

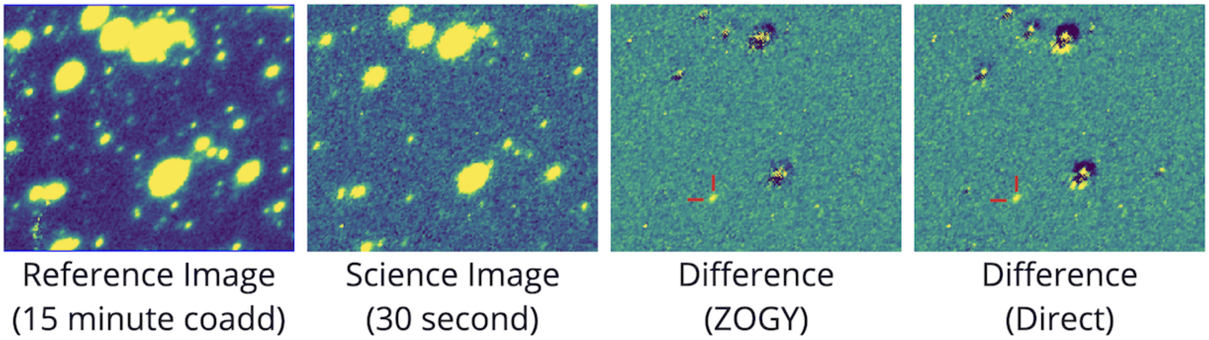

Figure 7.3 Per-tile image subtraction near an injected transient source with a 5-σ peak significance, using both the high-speed direct subtraction algorithm of Ref. 61, and the ZOGY(Zackay et al. 2016) algorithm.

maximize utility and ease of use for the community, we are adopting the evolving community standard of streaming serialized alert packets via Apache Kafka.[10].

7.4.3 Light Curves

Full evaluation of the expected precision of lightcurves from the Argus Optical Array will be made using data from Argus Pathfinder; however, initial results from A2TD nodes indicate that sub-percent performance may be achievable, at least on short timescales. Figure 7.4 shows the RMS vs magnitude for 900 stars during a single 15-minute ratchet at 30-second cadence, before and after three iterations of detrending using the SYSREM algorithm (Tamuz et al. 2005), which achieves ~ 7 mmag performance at the bright end.

Section 7.5: Pipeline Performance and Summary

We are developing Argus-HDPS, an integrated instrument control and data analysis system for the Argus Optical Array, which uses asynchronous HTTP connections to orchestrate observation and analysis tasks across multiple control servers that pair optical/camera control with edge GPU computing capabilities for minimal latency. For current prototyping stages, all analysis will be completed on a single x86 server; scaling to a full 900-telescope system can be

---

[10] https://kafka.apache.org/

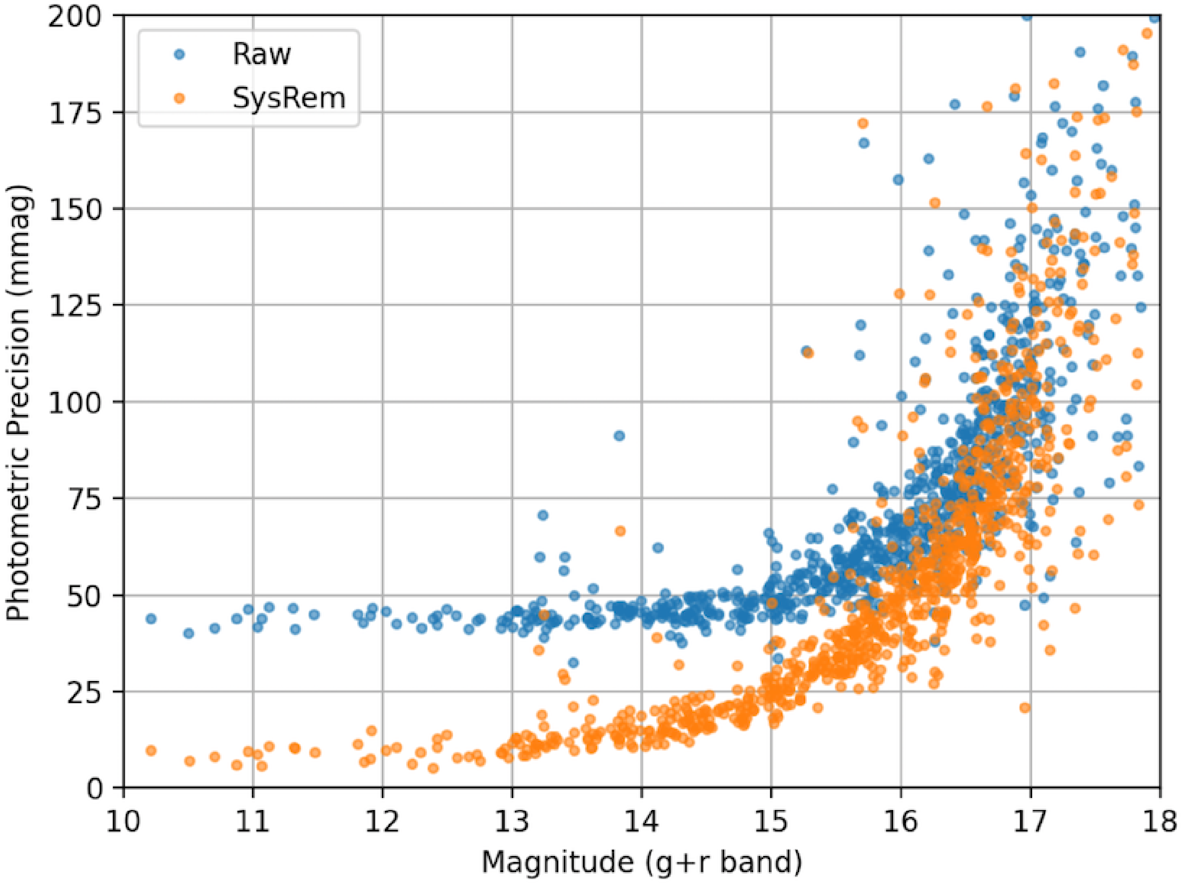

Figure 7.4 Photometric RMS vs. Magnitude for 900 stars across a single 15-minute pointing of A2TD at 30-second cadence.

accomplished linearly with the addition of 19 additional control servers. This system enables a low-latency sharing of instrument state with an O(1000) camera array, and allows for images to enter the analysis pipeline within 100 ms of camera readout. We have demonstrated real-time image data product generation, using a custom high-speed astrometric solver and GPU-based reprojection of sensor-plane data to produce equal-area image segments, which are then coadded and subtracted for transient detection at both single-image cadence and in deep coadds. Public data release of imaging and transient alert data from the Argus Optical Array is planned, and will be publicly prototyped after a commissioning period.

Table 7.2 presents the average compute time for the image segmentation and analysis pipeline stages, measured using a representative 36-core test server and an Nvidia RTX 3090

Ti GPU. Source detection, astrometry, and segmentation to the HEALPix grid are completed in an average of only 27 milliseconds on the GPU, which can be shared sequentially by many cameras to generate image data products in real time, even at 1-second cadence. CPU-based image subtraction is possible within cadence by parallelizing the direct subtraction at the segment level; however, a GPU implementation is in development.

Table 7.2 Average timing results for key processing steps in Argus-HDPS.

GPU Timing	
61-MPix image copy to GPU	16 ms
Calibration	< 1 ms
Median-filtered background map	1.7 ms
Source detection	6.1 ms
Image segmentation and resampling to HEALPix grid	3.2 ms
CPU Timing (single-threaded)	
Source de-duplication	7.5 ms
Astrometric solution	190 ms (95 ms with caching) (95 ms with caching)
Writing to modified FITS	475 ms
Compressed image generation	300 ms (batch reduction)
Direct image subtraction	20 ms per tile
ZOGY image subtraction	1400 ms per tile

CHAPTER 8: CONCLUSIONS

Section 8.1: EFTE and VetNet

In Chapters 2 and 3, we presented the Evryscope Fast Transient Engine (EFTE), the real-time transient discovery pipeline for the Evryscopes. The pipeline is a fully custom data analysis tool, suited to the unique parameter space inhabited by the Evryscopes and capable of identifying transient candidates in real-time, with alerts available for each image within the two-minute cadence of the Evryscopes for 98.5% of images. To accomplish this, we reduce the complex image subtraction process adopted by seeing-limited surveys to a simple direct subtraction of near-consecutive images. Astrometric performance for transient alerts is sub-pixel at the 99th percentile, and photometric performance is within 0.06 mag RMS of the ATLAS-RefCat2 catalog for reference stars within the $8 < m_g < 14.5$ sensitivity range of the survey. Using a convolutional real-bogus classifier, we are able to recover 99.9% of sources brighter than $m_g = 13.2$ with a false positive rate of 5.1%.

While EFTE is specifically adapted to Evryscope data, the infrastructure, algorithms, and ML models were developed to enable portability to instruments with similar survey strategies, such as the NASA Transiting Exoplanet Survey Satellite (TESS; Ricker et al. 2014), or with stringent data throughput and reduction latency requirements. Core algorithms from EFTE have been adapted for usage in the pipeline of the Argus Optical Array, a 5-meter class multiplexed 55 GPix synoptic survey instrument currently in development (Law et al. 2022c;b). Argus will observe a field of view equivalent to Evryscope in alternating 1- and 30-second cadences, which produce up to 4.3 PiB and 145 TiB of raw data per night, respectively. To support this data rate, Argus data will be reduced in real time, producing low-latency transient alerts, photometry, and calibrated image data for distribution and storage. In Corbett et al. (2022a), we describe the Argus pipeline and data products, and demonstrate the direct subtraction algorithm described in Section 2.4 on the Argus Array Technology Demonstrator (Corbett et al. 2022b). The VetNet model described in Section 3.1 was optimized for direct image subtraction and Evryscope data; however, the framework for performing this optimization and for staged model training using both on-sky and simulated data was similarly portable to Argus.

A public alert stream from EFTE is in development, based on the evolving community standard, in use for the Zwicky Alert Distribution System (Patterson et al. 2019) and planned for the Rubin Observatory's Legacy Survey of Space and Time (LSST)[1], of serialized alert packets distributed via Apache Kafka (Kreps et al. 2011). Alerts will be available via the Arizona-NOIRLab Temporal Analysis and Response to Events System (ANTARES; Matheson et al. 2021). Details of the alert distribution system and alert schema contents will be addressed in future work.

Section 8.2: Orbital Foregrounds for Fast Astronomical Transients

Unlike the population of astrophysical transients, the population of objects in Earth orbit is rapidly evolving on human timescales. Since the beginning of the work undertaken here, the number of satellites in orbit has increased by more than a factor of two,[2], with the vast majority coming from a single commercial launch provider. Concerns about the impacts of satellites on ground-based astronomy are common, and in many cases, well-founded. For the upcoming Vera C. Rubin Observatory in particular, the cross-talk induced within the camera by bright streaks is an open problem under investigation (Tyson et al. 2020), and perhaps an unavoidable one (Alina Hu et al. 2022). The implications on the growing number of satellite constellations on the population of satellite glints described in Chapter 4, however, is somewhat less clear. In collaboration with Rubin scientists, I recreated the 2020 analysis

---

[1] https://dmtn-093.lsst.io

[2] https://www.ucsusa.org/resources/satellite-database

to measure the glint rate using a sample of Evryscope-North data from 2022 and updated versions of EFTE and VetNet. Figure 8.1 shows the integrated all-sky event rate for both 2020 and 2022. I found that the glint rate was broadly consistent with the earlier measurement from the 2020 dataset, though the $\sim 30\%$ increase at the 50th percentile for dimmer targets is suggestive.

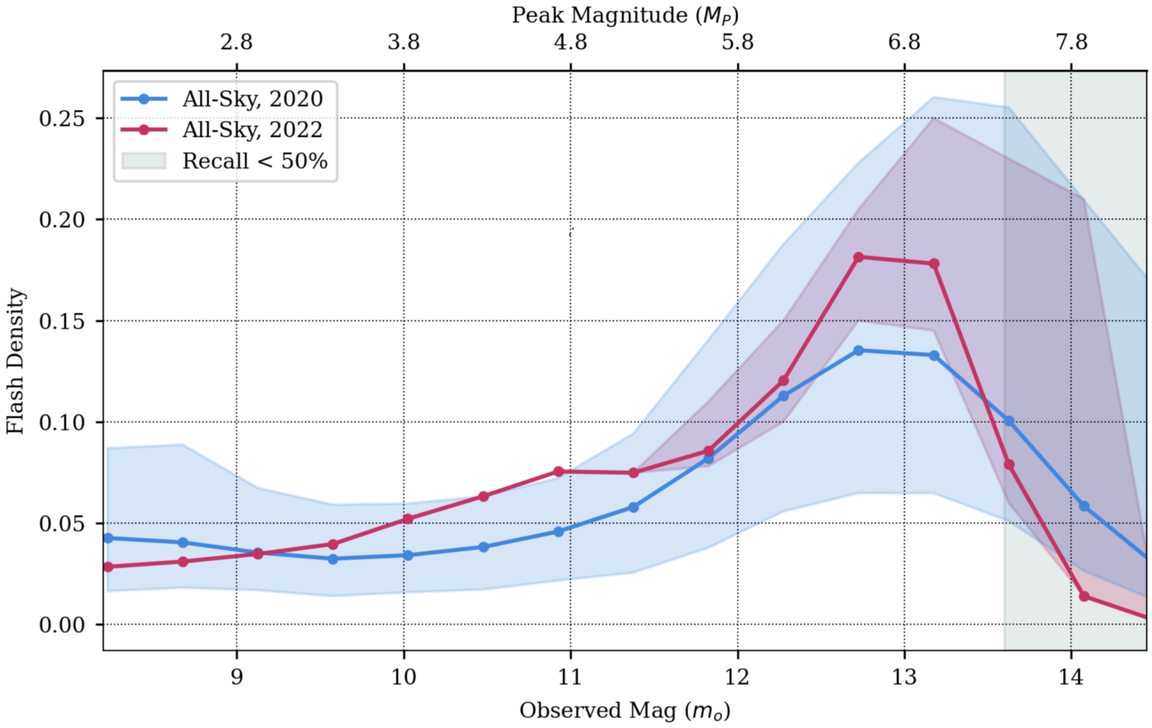

Figure 8.1 Rate of satellite glints as a function of magnitude as measured by Evryscope, both in 2020 as presented in Corbett et al. (2020) and updated based on the 2022 Evryscope-North dataset. Results are broadly consistent between the two years, despite the factor of two increase in the number of artificial Earth satellites.

Section 8.3: Prospects for Fast Duration Transient Searches with Argus Pathfinder

The upcoming Argus Optical Array, and the now-operating Argus Pathfinder, have the potential to systematically explore the sub-minute time domain. In this section, I will discuss the sensitivity of the nominal Argus survey, both specifically for optical counterparts to fast radio bursts (FRBs), and more generally for fast transients of any origin.

8.3.1 Searches for Optical Counterparts to FRBs

A multiwavelength discovery of an FRB counterpart would provide transformative constraints on the progenitor(s) and emission mechanism. A variety of models predicting optical emission have been proposed in the literature, ranging from a shared mechanism with the FRB on ms-timescales to long-lasting (seconds-to-minutes) afterglows (Yi et al. 2014). Assuming that at least some of the cosmological FRBs have a magnetar origin, like FRB 20200428A (Bochenek et al. 2020; Mereghetti et al. 2020; CHIME/FRB Collaboration et al. 2020), corresponding optical flashes generated by synchrotron emission are possible, particularly for repeaters, where blast wave collisions at the boundary between the stellar wind and the hot, slow tail. Beloborodov (2020) estimates that resulting luminosity could exceed that of a type Ia supernova, releasing up to 10^{44} ergs on 1-second timescales, detectable by Pathfinder out to z=0.05 at 1-second cadence. The inverse Compton scattering model discussed in Yang et al. (2019), predicts dimmer emission on ms-timescales, and while Pathfinder is not as sensitive as larger instruments like Rubin, the flux dilution factor (the ratio of the exposure time to the emission timescale) enables competitive flux sensitivity for millisecond-timescale flashes. For a 1 ms event, Argus Pathfinder will have a limiting flux of 0.9 Jy, compared to 0.01 Jy for Rubin and 0.5 Jy for Tomo-e Gozen (Sako et al. 2018), all computed using the scaling relations for the AB magnitudes from Lyutikov & Lorimer (2016); however, the areal survey rate (product of instantaneous FoV and exposure time) of Argus Pathfinder is 1100x that of an idealized Rubin survey, and comparable to that of Tomo-e Gozen, a dedicated high-speed survey instrument (Sako et al. 2018).

During a hypothetical Pathfinder survey at the Evryscope-North site (MLO), we could adopt a pointing strategy that places one of the three right ascension columns 3.2 degrees to the west of the local meridian towards the CHORD field of view to provide simultaneous monitoring of $\sim 20\%$ of all CHORD-detected FRBs, enabling the largest ever systematic search for simultaneous optical counterparts to both repeating and non-repeating FRBs with comparable optical/radio flux sensitivities. While the optical candidates will include foreground contaminants like glints from artificial Earth satellites (Corbett et al. 2020; Nir et al. 2021; Karpov & Peloton 2022), the coincidence probability within a conservative 1 arcsec optical localization region and a satellite reflection is $O(10^{-7})$, even when extrapolating to 10x the current rate of satellite debris signals to account for the rapidly increasing utilization of orbital space. Beyond this, the pre-burst monitoring of the field will allow us to resolve track-like event sequences from isolated, potentially astrophysical, candidates.

8.3.2 Exotic Extragalactic Fast Transients

Beyond FRBs, Argus will be sensitive to a variety of other classes of fast optical transients, independent of external triggers from multi-wavelength or multi-messenger observatories. These events include known, but uncommon, events like prompt optical flashes from gamma-ray bursts (Fox et al. 2003; Cucchiara et al. 2011; Vestrand et al. 2014; Martin-Carrillo et al. 2014; Troja et al. 2017), shockwave breakout from young supernovae (Garnavich et al. 2016; Bersten et al. 2018; Vallely et al. 2021), and stellar superflares (Kulkarni & Rau 2006; Howard et al. 2018a).

Due to the dense time sampling and huge control time of Argus Pathfinder's high-speed survey, we will be able to place the most stringent limits for the rate of dim, second-timescale extragalactic transients, reaching four orders of magnitude beyond the closest comparable limits (Richmond et al. 2020) for 1-second duration transients. Pathfinder will also be able to constrain the population of O(10s) duration transients, pushing limits 8.5 magnitudes deeper than previously probed by Pi of the Sky (Sokołowski et al. 2010) and filling in the intermediate parameter space between the 1-second cadence Argus Pathfinder survey and the deep, minute-cadence observations reported by the Deeper-Wider-Faster program (Andreoni et al. 2020a) using the Dark Energy Camera (Flaugher et al. 2015).

To assess the potential impact of the Pathfinder survey on the search for exotic high-speed transients, we can consider the potential upper limits that it could produce in a nominal 3-year survey with a 70/30 split between 30-second and 1-second cadence operating modes based on the expected control time for these events (Zwicky 1938), representing the amount of time that the event would be detectable by the survey, should they occur. While number of discoveries would be a preferable metric, at this time, the population is unconstrained, so upper limits provide a reasonable basis for comparison between experiments and surveys.

Richmond et al. (2020) calculated a 95% confidence-level areal rate (λ) limit of 1.46 events deg^{-2} day^{-1} with a limiting magnitude of V=15.6 using the Tomo-e Gozen instrument (Sako et al. 2018). Comparatively, the Pathfinder 1s-cadence survey could place limits as low as 0.00017 deg^{-2}d ay^{-1}, with a limiting magnitude equivalent to $g = 16.1$, slightly deeper than Tomo-e Gozen. In the 30s-cadence base survey, Pathfinder will provide similarly competitive event rates for eFOTS on O(10s) timescales, filling in the unknown region between the bright ($V \sim 11$) all-sky limits from Pi of the Sky ($\lambda \leq 5 \times 10^{-5}$ deg^{-2} day^{-1}, Sokołowski et al. (2010)) and the deep (g 23.7), narrow-field limits from Deeper-Wider-Faster ($\lambda \leq 1.625$ deg^{-2} day^{-1}, Andreoni et al. (2020a)). Over a 3-year survey, Pathfinder will establish limits for events on similar timescales at intermediate depth ($g \sim 19.1$) with an areal rate sensitivity of 0.0018 events deg^{-2} day^{-1}. The full Argus Optical Array, running the same 3-year survey as Pathfinder, would be able to establish limits of 4.3×10^{6} events deg^{-2} day^{-1} and 4.8×10^{5} events deg^{-2} day^{-1}, based on the 30- and 1-second cadence operating modes, respectively. Figure 1.2 shows the prospective upper limits for the Argus Pathfinder and Argus Optical Array in the context of established limits from the literature.

Section 8.4: Closing Thoughts

The apparatus for a conclusive census of the phenomenology of the night sky on days-to-weeks timescales is in place, with a key pivot being the first light of the Rubin Observatory's Legacy Survey of Space and Time – currently anticipated for the third quarter of 2024. However, the parameter space of bright and fast-evolving phenomena, and even more so, *dim* and fast-evolving phenomena, remains enigmatic and technically difficult. Among the windows to the universe through which we are currently able to peer, optical astronomy is perhaps the farthest behind in this respect. The IceCube Neutrino Observatory can localize events from trajectories across half of the sky within its square kilometer of detector with a precision of 3 ns (IceCube Collaboration et al. 2017). LIGO records even more exacting time precision across the entire sky (Abbott et al. 2009), and both operating (The CHIME/FRB Collaboration et al. 2018) and upcoming (Vanderlinde et al. 2019) radio observatories with massively-multiplexed fields of view can cover hundreds of square degrees with ms-scale sampling. Multiple gamma-ray telescopes now monitor large fractions of the sky near-constantly (Gehrels et al. 2004; Bhat et al. 2009).

In contrast, optical astronomy is primarily conducted target by target, field by field. Though digitized, the conventional image-based approaches are similar in form-factor to historical photographic emulsions on glass plates. Such approaches are a difficult fit for this high-speed time domain and parameter space of uncommon events. It is my sincere hope that the techniques and approaches described here, developed for the relatively conventional wide-field Evryscope and Argus cameras, will help guide future efforts to both detect and discover what strange flashes we may find.

REFERENCES

Abadi, M., Agarwal, A., Barham, P., et al. 2015, TensorFlow: Large-Scale Machine Learning on Heterogeneous Systems. https://www.tensorflow.org/

Abbott, B. P., Abbott, R., Adhikari, R., et al. 2009, Reports on Progress in Physics, 72, 076901, "10.1088/0034-4885/72/7/076901"

Agarap, A. F. 2018, arXiv preprint arXiv:1803.08375

Aizawa, M., Kawana, K., Kashiyama, K., et al. 2022, Publications of the Astronomical Society of Japan, 74, 1069, "10.1093/pasj/psac056"

Alard, C., & Lupton, R. H. 1998, Astrophysical Journal, 503, 325, "10.1086/305984"

Aldering, G., Adam, G., Antilogus, P., et al. 2002, in Society of Photo-Optical Instrumentation Engineers (SPIE) Conference Series, Vol. 4836, Survey and Other Telescope Technologies and Discoveries, ed. J. A. Tyson & S. Wolff, 61–72, "10.1117/12.458107"

Alina Hu, J., Rawls, M. L., Yoachim, P., & Ivezić, Ž. 2022, arXiv e-prints, arXiv:2211.15908, "10.48550/arXiv.2211.15908"

Allred, J. C., Hawley, S. L., Abbett, W. P., & Carlsson, M. 2006, The Astrophysical Journal, 644, 484, "10.1086/503314"

Allred, J. C., Kowalski, A. F., & Carlsson, M. 2015, The Astrophysical Journal, 809, 104, "10.1088/0004-637X/809/1/104"

Anders, F., Khalatyan, A., Chiappini, C., et al. 2019, Astronomy & Astrophysics, 628, A94, "10.1051/0004-6361/201935765"

Anders, F., Khalatyan, A., Queiroz, A. B. A., et al. 2022, Astronomy & Astrophysics, 658, A91, "10.1051/0004-6361/202142369"

Anderson, J., & King, I. R. 2000, Publications of the Astronomical Society of the Pacific, 112, 1360, "10.1086/316632"

Andreoni, I., Jacobs, C., Hegarty, S., et al. 2017, Publications of the Astronomical Society of Australia, 34, e037, "10.1017/pasa.2017.33"

Andreoni, I., Cooke, J., Webb, S., et al. 2020a, Monthly Notices of the Royal Astronomical Society, 491, 5852, "10.1093/mnras/stz3381"

Andreoni, I., Lu, W., Smith, R. M., et al. 2020b, The Astrophysical Journal Letters, 896, L2, "10.3847/2041-8213/ab94a5"

Arcavi, I. 2022, Astrophysical Journal, 937, 75, "10.3847/1538-4357/ac90c0"

Arimatsu, K., Tsumura, K., Usui, F., Ootsubo, T., & Watanabe, J.-i. 2021, The Astronomical Journal, 161, 135, "10.3847/1538-3881/abd94d"

Bailey, S., Aragon, C., Romano, R., et al. 2008, Astronomische Nachrichten, 329, 292, "10.1002/asna.200710932"

Bakos, G., Noyes, R. W., Kovács, G., et al. 2004, PASP, 116, 266, "10.1086/382735"

Barbary, K. 2016, Journal of Open Source Software, 1, 58, "10.21105/joss.00058"

Barrau, A., Rovelli, C., & Vidotto, F. 2014, Physical Review D, 90, 127503, "10.1103/PhysRevD.90.127503"

Bassa, C. G., Tendulkar, S. P., Adams, E. A. K., et al. 2017, The Astrophysical Journal Letters, 843, L8, "10.3847/2041-8213/aa7a0c"

Becker, A. 2015, HOTPANTS: High Order Transform of PSF ANd Template Subtraction. http://ascl.net/1504.004

Behnel, S., Bradshaw, R., Citro, C., et al. 2011, Computing in Science & Engineering, 13, 31

Bellm, E. C. 2016, Publications of the Astronomical Society of the Pacific, 128, 084501, "10.1088/1538-3873/128/966/084501"

Bellm, E. C., Kulkarni, S. R., Graham, M. J., et al. 2019, Publications of the Astronomical Society of the Pacific, 131, 018002, "10.1088/1538-3873/aaecbe"

Beloborodov, A. M. 2020, The Astrophysical Journal, 896, 142, "10.3847/1538-4357/ab83eb"

Berger, E., Leibler, C. N., Chornock, R., et al. 2013, Astrophysical Journal, 779, 18, "10.1088/0004-637X/779/1/18"

Beroiz, M., Cabral, J., & Sanchez, B. 2020, Astronomy and Computing, 32, 100384, "https://doi.org/10.1016/j.ascom.2020.100384"

Berry, R., & the Celestron Engineering Team. 2020, Big! Fast! Wide! Sharp! The Story of the Rowe-Ackermann Schmidt Astrograph, https://celestron-site-support-files.s3.amazonaws.com/support_files/RASA_White_Paper_2020_Web.pdf

Bersten, M. C., Folatelli, G., García, F., et al. 2018, Nature, 554, 497, "10.1038/nature25151"

Bertin, E. 2011, in Astronomical Society of the Pacific Conference Series, Vol. 442, Astronomical Data Analysis Software and Systems XX, ed. I. N. Evans, A. Accomazzi, D. J. Mink, & A. H. Rots, 435

Bertin, E., & Arnouts, S. 1996, Astronomy & Astrophysicss, 117, 393, "10.1051/aas:1996164"

Bhandari, S., Keane, E. F., Barr, E. D., et al. 2018, Monthly Notices of the Royal Astronomical Society, 475, 1427, "10.1093/mnras/stx3074"

Bhandari, S., Heintz, K. E., Aggarwal, K., et al. 2022, Astronomical Journal, 163, 69, "10.3847/1538-3881/ac3aec"

Bhat, P. N., Meegan, C. A., Lichti, G. G., et al. 2009, in American Institute of Physics Conference Series, Vol. 1133, American Institute of Physics Conference Series, ed. C. Meegan, C. Kouveliotou, & N. Gehrels, 34–36, “10.1063/1.3155916”

Biryukov, A., Beskin, G., Karpov, S., et al. 2015, Baltic Astronomy, 24, 100, “10.1515/astro-2017-0208”

Blake, J. A., Chote, P., Pollacco, D., et al. 2020, arXiv e-prints, arXiv:2008.12799. https://arxiv.org/abs/2008.12799

Bloom, J. S., Starr, D. L., Butler, N. R., et al. 2008, Astronomische Nachrichten, 329, 284, “10.1002/asna.200710957”

Bochenek, C. D., Ravi, V., Belov, K. V., et al. 2020, Nature, 587, 59, “10.1038/s41586-020-2872-x”

Bramich, D. 2008, Monthly Notices of the Royal Astronomical Society, 386, “10.1111/j.1745-3933.2008.00464.x”

Breiman, L. 2001, Machine Learning, 45, 5, “10.1023/A:1010933404324”

Brink, H., Richards, J. W., Poznanski, D., et al. 2013, Monthly Notices of the Royal Astronomical Society, 435, 1047, “10.1093/mnras/stt1306”

Burke, C. J., Aleo, P. D., Chen, Y.-C., et al. 2019, Monthly Notices of the Royal Astronomical Society, 490, 3952, “10.1093/mnras/stz2845”

Butler, H., Daly, M., Doyle, A., et al. 2016, The GeoJSON Format, “10.17487/RFC7946”

Bäuerle, A., van Onzenoodt, C., & Ropinski, T. 2021, IEEE Transactions on Visualization and Computer Graphics, 27, 2980, “10.1109/TVCG.2021.3057483”

Calabretta, M. R. 2011, Wcslib and Pgsbox, Astrophysics Source Code Library, record ascl:1108.003. http://ascl.net/1108.003

Calabretta, M. R., Valdes, F., Greisen, E. W., & Allen, S. L. 2004, in Astronomical Society of the Pacific Conference Series, Vol. 314, Astronomical Data Analysis Software and Systems (ADASS) XIII, ed. F. Ochsenbein, M. G. Allen, & D. Egret, 551

Candelaresi, S., Hillier, A., Maehara, H., Brandenburg, A., & Shibata, K. 2014, The Astrophysical Journal, 792, 67, “10.1088/0004-637X/792/1/67”

Cao, Y., Nugent, P. E., & Kasliwal, M. M. 2016, arXiv, “10.1088/1538-3873/128/969/114502”

Chawla, P., Kaspi, V. M., Josephy, A., et al. 2017, The Astrophysical Journal, 844, 140, “10.3847/1538-4357/aa7d57”

CHIME/FRB Collaboration, Andersen, B. C., Bandura, K. M., et al. 2020, Nature, 587, 54, “10.1038/s41586-020-2863-y”

Chollet, F., et al. 2015, Keras, GitHub. https://github.com/fchollet/keras

Cisco. 2021, Annual Visual Networking Index, https://www.cisco.com/c/dam/m/en_us/solutions/service-provider/vni-forecast-highlights/pdf/Global_2021_Forecast_Highlights.pdf

Clemens, J. C., Crain, J. A., & Anderson, R. 2004, in Society of Photo-Optical Instrumentation Engineers (SPIE) Conference Series, Vol. 5492, Ground-based Instrumentation for Astronomy, ed. A. F. M. Moorwood & M. Iye, 331–340, "10.1117/12.550069"

Corbett, H., Galliher, N., Gonzalez, R., Glazier, A., & Law, N. M. 2023, AAS Journals, *(in prep)*

Corbett, H., Law, N., Goeke, E., et al. 2018, The Astronomer's Telegram, 11467, 1

Corbett, H., Soto, A. V., Machia, L., et al. 2022a, in Software and Cyberinfrastructure for Astronomy VII, ed. J. Ibsen & G. Chiozzi, Vol. 12189, International Society for Optics and Photonics (SPIE), 1218910, "10.1117/12.2629533"

Corbett, H., Soto, A. V., Machia, L., et al. 2022b, in Ground-based and Airborne Telescopes IX, ed. H. K. Marshall, J. Spyromilio, & T. Usuda, Vol. 12182, International Society for Optics and Photonics (SPIE), 121824D, "10.1117/12.2629489"

Corbett, H., Vasquez Soto, A., Machia, L., et al. 2022, in Society of Photo-Optical Instrumentation Engineers (SPIE) Conference Series, Vol. 12189, Society of Photo-Optical Instrumentation Engineers (SPIE) Conference Series, 1218910, "10.1117/12.2629533"

Corbett, H., Law, N. M., Soto, A. V., et al. 2020, Astrophysical Journal Letters, 903, L27, "10.3847/2041-8213/abbee5"

Corbett, H., Carney, J., Gonzalez, R., et al. 2023, The Astrophysical Journal Supplement Series, 265, 63, "10.3847/1538-4365/acbd41"

Cornsweet, T. 2014, Visual Perception (Elsevier Science)

Covey, K. R., Hawley, S. L., Bochanski, J. J., et al. 2008, The Astronomical Journal, 136, 1778, "10.1088/0004-6256/136/5/1778"

Cucchiara, A., Cenko, S. B., Bloom, J. S., et al. 2011, Astrophysical Journal, 743, 154, "10.1088/0004-637X/743/2/154"

Cutri, R. M., Skrutskie, M. F., van Dyk, S., et al. 2003, 2MASS All Sky Catalog of point sources.

Cutri, R. M., Wright, E. L., Conrow, T., et al. 2013, Explanatory Supplement to the AllWISE Data Release Products, Explanatory Supplement to the AllWISE Data Release Products

Dálya, G., Galgóczi, G., Dobos, L., et al. 2018, Monthly Notices of the Royal Astronomical Society, 479, 2374, "10.1093/mnras/sty1703"

Dark Energy Survey Collaboration, Abbott, T., Abdalla, F. B., et al. 2016, Monthly Notices of the Royal Astronomical Society, 460, 1270, “10.1093/mnras/stw641”

Davenport, J. R. A., Hawley, S. L., Hebb, L., et al. 2014, The Astrophysical Journal, 797, 122, “10.1088/0004-637X/797/2/122”

Di Stefano, R., Fisher, R., Guillochon, J., & Steiner, J. F. 2015, arXiv e-prints, arXiv:1501.07837. https://arxiv.org/abs/1501.07837

Dieleman, S., Willett, K. W., & Dambre, J. 2015, Monthly Notices of the Royal Astronomical Society, 450, 1441, “10.1093/mnras/stv632”

Drake, A. J., Djorgovski, S. G., Mahabal, A., et al. 2009, Astrophysical Journal, 696, 870, “10.1088/0004-637X/696/1/870”

Dressing, C. D., & Charbonneau, D. 2013, The Astrophysical Journal, 767, 95, “10.1088/0004-637X/767/1/95”

—. 2015, The Astrophysical Journal, 807, 45, “10.1088/0004-637X/807/1/45”

Duev, D. A., Mahabal, A., Masci, F. J., et al. 2019, Monthly Notices of the Royal Astronomical Society, 489, 3582, “10.1093/mnras/stz2357”

Dunn, F. A., & Rieke, F. 2006, Current Opinion in Neurobiology, 16, 363, “10.1016/j.conb.2006.06.013”

Dyer, M. J., Dhillon, V. S., Littlefair, S., et al. 2018, in Society of Photo-Optical Instrumentation Engineers (SPIE) Conference Series, Vol. 10704, Observatory Operations: Strategies, Processes, and Systems VII, 107040C, “10.1117/12.2311865”

Fernique, P., Allen, M., Boch, T., et al. 2017, HiPS - Hierarchical Progressive Survey Version 1.0, IVOA Recommendation 19 May 2017, “10.5479/ADS/bib/2017ivoa.spec.0519F”

Fischler, M., & Bolles, R. 1981, Communications of the ACM, 24, 381. https://dl.acm.org/doi/10.1145/358669.358692

Flaugher, B., Diehl, H. T., Honscheid, K., et al. 2015, The Astronomical Journal, 150, 150, “10.1088/0004-6256/150/5/150”

Flewelling, H. A., Magnier, E. A., Chambers, K. C., et al. 2016, arXiv e-prints, arXiv:1612.05243. https://arxiv.org/abs/1612.05243

Fong, W.-f., Dong, Y., Leja, J., et al. 2021, The Astrophysical Journal Letters, 919, L23, “10.3847/2041-8213/ac242b”

Fouesneau, M. 2022, pyphot, 1.4.3. https://github.com/mfouesneau/pyphot

Fox, D. W., Price, P. A., Soderberg, A. M., et al. 2003, Astrophysical Journal Letters, 586, L5, “10.1086/374683”

Fresneau, A., & Osborn, W. H. 2009, Astronomy & Astrophysics, 503, 1023, “10.1051/0004-6361/200810798”

Froning, C. S., Kowalski, A., France, K., et al. 2019, arXiv e-prints, arXiv:1901.08647. https://arxiv.org/abs/1901.08647

Förster, F., Maureira, J. C., Martín, J. S., et al. 2016, arXiv, “10.3847/0004-637x/832/2/155”

Gaia Collaboration, Prusti, T., de Bruijne, J. H. J., et al. 2016, Astronomy & Astrophysics, 595, A1, “10.1051/0004-6361/201629272”

Gaia Collaboration, Brown, A. G. A., Vallenari, A., et al. 2018, Astronomy & Astrophysics, 616, A1, “10.1051/0004-6361/201833051”

—. 2021, Astronomy & Astrophysics, 649, A1, “10.1051/0004-6361/202039657”

Gaia Collaboration, Vallenari, A., Brown, A. G. A., et al. 2022, arXiv e-prints, arXiv:2208.00211, “10.48550/arXiv.2208.00211”

Gal, Y., & Ghahramani, Z. 2015a, arXiv e-prints, arXiv:1506.02142. https://arxiv.org/abs/1506.02142

—. 2015b, arXiv e-prints, arXiv:1506.02158. https://arxiv.org/abs/1506.02158

Galliher, N., Law, N., Corbett, H., et al. 2022a, in Society of Photo-Optical Instrumentation Engineers (SPIE) Conference Series, Vol. 12182, Ground-based and Airborne Telescopes IX

Galliher, N. W., Law, N. M., Corbett, H., et al. 2022b, in Society of Photo-Optical Instrumentation Engineers (SPIE) Conference Series, Vol. 12184, Ground-based and Airborne Instrumentation for Astronomy IX, ed. C. J. Evans, J. J. Bryant, & K. Motohara, 1218485, “10.1117/12.2630146”

García-Alvarez, D., Jevremović, D., Doyle, J. G., & Butler, C. J. 2002, Astronomy & Astrophysics, 383, 548, “10.1051/0004-6361:20011743”

Garnavich, P. M., Tucker, B. E., Rest, A., et al. 2016, Astrophysical Journal, 820, 23, “10.3847/0004-637X/820/1/23”

Gehrels, N., Chincarini, G., Giommi, P., et al. 2004, The Astrophysical Journal, 611, 1005, “10.1086/422091”

Geurts, P., Ernst, D., & Wehenkel, L. 2006, Mach. Learn., 63, 3–42, “10.1007/s10994-006-6226-1”

Ghosh, A., Manwani, N., & Sastry, P. S. 2016, arXiv e-prints, arXiv:1605.06296. https://arxiv.org/abs/1605.06296

Glazier, A. L., Howard, W. S., Corbett, H., et al. 2020, The Astrophysical Journal, 900, 27, “10.3847/1538-4357/aba4a6”

Goldstein, A., Fletcher, C., Veres, P., et al. 2020, The Astrophysical Journal, 895, 40, "10.3847/1538-4357/ab8bdb"

Goldstein, D. A., D'Andrea, C. B., Fischer, J. A., et al. 2015, The Astronomical Journal, 150, 82, "10.1088/0004-6256/150/3/82"

Gonzalez, R., Corbett, H., Law, N., et al. 2022, in Society of Photo-Optical Instrumentation Engineers (SPIE) Conference Series, Vol. 12182, Ground-based and Airborne Telescopes IX

Górski, K. M., & Hivon, E. 2011, HEALPix: Hierarchical Equal Area isoLatitude Pixelization of a sphere, Astrophysics Source Code Library, record ascl:1107.018. http://ascl.net/1107.018

Górski, K. M., Hivon, E., Banday, A. J., et al. 2005, The Astrophysical Journal, 622, 759, "10.1086/427976"

Griffin, S. C. 2012, in New Horizons in Time Domain Astronomy, ed. E. Griffin, R. Hanisch, & R. Seaman, Vol. 285, 321–323, "10.1017/S1743921312000932"

Gupta, P. D., & Saini, N. 2018, Journal of Astrophysics and Astronomy, 39, 14, "10.1007/s12036-017-9499-9"

Hamuy, M., Suntzeff, N. B., Heathcote, S. R., et al. 1994, Publications of the Astronomical Society of the Pacific, 106, 566, "10.1086/133417"

Hamuy, M., Walker, A. R., Suntzeff, N. B., et al. 1992, Publications of the Astronomical Society of the Pacific, 104, 533, "10.1086/133028"

Hardy, L. K., Dhillon, V. S., Spitler, L. G., et al. 2017, Monthly Notices of the Royal Astronomical Society, 472, 2800, "10.1093/mnras/stx2153"

Hawley, S. L., & Pettersen, B. R. 1991, Astrophysical Journal, 378, 725, "10.1086/170474"

Hawley, S. L., Walkowicz, L. M., Allred, J. C., & Valenti, J. A. 2007, Publications of the Astronomical Society of the Pacific, 119, 67, "10.1086/510561"

Hawley, S. L., Fisher, G. H., Simon, T., et al. 1995, The Astrophysical Journal, 453, 464, "10.1086/176408"

Hawley, S. L., Allred, J. C., Johns-Krull, C. M., et al. 2003, The Astrophysical Journal, 597, 535, "10.1086/378351"

Hedges, C., Luger, R., Martinez-Palomera, J., Dotson, J., & Barentsen, G. 2021, The Astronomical Journal, 162, 107, "10.3847/1538-3881/ac0825"

Heintz, K. E., Prochaska, J. X., Simha, S., et al. 2020, The Astrophysical Journal, 903, 152, "10.3847/1538-4357/abb6fb"

Heinze, A. N., Tonry, J. L., Denneau, L., et al. 2018, The Astronomical Journal, 156, 241, "10.3847/1538-3881/aae47f"

Henden, A. A., Templeton, M., Terrell, D., et al. 2016, VizieR Online Data Catalog, II/336

Henry, T. J., Jao, W.-C., Subasavage, J. P., et al. 2006, The Astronomical Journal, 132, 2360, “10.1086/508233”

Ho, A. Y. Q., Kulkarni, S. R., Nugent, P. E., et al. 2018, Astrophysical Journal Letters, 854, L13, “10.3847/2041-8213/aaaa62”

Hoffleit, D., & Jaschek, C. 1991, The Bright star catalogue (Yale University Observatory)

Høg, E., Fabricius, C., Makarov, V. V., et al. 2000, Astronomy & Astrophysics, 355, L27

Howard, W. S., Corbett, H., Law, N. M., et al. 2019, The Astrophysical Journal, 881, 9, “10.3847/1538-4357/ab2767”

Howard, W. S., & MacGregor, M. A. 2022, Astrophysical Journal, 926, 204, “10.3847/1538-4357/ac426e”

Howard, W. S., Tilley, M. A., Corbett, H., et al. 2018a, Astrophysical Journal Letters, 860, L30, “10.3847/2041-8213/aacaf3”

—. 2018b, The Astrophysical Journal Letters, 860, L30, “10.3847/2041-8213/aacaf3”

Howard, W. S., Corbett, H., Law, N. M., et al. 2020, The Astrophysical Journal, 895, 140, “10.3847/1538-4357/ab9081”

Howard, W. S., Corbett, H., Law, N. M., et al. 2020, Astrophysical Journal, 902, 115, “10.3847/1538-4357/abb5b4”

Howard, W. S., Teske, J., Corbett, H., et al. 2021, The Astronomical Journal, 162, 147, “10.3847/1538-3881/ac0fe3”

Hu, L., Wang, L., Chen, X., & Yang, J. 2022, Astrophysical Journal, 936, 157, “10.3847/1538-4357/ac7394”

IceCube Collaboration, Aartsen, M. G., Ackermann, M., et al. 2017, Journal of Instrumentation, 12, P03012–P03012, “10.1088/1748-0221/12/03/p03012”

Ioffe, S., & Szegedy, C. 2015, arXiv e-prints, arXiv:1502.03167. https://arxiv.org/abs/1502.03167

Jayasinghe, T., Kochanek, C. S., Stanek, K. Z., et al. 2018, Monthly Notices of the Royal Astronomical Society, 477, 3145, “10.1093/mnras/sty838”

Johnson, N. L. 1949, Biometrika, 36, 149, “10.1093/biomet/36.1-2.149”

Kaiser, N., Burgett, W., Chambers, K., et al. 2010, in Society of Photo-Optical Instrumentation Engineers (SPIE) Conference Series, Vol. 7733, Society of Photo-Optical Instrumentation Engineers (SPIE) Conference Series, 77330E, “10.1117/12.859188”

Karpov, S., Beskin, G., Biryukov, A., et al. 2016, in Revista Mexicana de Astronomia y Astrofisica Conference Series, Vol. 48, Revista Mexicana de Astronomia y Astrofisica Conference Series, 91–96

Karpov, S., & Peloton, J. 2022, arXiv e-prints, arXiv:2202.05719. https://arxiv.org/abs/2202.05719

Karpov, S., Beskin, G., Biryukov, A., et al. 2018, in SN 1987A, Quark Phase Transition in Compact Objects and Multimessenger Astronomy, 86–95, "10.26119/SAO.2020.1.52312"

Keller, S. C., Schmidt, B. P., Bessell, M. S., et al. 2007, Publications of the Astronomical Society of Australia, 24, 1, "10.1071/AS07001"

Kesseli, A. Y., West, A. A., Veyette, M., et al. 2017, The Astrophysical Journal Supplement Series, 230, 16, "10.3847/1538-4365/aa656d"

Killestein, T. L., Lyman, J., Steeghs, D., et al. 2021, Monthly Notices of the Royal Astronomical Society, 503, 4838, "10.1093/mnras/stab633"

Kilpatrick, C. D., Burchett, J. N., Jones, D. O., et al. 2021, The Astrophysical Journal Letters, 907, L3, "10.3847/2041-8213/abd560"

Kiman, R., Schmidt, S. J., Angus, R., et al. 2019, The Astronomical Journal, 157, 231, "10.3847/1538-3881/ab1753"

Kingma, D. P., & Ba, J. 2014, arXiv e-prints, arXiv:1412.6980. https://arxiv.org/abs/1412.6980

Kirsten, F., Marcote, B., Nimmo, K., et al. 2022, Nature, 602, 585, "10.1038/s41586-021-04354-w"

Koposov, S., & Bartunov, O. 2006, in Astronomical Society of the Pacific Conference Series, Vol. 351, Astronomical Data Analysis Software and Systems XV, ed. C. Gabriel, C. Arviset, D. Ponz, & S. Enrique, 735

Koposov, S., & Bartunov, O. 2019, Q3C: A PostgreSQL package for spatial queries and cross-matches of large astronomical catalogs. http://ascl.net/1905.008

Kosiarek, M. R., Crossfield, I. J. M., Hardegree-Ullman, K. K., et al. 2019, The Astronomical Journal, 157, 97, "10.3847/1538-3881/aaf79c"

Kowalski, A. F., Hawley, S. L., Holtzman, J. A., Wisniewski, J. P., & Hilton, E. J. 2010, The Astrophysical Journal Letters, 714, L98, "10.1088/2041-8205/714/1/L98"

Kowalski, A. F., Hawley, S. L., Wisniewski, J. P., et al. 2013, Astrophysical Journal Supplement Series, 207, 15, "10.1088/0067-0049/207/1/15"

Kreps, J., Narkhede, N., & Rao, J. 2011, in Proceedings of the NetDB, 1–7

Kulkarni, S. R., & Rau, A. 2006, Astrophysical Journal Letters, 644, L63, "10.1086/505423"

Kumar, M. 1988, Marine Geodesy, 12, 117

Kumar, S., Gezari, S., Heinis, S., et al. 2015, Astrophysical Journal, 802, 27, "10.1088/0004-637X/802/1/27"

Lacy, C. H., Moffett, T. J., & Evans, D. S. 1976, The Astrophysical Journal Supplement Series, 30, 85, "10.1086/190358"

Lang, D., Hogg, D. W., Mierle, K., Blanton, M., & Roweis, S. 2010, The Astronomical Journal, 139, 1782, "10.1088/0004-6256/139/5/1782"

Larson, S., Beshore, E., Hill, R., et al. 2003, in AAS/Division for Planetary Sciences Meeting Abstracts #35, AAS/Division for Planetary Sciences Meeting Abstracts, 36.04

Law, N., Vasquez Soto, A., Corbett, H., et al. 2022a, in Society of Photo-Optical Instrumentation Engineers (SPIE) Conference Series, Vol. 12182, Ground-based and Airborne Telescopes IX

Law, N., Vasquez Soto, A., Corbett, H., et al. 2022b, in Society of Photo-Optical Instrumentation Engineers (SPIE) Conference Series, Vol. 12182, Ground-based and Airborne Telescopes IX, ed. H. K. Marshall, J. Spyromilio, & T. Usuda, 121824H, "10.1117/12.2630037"

Law, N. M., Kulkarni, S. R., Dekany, R. G., et al. 2009, Publications of the Astronomical Society of the Pacific, 121, 1395, "10.1086/648598"

Law, N. M., Fors, O., Ratzloff, J., et al. 2015, Publications of the Astronomical Society of the Pacific, 127, 234, "10.1086/680521"

Law, N. M., Corbett, H., Galliher, N. W., et al. 2022c, Publications of the Astronomical Society of the Pacific, 134, 035003, "10.1088/1538-3873/ac4811"

Le Folgoc, L., Baltatzis, V., Desai, S., et al. 2021, arXiv e-prints, arXiv:2110.04286. https://arxiv.org/abs/2110.04286

LeCun, Y., & Bengio, Y. 1995, in The Handbook of Brain Theory and Neural Networks, ed. M. A. Arbib (MIT Press)

LeCun, Y., Boser, B., Denker, J. S., et al. 1989, Neural Computation, 1, 541

Li, L., Jamieson, K., DeSalvo, G., Rostamizadeh, A., & Talwalkar, A. 2018, Journal of Machine Learning Research, 18, 1. http://jmlr.org/papers/v18/16-558.html

Li, L., Li, Q.-C., Zhong, S.-Q., et al. 2022, The Astrophysical Journal, 929, 139, "10.3847/1538-4357/ac5d5a"

Lipunov, V. M., Krylov, A. V., Kornilov, V. G., et al. 2004, Astronomische Nachrichten, 325, 580, "10.1002/asna.200410284"

Loyd, R. O. P., Shkolnik, E. L., Schneider, A. C., et al. 2018, The Astrophysical Journal, 867, 70, "10.3847/1538-4357/aae2ae"

Loyd, R. O. P., France, K., Youngblood, A., et al. 2018, ApJ, 867, 71, "10.3847/1538-4357/aae2bd"

LSST Science Collaboration, Abell, P. A., Allison, J., et al. 2009, arXiv e-prints, arXiv:0912.0201. https://arxiv.org/abs/0912.0201

Lyutikov, M. 2021, The Astrophysical Journal, 922, 166, "10.3847/1538-4357/ac1b32"

Lyutikov, M., & Lorimer, D. R. 2016, The Astrophysical Journal Letters, 824, L18, "10.3847/2041-8205/824/2/l18"

Machia, L., Law, N., Corbett, H., et al. 2022, in Society of Photo-Optical Instrumentation Engineers (SPIE) Conference Series, Vol. 12182, Ground-based and Airborne Telescopes IX

MAGIC Collaboration, Acciari, V. A., Ansoldi, S., et al. 2018, Monthly Notices of the Royal Astronomical Society, 481, 2479, "10.1093/mnras/sty2422"

Mahabal, A., Rebbapragada, U., Walters, R., et al. 2019, Publications of the Astronomical Society of the Pacific, 131, 038002, "10.1088/1538-3873/aaf3fa"

Makhlouf, K., Turpin, D., Corre, D., et al. 2021, arXiv

Maley, P. 1991, Advances in Space Research, 11, 33–36, "10.1016/0273-1177(91)90539-v"

Maley, P. D. 1987, The Astrophysical Journal, 317, L39, "10.1086/184909"

Mannings, A. G., Fong, W.-f., Simha, S., et al. 2021, The Astrophysical Journal, 917, 75, "10.3847/1538-4357/abff56"

Marcote, B., Nimmo, K., Hessels, J. W. T., et al. 2020, Nature, 577, 190, "10.1038/s41586-019-1866-z"

Martin-Carrillo, A., Hanlon, L., Topinka, M., et al. 2014, Astronomy & Astrophysics, 567, A84, "10.1051/0004-6361/201220872"

Matheson, T., Stubens, C., Wolf, N., et al. 2021, The Astronomical Journal, 161, 107, "10.3847/1538-3881/abd703"

Mcculloch, W., & Pitts, W. 1943, Bulletin of Mathematical Biophysics, 5, 127

McCully, C., Crawford, S., Kovacs, G., et al. 2018, astropy/astroscrappy: v1.0.5 Zenodo Release, v1.0.5, Zenodo, "10.5281/zenodo.1482019"

McDowell, J. C. 2020, Astrophysical Journal Letters, 892, L36, "10.3847/2041-8213/ab8016"

Mereghetti, S., Savchenko, V., Ferrigno, C., et al. 2020, The Astrophysical Journal, 898, L29, "10.3847/2041-8213/aba2cf"

Metzger, B. D., Margalit, B., & Sironi, L. 2019, Monthly Notices of the Royal Astronomical Society, 485, 4091, "10.1093/mnras/stz700"

Nelder, J. A., & Mead, R. 1965, Computer Journal, 7, 308

Niino, Y., Tominaga, N., Totani, T., et al. 2018, Publications of the Astronomical Society of Japan, 70, L7, “10.1093/pasj/psy102”

Niino, Y., Doi, M., Sako, S., et al. 2022, The Astrophysical Journal, 931, 109, “10.3847/1538-4357/ac6be8”

Nimmo, K., Hewitt, D. M., Hessels, J. W. T., et al. 2022, The Astrophysical Journal Letters, 927, L3, “10.3847/2041-8213/ac540f”

Nir, G., Ofek, E. O., Ben-Ami, S., et al. 2021, Monthly Notices of the Royal Astronomical Society, 505, 2477, “10.1093/mnras/stab1437”

Núñez, C., Tejos, N., Pignata, G., et al. 2021, Astronomy & Astrophysics, 653, A119, “10.1051/0004-6361/202141110”

Ofek, E. O. 2019, Publications of the Astronomical Society of the Pacific, 131, 054504, “10.1088/1538-3873/ab04df”

Ofek, E. O., & Ben-Ami, S. 2020, Publications of the Astronomical Society of the Pacific, 132, 125004, “10.1088/1538-3873/abc14c”

Osten, R. A., & Wolk, S. J. 2015, The Astrophysical Journal, 809, 79, “10.1088/0004-637X/809/1/79”

Osten, R. A., Godet, O., Drake, S., et al. 2010, Astrophysical Journal, 721, 785, “10.1088/0004-637X/721/1/785”

Osten, R. A., Kowalski, A., Drake, S. A., et al. 2016, The Astrophysical Journal, 832, 174, “10.3847/0004-637X/832/2/174”

Parsons, S. G., Gänsicke, B. T., Marsh, T. R., et al. 2018, Monthly Notices of the Royal Astronomical Society, 481, 1083, “10.1093/mnras/sty2345”

Patterson, M. T., Bellm, E. C., Rusholme, B., et al. 2019, Publications of the Astronomical Society of the Pacific, 131, 018001, “10.1088/1538-3873/aae904”

Pedregosa, F., Varoquaux, G., Gramfort, A., et al. 2012, arXiv e-prints, arXiv:1201.0490. https://arxiv.org/abs/1201.0490

Perrett, K., Balam, D., Sullivan, M., et al. 2010, The Astronomical Journal, 140, 518, “10.1088/0004-6256/140/2/518”

Petroff, E., Bailes, M., Barr, E. D., et al. 2015, Monthly Notices of the Royal Astronomical Society, 447, 246, “10.1093/mnras/stu2419”

Pickles, A., & Depagne, É. 2010, Publications of the Astronomical Society of the Pacific, 122, 1437, “10.1086/657947”

Pietras, M., Falewicz, R., Siarkowski, M., Bicz, K., & Preś, P. 2022, Astrophysical Journal, 935, 143, “10.3847/1538-4357/ac8352”

Piro, L., Bruni, G., Troja, E., et al. 2021, Astronomy & Astrophysics, 656, L15, “10.1051/0004-6361/202141903”

Platts, E., Weltman, A., Walters, A., et al. 2019, Physics Reports, 821, 1, “10.1016/j.physrep.2019.06.003”

Pollacco, D. L., Skillen, I., Collier Cameron, A., et al. 2006, PASP, 118, 1407, “10.1086/508556”

Powell, B. P., Kostov, V. B., Rappaport, S. A., et al. 2021, The Astronomical Journal, 162, 299, “10.3847/1538-3881/ac2c81”

Puetter, R. C., Smith, H. E., Willner, S. P., & Pipher, J. L. 1981, The Astrophysical Journal, 243, 345, “10.1086/158603”

Quimby, R. M., Shafter, A. W., & Corbett, H. 2021, Research Notes of the American Astronomical Society, 5, 160, “10.3847/2515-5172/ac14c0”

Ranjan, S., Wordsworth, R., & Sasselov, D. D. 2017, Astrophysical Journal, 843, 110, “10.3847/1538-4357/aa773e”

Rast, R. H. 1991, Icarus, 90, 328–329, “10.1016/0019-1035(91)90112-7”

Ratzloff, J. K., Law, N. M., Corbett, H. T., Fors, O., & del Ser, D. 2020a, Journal of Astronomical Telescopes, Instruments, and Systems, 6, 018002, “10.1117/1.JATIS.6.1.018002”

Ratzloff, J. K., Law, N. M., Fors, O., et al. 2019a, Publications of the Astronomical Society of the Pacific, 131, 075001, “10.1088/1538-3873/ab19d0”

Ratzloff, J. K., Corbett, H., Law, N. M., et al. 2019b, Publications of the Astronomical Society of the Pacific, 131, 084201, “10.1088/1538-3873/ab1d77”

Ratzloff, J. K., Barlow, B. N., Kupfer, T., et al. 2019c, The Astrophysical Journal, 883, 51, “10.3847/1538-4357/ab3727”

Ratzloff, J. K., Barlow, B. N., Németh, P., et al. 2020b, The Astrophysical Journal, 890, 126, “10.3847/1538-4357/ab64f3”

Ravi, V., Law, C. J., Li, D., et al. 2022, Monthly Notices of the Royal Astronomical Society, 513, 982, “10.1093/mnras/stac465”

Richmond, M. W., Tanaka, M., Morokuma, T., et al. 2020, Publications of the Astronomical Society of Japan, 72, 3, “10.1093/pasj/psz120”

Ricker, G. R., Winn, J. N., Vanderspek, R., et al. 2014, in Society of Photo-Optical Instrumentation Engineers (SPIE) Conference Series, Vol. 9143, Space Telescopes and Instrumentation 2014: Optical, Infrared, and Millimeter Wave, ed. J. Oschmann, Jacobus M., M. Clampin, G. G. Fazio, & H. A. MacEwen, 914320, “10.1117/12.2063489”

Rimmer, P. B., Xu, J., Thompson, S. J., et al. 2018, Science Advances, 4, eaar3302, “10.1126/sciadv.aar3302”

Robinson, R. D., Wheatley, J. M., Welsh, B. Y., et al. 2005, The Astrophysical Journal, 633, 447, “10.1086/444608”

Rolnick, D., Veit, A., Belongie, S., & Shavit, N. 2017, arXiv e-prints, arXiv:1705.10694. https://arxiv.org/abs/1705.10694

Saha, A., Matheson, T., Snodgrass, R., et al. 2014, in Society of Photo-Optical Instrumentation Engineers (SPIE) Conference Series, Vol. 9149, Observatory Operations: Strategies, Processes, and Systems V, ed. A. B. Peck, C. R. Benn, & R. L. Seaman, 914908, “10.1117/12.2056988”

Sako, S., Ohsawa, R., Takahashi, H., et al. 2018, in Society of Photo-Optical Instrumentation Engineers (SPIE) Conference Series, Vol. 10702, Ground-based and Airborne Instrumentation for Astronomy VII, 107020J, “10.1117/12.2310049”

Schaefer, B. E., King, J. R., & Deliyannis, C. P. 2000, Astrophysical Journal, 529, 1026, “10.1086/308325”

Schaefer, B. E., Barber, M., Brooks, J. J., et al. 1987, Astrophysical Journal, 320, 398, “10.1086/165552”

Segura, A., Walkowicz, L. M., Meadows, V., Kasting, J., & Hawley, S. 2010, Astrobiology, 10, 751, “10.1089/ast.2009.0376”

Shamir, L., & Nemiroff, R. J. 2006, Publications of the Astronomical Society of the Pacific, 118, 1180, “10.1086/506989”

Shappee, B. J., Prieto, J. L., Grupe, D., et al. 2014, Astrophysical Journal, 788, 48, “10.1088/0004-637X/788/1/48”

Simonyan, K., & Zisserman, A. 2014, arXiv e-prints, arXiv:1409.1556. https://arxiv.org/abs/1409.1556

Sokolovsky, K. V., Johnson, T. J., Buson, S., et al. 2023, arXiv e-prints, arXiv:2302.03043, “10.48550/arXiv.2302.03043”

Sokołowski, M., Małek, K., Piotrowski, L. W., & Wrochna, G. 2010, Advances in Astronomy, 2010, 463496, “10.1155/2010/463496”

Srivastava, N., Hinton, G., Krizhevsky, A., Sutskever, I., & Salakhutdinov, R. 2014, Journal of Machine Learning Research, 15, 1929. http://jmlr.org/papers/v15/srivastava14a.html

Stelzer, B., Caramazza, M., Raetz, S., Argiroffi, C., & Coffaro, M. 2022, Astronomy & Astrophysics, 667, L9, “10.1051/0004-6361/202244642”

Stoppa, F., Vreeswijk, P., Bloemen, S., et al. 2022, arXiv e-prints, arXiv:2202.00489. https://arxiv.org/abs/2202.00489

Talens, G. J. J., Spronck, J. F. P., Lesage, A. L., et al. 2017, Astronomy & Astrophysics, 601, A11, "10.1051/0004-6361/201630319"

Tamuz, O., Mazeh, T., & Zucker, S. 2005, Monthly Notices of the Royal Astronomical Society, 356, 1466, "10.1111/j.1365-2966.2004.08585.x"

Tendulkar, S. P., Gil de Paz, A., Kirichenko, A. Y., et al. 2021, The Astrophysical Journal Letters, 908, L12, "10.3847/2041-8213/abdb38"

The CHIME/FRB Collaboration, :, Amiri, M., et al. 2018, The Astrophysical Journal, 863, 48, "10.3847/1538-4357/aad188"

Tilley, M. A., Segura, A., Meadows, V., Hawley, S., & Davenport, J. 2019, Astrobiology, 19, 64, "10.1089/ast.2017.1794"

Tingay, S. 2020, Publications of the Astronomical Society of Australia, 37, e015, "10.1017/pasa.2020.7"

Tingay, S., & Joubert, W. 2021, Publications of the Astronomical Society of Australia, 38, e001, "10.1017/pasa.2020.53"

Tingay, S. J. 2022, The Astrophysical Journal Letters, 934, L29, "10.3847/2041-8213/ac82e6"

Tokovinin, A., Corbett, H., Fors, O., et al. 2018, The Astronomical Journal, 156, 120, "10.3847/1538-3881/aad694"

Tominaga, N., Niino, Y., Totani, T., et al. 2018, Publications of the Astronomical Society of Japan, 70, 103, "10.1093/pasj/psy101"

Tonry, J. L., Denneau, L., Heinze, A. N., et al. 2018, Publications of the Astronomical Society of the Pacific, 130, 064505, "10.1088/1538-3873/aabadf"

Tonry, J. L., Denneau, L., Flewelling, H., et al. 2018, Astrophysical Journal, 867, 105, "10.3847/1538-4357/aae386"

Troja, E., Lipunov, V. M., Mundell, C. G., et al. 2017, Nature, 547, 425, "10.1038/nature23289"

Tyson, J. A., Ivezić, Ž., Bradshaw, A., et al. 2020, The Astronomical Journal, 160, 226, "10.3847/1538-3881/abba3e"

Vallely, P. J., Kochanek, C. S., Stanek, K. Z., Fausnaugh, M., & Shappee, B. J. 2021, Monthly Notices of the Royal Astronomical Society, 500, 5639, "10.1093/mnras/staa3675"

van Dokkum, P. G. 2001, Publications of the Astronomical Society of the Pacific, 113, 1420, "10.1086/323894"

van Roestel, J., Groot, P. J., Kupfer, T., et al. 2019, Monthly Notices of the Royal Astronomical Society, 484, 4507, "10.1093/mnras/stz241"

Vanderlinde, K., Liu, A., Gaensler, B., et al. 2019, in Canadian Long Range Plan for Astronomy and Astrophysics White Papers, Vol. 2020, 28, "10.5281/zenodo.3765414"

Vasquez Soto, A., Law, N., Corbett, H., et al. 2022, in Society of Photo-Optical Instrumentation Engineers (SPIE) Conference Series, Vol. 12182, Ground-based and Airborne Telescopes IX

Vestrand, W. T., Wren, J. A., Panaitescu, A., et al. 2014, Science, 343, 38, "10.1126/science.1242316"

Voges, W., Aschenbach, B., Boller, T., et al. 1999, Astronomy & Astrophysics, 349, 389. https://arxiv.org/abs/astro-ph/9909315

Walkowicz, L. M., Johns-Krull, C. M., & Hawley, S. L. 2008, The Astrophysical Journal, 677, 593, "10.1086/526421"

Wang, W., Luo, R., Yue, H., et al. 2018, The Astrophysical Journal, 852, 140, "10.3847/1538-4357/aaa025"

Watson, C., Henden, A. A., & Price, A. 2020, VizieR Online Data Catalog, B/vsx

Wee, J., Blagorodnova, N., Penprase, B. E., et al. 2020, The Astrophysical Journal, 899, 162, "10.3847/1538-4357/aba3cc"

Wolf, C., Onken, C. A., Luvaul, L. C., et al. 2018, Publications of the Astronomical Society of Australia, 35, e010, "10.1017/pasa.2018.5"

Xin, L. P., Li, H. L., Wang, J., et al. 2021, Astrophysical Journal, 909, 106, "10.3847/1538-4357/abdd1b"

Xu, H., Niu, J. R., Chen, P., et al. 2022, Nature, 609, 685, "10.1038/s41586-022-05071-8"

Yang, Y.-P., Zhang, B., & Wei, J.-Y. 2019, The Astrophysical Journal, 878, 89, "10.3847/1538-4357/ab1fe2"

Yeh, T., Lee, B. B., & Kremers, J. 1996, Vision Research, 36, 913, "10.1016/0042-6989(95)00332-0"

Yi, S.-X., Gao, H., & Zhang, B. 2014, The Astrophysical Journal Letters, 792, L21, "10.1088/2041-8205/792/1/L21"

Zackay, B., & Ofek, E. O. 2017, The Astrophysical Journal, 836, 188, "10.3847/1538-4357/836/2/188"

Zackay, B., Ofek, E. O., & Gal-Yam, A. 2016, Astrophysical Journal, 830, 27, "10.3847/0004-637X/830/1/27"

Zhang, K., Li, L., Zhang, Z., et al. 2022, Universe, 8, 355, "10.3390/universe8070355"

Zwicky, F. 1938, The Astrophysical Journal, 88, 529, "10.1086/144007"